THE EFFECT OF A HIGH-TEMPERATURE HIGH-PRESSURE NITROGEN ENVIRONMENT WITH CARBONACEOUS IMPURITIES ON THE PERFORMANCE OF THREE AUSTENITIC ALLOYS

A thesis

submitted in partial fulfillment

of the requirements for the Degree

of

Master of Engineering (Mechanical)

in the

University of Canterbury

by

Franziska Anna Jones

University of Canterbury
2007

Abstract

WhisperGen™ heater head components are currently machined from the austenitic stainless steel Sandvik 253MA. The inner surface of the heater heads is subjected to the working gas of the engine, which is a high-pressure, high-temperature nitrogen-based environment with carbonaceous impurities. As a result of this exposure, a scale forms during operation and eventually spalls. This spalled scale causes abrasive damage to piston seals and guides, which leads to pressure loss and eventual failure of the engine. The aim of the present work was to compare the performance of the austenitic alloy 253MA with two alternative alloys, Incoloy 800H and AISI 310, thereby enabling a material recommendation.

A literature review provided information about many general aspects of high temperature corrosion in similar alloys. However, little was found about the application of these alloys in environments similar to those experienced by a WhisperGen™ heater head. Therefore, laboratory experiments were conducted to indicate the relative performance characteristics of the three potential alloys (253MA, Incoloy 800H and AISI 310). To overcome the difficulties with testing at high temperatures and pressures, Thermo-Calc™ was used to calculate gas mixtures at 1 bar that approximated the chemical potentials of carbon and nitrogen in the working gas at 24 bar. Comparisons of the different materials were made via weight loss/gain measurements and metallographic analysis, which included optical microscopy, scanning electron microscopy, X-ray mapping and electron back scatter diffraction (EBSD). The laboratory test sample results were also compared with results from heater heads of the same materials that were run in an actual WhisperGen™ engine.

The experimental results taken in total indicate that 253MA is the least suitable alloy for the heater head application because it exhibited poor spalling performance, internal oxidation and formation of a large amount of $Cr_{23}C_6$. AISI 310 was shown in all cases to develop the detrimental sigma phase, although this alloy was the least susceptible to internal oxidation. Incoloy 800H was the most resistant alloy to all forms of degradation and is thus recommended for the heater head application.

Acknowledgements

Firstly, I would like to acknowledge Dr Milo Kral for offering me this opportunity. His advice and knowledge have been invaluable in allowing me to complete the project. The conference in the states was a valuable experience which would not have been possible otherwise. I have learned a great deal from this experience and will forever be grateful for the opportunity to work in a field I enjoy.

I strongly acknowledge Dr Chris Hutchinson, who generously performed the Thermo-Calc™ calculations that made this thesis possible. Discussions with Dr Hutchinson were critical to decisions regarding experimental design.

I also wish to thank WhisperGen Limited for the opportunity and financial support to complete this thesis. Thank you to Dr Don Clucas and the staff at WhisperGen Limited for their interest in the project and willingness to help me. In particular, I would like to thank Dr Lee Cameron for the guidance he generously provided throughout the course of the project.

Thank you to Technology New Zealand for providing funding for the project.

Finally, I would like to thank my family and friends for their support, in particular my Mum and Mark.

Nanny, I will always remember your kindness and the good times we had together.

Table of Contents

1 Introduction

1.1 Project Aims

WhisperGen™ heater head components are subjected to a high-temperature, high-pressure nitrogen environment with carbonaceous impurities, and are currently made of the austenitic stainless steel Sandvik 253MA. The heater head components develop a scale which spalls as a result of thermal cycling. The abrasive nature of the spalled material causes damage to piston guides and seals, eventually leading to pressure loss and a severe degradation of engine performance.

In general, high-temperature alloys rely on the development of a protective oxide layer in order to resist excessive high-temperature corrosion modes such as oxidation, nitridation and carburisation. Sandvik 253MA relies on the formation of a slow-growing, continuous, stable and adherent chromia (Cr_2O_3) layer for protection against high-temperature corrosion. However, chromia layers are susceptible to spalling in thermal cycling conditions *[1]*.

The spalling characteristics of an alloy under thermal cycling conditions are dictated mainly by scale adherence, which is in turn dictated by both scale morphology and alloy and scale compositions *[2]*. The interdependent effect of alloy additions on oxide-layer adherence makes it difficult to predict the performance of alloys in specific conditions without the use of experimentation.

The objective of this thesis was to evaluate the spalling, and general performance, of several different alloys in the heater head environment, including Sandvik 253MA, with the aim of

recommending the most suitable alloy. The two alloys chosen for the comparison with 253MA were the austenitic stainless steel AISI 310, and the iron-nickel based austenitic superalloy, Incoloy 800H. It is important to note the effect of nickel content on the performance of high-temperature alloys, as 253MA has particularly low nickel content (10%), while 310 and 800H have far greater nickel content (20 and 31%, respectively). An increase in nickel content improves the resistance of alloys to cyclic oxidation, promotes a more adherent oxide layer, and increases metallurgical stability and creep strength *[3]*.

In order to compare the performance of the three alloys under different conditions, a laboratory setup was designed to simulate the heater head environment. In addition, heater heads were machined from each of the three alloys and run in an actual WhisperGen™ for comparison to the laboratory results.

1.2 Background

This thesis was sponsored by WhisperGen Limited and Technology New Zealand. The company WhisperGen Limited designs, develops and implements WhisperGen™ microCHP systems. The WhisperGen™ system is a quiet, clean burning and efficient system that generates both heat and power in either AC or DC form. The AC unit is referred to as the WhisperGen™ micro combined heat and power (microCHP) system, and is aimed at the residential market. The microCHP units are central heating boilers which generate electricity that can be either used in-house or sold back to the electricity grid. The DC unit is referred to as the WhisperGen™ heat and power system and is used in remote or marine applications to provide heating/hot water, in addition to battery charging. A fully assembled AC WhisperGen™ microCHP system is shown in Figure 1.1.

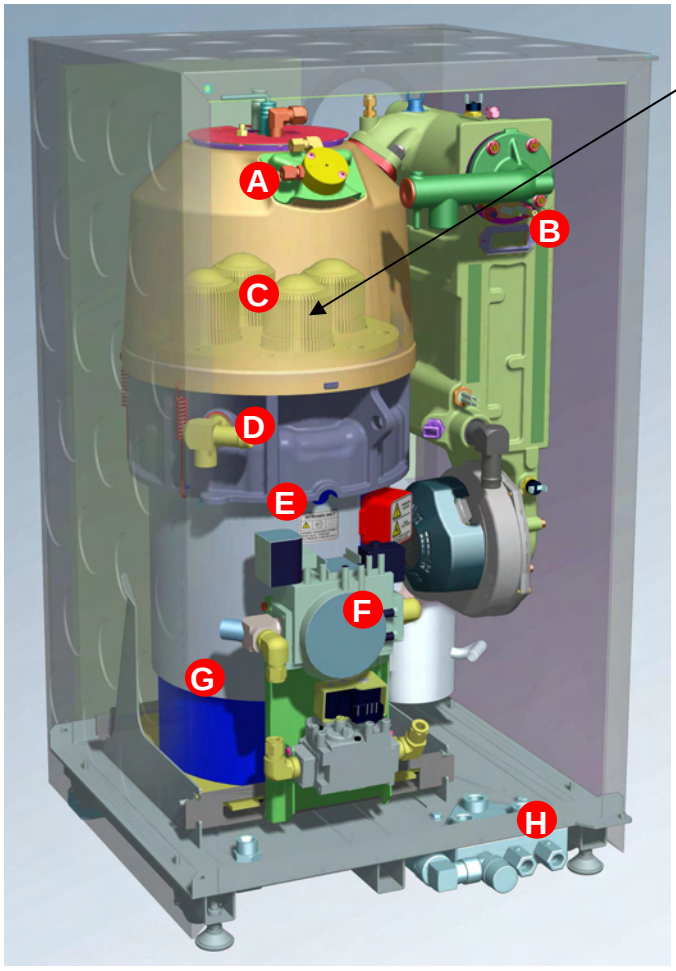

Heater Heads

A) Gas burner: flame heats the four cylinder heads of the engine

B) Exhaust heat recovery unit: uses the exhaust heat to heat the water

C) Stirling engine: uses the heat from the burner to push pistons back and forth

D) Water heating: water is further heated as it passes through the engine

E) Wobble Yoke (inside): converts the linear motion of the pistons into rotating motion for the alternator

F) Gas valve: supplies and regulates the gas to the burner

G) Rotary alternator (inside): generates electricity

H) Water pipe connections: delivers the hot water to the home's hot water cylinder and heating system

Figure 1.1: AC Mark 5 WhisperGen™ microCHP system (AC Product Brochure), showing the placement of heater heads with respect to the unit.

The component studied in the present work is referred to as a heater head, and acts as a hot end heat exchanger. The placement of heater heads with respect to the rest of an engine is also shown in Figure 1.1. During operation, flame in the external combustion chamber directly impinges onto the top of four heater heads, which conduct heat into the working gas of the engine. Each of the four heater heads is part of a piston-cylinder arrangement as illustrated in Figure 1.2.

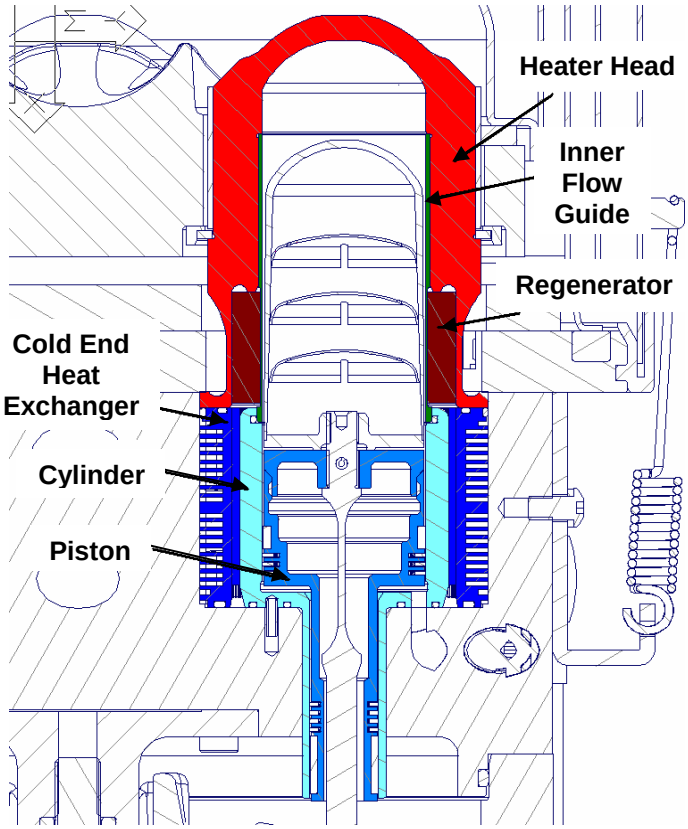

Figure 1.2: Cross section of a heater head, regenerator and inner flow guide with respect to other engine parts (right).

Scale has been observed to form on the inside of heater heads that have been exposed to extreme temperatures. When this scale subsequently spalls, it may damage other components such as the piston guides and seals, leading to pressure loss and a severe degradation in engine performance. Figure 1.3 shows the inner area of a heater head on which scale has developed after exposure to the engine environment. The onset of scaling is reported to coincide with the 'boost mode' of operation where hotter than usual heater head temperatures are encountered (up to 930°C as opposed to 850°C in normal operation).

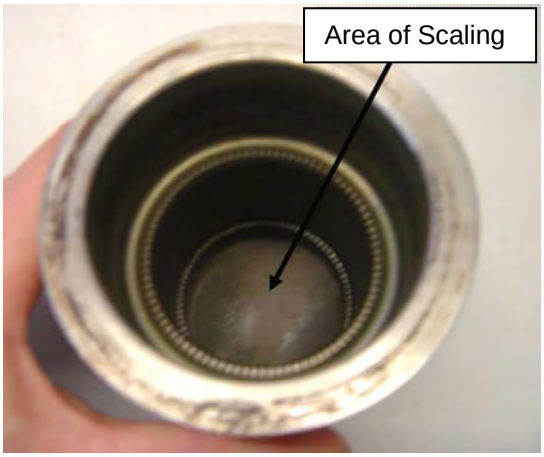

Figure 1.3: Internal scale present on the inside of a heater head that was in service.

The outer surface of the heater head is exposed to combustion gases from the external combustion chamber, whereas its inner surface is exposed to the working gas of the engine. Only the effect of the working gas environment on the inner surface was investigated in this research. BOC industrial grade oxygen-free nitrogen 152 ($\leq$ 10 ppm O_2) is employed as the working fluid of a WhisperGen^{TM} because of its availability and inert properties. The working gas is charged to 24 bar pressure (in the AC machine) and 28 bar (in the DC machine).

Since the engine is charged with nitrogen as a working gas at the beginning of its life, it was originally thought that the engine retained this pure working gas during operation. However, gas composition tests conducted after a number of hours of operation showed that the working gas contains significant levels of carbon monoxide, carbon dioxide, hydrogen and oxygen. The origin of these gases is the subject of some speculation at present, but it suffices to say that to some extent the gases are unavoidable.

1.3 Outline of Thesis

Chapter 2 provides an overview of literature relevant to the project. The chapter emphasises the importance of the formation of a protective oxide layer on high-temperature alloys. It provides information about the rate of oxidation, the structure and texture of oxide layers, chromia layers and stress relief in oxide layers, and gives the requirements for a protective oxide layer. A general overview of high-temperature corrosion is included, which describes some aspects of oxidation, nitridation and carburisation. Precipitate phases formed during high-temperature aging of austenitic alloys are described, and a ternary equilibrium phase diagram for Fe-Cr-Ni alloys is provided. Brief descriptions of austenitic stainless steels and superalloys are provided, and the sensitisation of austenitic stainless steel is presented in some detail. Literature about the three alloys 253MA, 310 and 800H is provided and compared. The effect of alloying additions on spalling behaviour and the effect of non-metallic inclusions on alloy properties are also discussed.

The lack of literature about the application of austenitic alloys in high-pressure, high-temperature, nitrogen-rich environments led to the decision to carry out the present laboratory experiments. The design and set-up of the experiments is described in Chapter 3 of this thesis. The main complicating factor with the laboratory simulation of the heater head environment was the impracticality of testing at the intended service pressure. Hence an alternative to testing at pressure was adopted, in which the chemical potentials of the gas mixture at 24 bar and various temperatures were simulated at 1 bar. The details of this simulation are included, along with the limitations of the design and equipment.

The alloy samples from the tests described in Chapter 3 were analysed using several advanced metallurgical techniques, the details of which are provided in Chapter 4. An example of each

technique is provided along with an explanation. The use of energy dispersive X-ray spectroscopy (EDS) to generate X-ray maps is described, as well as the use of electron back scatter diffraction (EBSD) for phase identification. Finally, the etching process and subsequent optical microscopy undertaken are described.

Chapter 5 provides a summary of the results of the analysis described in Chapter 4, and discusses these results. A summary of weight-change results is provided for the laboratory testing, and a table containing information about the thickness of the oxide layers and amount of spalling observed for all tests is given. A selection of microstructures for both the heater head and laboratory tests at 900°C is provided, and allows direct comparison between the three alloys. The first section discusses the comparative spalling performance of the three alloys with respect to experimental findings. The laboratory results showed that 253MA spalled the most, while 800H spalled the least. The second section discusses the microstructures observed and the implications on alloy performance. The heater head and laboratory test results are discussed separately, and are later compared with each other. The comparison showed some similarities and some discrepancies, suggesting that the simulation was somewhat successful for 310 and 800H, but not for 253MA. Reasons for the discrepancies are provided where possible. The final section of Chapter 5 summarises the findings from the first two sections, and provides a summary of the factors which should be taken into account when selecting an alloy for the heater head application.

Chapter 6 draws conclusions from the discussion and results found during the research, and suggests the most suitable alloy for the application. Recommendations for further work are provided in Chapter 7.

References

[1] A. Rahmel, H. J. Grabke, W. Steinkusch, *Materials and Corrosion* 1998, *49*, 221.
[2] B. Gleeson, B. Li, "Cyclic oxidation of chromia-scale forming alloys: Lifetime prediction and accounting for the effects of major and minor alloying additions", Les Embiez, France, 2004.
[3] G. Y. Lai, *High-Temperature Corrosion of Engineering Alloys*, ASM International, 1990.

2 Literature Review

2.1 Introduction

Currently WhisperGen™ heater heads are made out of the austenitic stainless steel Sandvik 253MA. The heater heads are exposed to a high-temperature, high-pressure, nitrogen-based environment with carbonaceous impurities, and thermal cycling occurs during engine start-up and shut-down. The service conditions result in formation of scale, and thermal cycling leads to spalling of the scale. Spallation of the scale formed on heater heads during operation leads to a detrimental effect on engine performance. A material selection process was therefore undertaken in this thesis to assess whether alloy AISI 310 or Incoloy 800H would be a better choice for this application.

This chapter provides a review of the current relevant literature concerning the behaviour of the three aforementioned alloys in high-temperature corrosion environments, and compares their performance where possible. A gap was found in the literature, in that there have not been any studies conducted at high pressure for the alloys mentioned, or for similar alloys. Very few studies have been conducted for the three alloys in nitrogen-based environments, and no publications were found involving nitrogen-based environments with carbonaceous impurities. Therefore it was decided that a study should be conducted in the unique conditions of a WhisperGen™ heater head. In addition, this chapter describes the development of, and properties required for, a protective oxide layer to develop, and then describes the conditions required to cause spallation of an oxide layer. The different forms of high-temperature corrosion relevant to this thesis will be discussed,

along with the properties of the three alloys previously mentioned, and the effect of alloying additions on the spallation behaviour of chromia-forming alloys.

2.2 Oxide Layers

Many high temperature alloys derive their resistance to high-temperature corrosion by producing and maintaining a protective solid oxide scale layer consisting of chromia (Cr_2O_3), silica (SiO_2) and alumina (Al_2O_3) or various spinels *[1, 2]*. The spinel structure has the general composition $(A)(B)_2O_4$, with A and B representing cations. The structure has a cubic unit cell consisting of eight smaller cubes. The smaller cubes have oxygen ions located in face-centered cubic positions, so there are a total of 32 oxygen ions in the unit cell. There are four octahedral sites and eight tetrahedral sites in each smaller cube, and 3 out of the 12 available sites are filled by cations.

The alloys Sandvik 253MA, AISI 310 and Incoloy 800H, studied for this thesis, are chromia-forming alloys, and therefore rely on the development and continuing integrity of a chromia layer. Unfortunately, chromia layers are susceptible to cracking and spalling during creep, growth or thermal cycling *[3]*. Methods exist that can be used to predict the useful service life of chromia-forming alloys exposed to thermal cycling conditions, and a detailed summary of these methods is given in Gleeson and Li *[2]*. However, it was not possible to apply these methods to this thesis, because the experiments that were carried out were not designed to provide the complex variables required for these analyses.

2.2.1 Oxidation Reactions

The reaction of a metal, M, with oxygen or other gases at high temperature, occurs over a series of steps shown in Figure 2.1. The initial step is the adsorption of oxygen on the surface of the metal, followed by a chemical reaction to form the surface oxide, which may be accompanied by the dissolution of oxygen in the metal. The oxide then grows laterally into a continuous film, which may protect the metal, or the film may contain defects such as cavities, microcracks, and porosity, and will therefore not be protective *[1, 4]*. The chemical reactions of metal with oxygen, water vapour and carbon dioxide, are shown in Equations 2.1, 2.2 and 2.3, respectively.

$$M + O_2 \rightarrow MO_2 \qquad \textbf{Equation 2.1}$$

$$M + H_2O \rightarrow MO + H_2 \qquad \textbf{Equation 2.2}$$

$$M + CO_2 \rightarrow MO + CO \qquad \textbf{Equation 2.3}$$

For example, the oxidation of chromium in oxygen to form Cr_2O_3 (chromia), would take place with the reaction shown in Equation 2.4.

$$2Cr + \tfrac{3}{2}O_2 \rightarrow Cr_2O_3 \qquad \textbf{Equation 2.4}$$

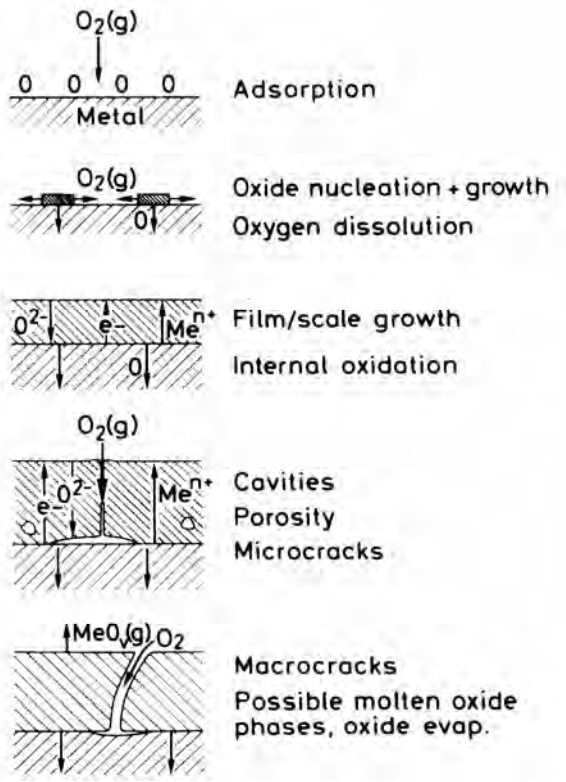

Figure 2.1: Oxide layer growth during high-temperature oxidation ***[1]***

2.2.2 Requirements for a Protective Oxide Layer

High-temperature alloys rely on the formation of a protective oxide layer in order to resist high-temperature attack. In order for an oxide layer to exhibit good protective properties, the scale should be slow growing, very stable, adherent, and continuous *[2]*. A more detailed source *[5]* describing the required properties for an oxide layer states the following requirements:

- The Pilling-Bedworth ratio must be greater than 1 so the oxide completely covers the surface
- A low vapour pressure so that the oxide forms as a solid and does not evaporate; good adherence to the metal substrate aided by a thermal expansion coefficient close to the alloy
- Enough high-temperature plasticity to resist fracture induced by differential thermal expansion strains

- High melting temperature
- High thermodynamic stability (highly negative Gibbs free energy of formation) so it forms preferentially to other products
- Low diffusion rate of cations and anions leading to a slow growth rate

In order to achieve the aforementioned high thermodynamic stability of a protective oxide layer at a given temperature, the oxygen partial pressure of the gaseous environment must be sufficiently high *[6]*.

The Pilling-Bedworth theory was proposed in 1923, and suggested that an unprotective oxide layer forms if the volume of the oxide layer is less than the volume of the metal substrate reacted with. As an example, for the oxidation of chromium, Equation 2.5 applies:

$$2Cr + \frac{3}{2}O_2 \rightarrow Cr_2O_3 \qquad \textbf{Equation 2.5}$$

for which the Pilling-Bedworth ratio is as in Equation 2.6:

$$\frac{\text{Volume of 1 mole of } Cr_2O_3}{\text{Volume of 2 moles of Cr}} \qquad \textbf{Equation 2.6}$$

The theory states that if the ratio is less than 1, then the oxide layer will be unprotective, with the scales being cracked or porous due to tensile stresses *[1, 4, 5]*. If the volume ratio is greater than 1, as in the case of Cr_2O_3 for which the ratio is 2.02, then according to the theory the oxide layer will be protective *[1, 4, 5]*. If the ratio is much greater than 2, then compressive stresses develop in the

oxide layer as it grows, and may cause the oxide layer to spall off *[1, 4, 5]*. There are exceptions to the Pilling-Bedworth theory, and many scientists do not accept it *[4]*.

2.2.3 Oxidation Rate

The kinetics of an oxidation process must be considered along with the thermodynamics when assessing the suitability of a material for high temperature use *[7]*. The rate of oxidation of a given alloy can be described by three kinetic laws, as shown in Figure 2.2: parabolic, linear and logarithmic *[4]*. The weight gain during oxidation is proportional to oxide thickness *[4, 7]*, but must be interpreted with caution if spalling or evaporation may occur. If a protective oxide is formed, and it is ideally dense, continuous and adheres to the metal over the entire surface, then the Wagner Theory of Oxidation applies, in which a parabolic rate law governs the growth of an oxide *[1, 4, 5]*.

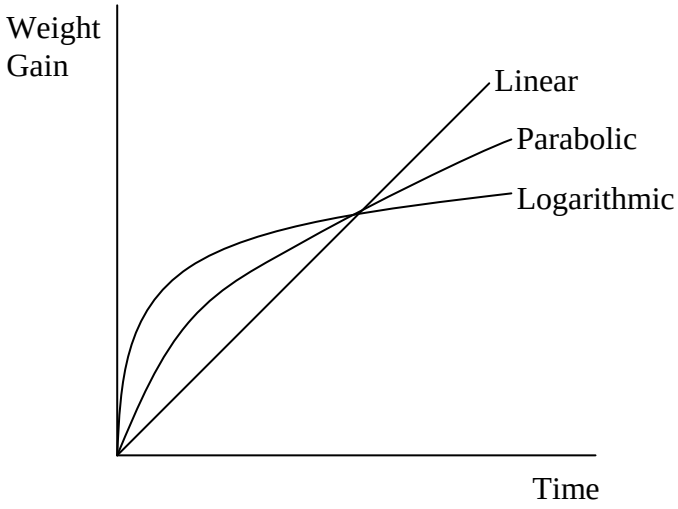

Figure 2.2: Common kinetic laws for the rate of growth of an oxide layer *[4]*

One form of the parabolic rate law is given in Equation 2.7, in which the square of the film thickness x, is proportional to time t, and k_p is the parabolic rate constant. During parabolic growth, the rate of oxidation is limited by solid-state diffusional transport of the reactant or electrons

through the scale, and as the scale grows in thickness the distance for diffusion increases, such that the reaction rate decreases with time *[1]*. Figure 2.3 shows the solid state diffusion which occurs during the growth of an oxide layer, and shows the area for oxide growth depending on the circumstance. If the metal ions diffuse more quickly across the scale than the oxygen ions, then the scale grows at the oxygen-scale interface, while if the oxygen ions diffuse more quickly, then the growth occurs at the metal-scale interface. In the case of a porous or cracked scale, then dissolved oxygen can come into direct contact with the metal, and growth will therefore occur at the metal-scale interface. Finally, if the diffusion of the metal ions and oxygen ions is at approximately the same rate, then growth could occur anywhere within the oxide scale *[7]*.

$$x^2 = k_p t$$ **Equation 2.7** ***[4]***

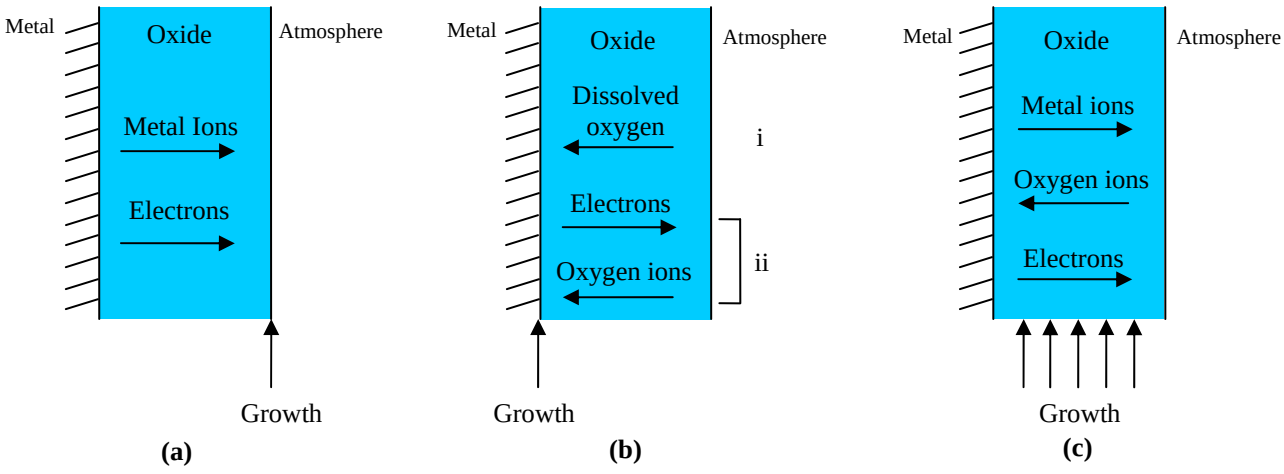

Figure 2.3: (a) If diffusion of the metal ions is faster than that of the oxygen ions then oxide growth will occur at the oxide-atmosphere interface. (b) If the oxide is porous or cracked then oxygen molecules can come into direct contact with the metal (i), and if not but the oxygen ions diffuse more quickly than the metal ions (ii), then growth will occur at the metal-oxide interface. (c) If the diffusion of both the metal and oxygen ions is at the same rate then growth will occur at any place in the oxide layer. *[7]*

The parabolic oxidation rate increases exponentially with temperature according to the Arrhenius rate law *[4, 5]* shown in Equation 2.8, in which k_o is a constant that is a function of the oxide composition and gas pressure, Q is the activation energy, R is the gas constant and T is the absolute

temperature. Oxygen partial pressure affects the parabolic rate constant according to Equation 2.9, in which C is a proportionality constant, and n is negative for *n*-type oxides, and positive for *p*-type oxides *[4]*. Chromium oxide (Cr_2O_3) is a *p*-type semiconductor with a metal excess *[4]*, and therefore has a positive n value in Equation 2.9, so the parabolic rate constant will increase with increasing oxygen partial pressure.

$$k_p = k_o \exp\frac{-Q}{RT} \qquad \textbf{Equation 2.8}$$

$$k_p = C(pO_2)^{1/n} \qquad \textbf{Equation 2.9}$$

If a reaction occurs at a the steel-gas interface, then linear kinetics may result, as shown in Figure 2.2 *[4]*. Linear kinetics have been observed in conditions of low oxygen partial pressure and in mixtures of CO/CO_2 *[4]*. During the opening stage of oxidation, if the oxide layer is thin enough, then linear oxidation kinetics will govern the reaction, until, as the film thickens, a transition to parabolic kinetics may occur *[4]*. A parabolic rate law can transform suddenly or gradually into a linear rate law if the metal surface is not protected by a layer of scale, in which case one of the steps in the oxidation process, rather than the rate of solid-state diffusion, will control the rate of oxidation *[4, 5]*. This situation may occur if a protective scale spalls off or cracks, if a non-protective porous scale develops, if the oxide is volatile or molten, or if the Pilling-Bedworth ratio is less than 1 *[5]*. At low temperatures, when a thin oxide film has formed (under 100nm), the oxidation rate usually follows logarithmic or inverse logarithmic kinetics *[4, 5]*. Logarithmic kinetics laws are rarely relevant to materials selection problems for corrosion properties *[4]*, and will therefore not be covered in depth here.

2.2.4 Chromia (Cr_2O_3) Layers

Generally, austenitic alloys with more than 17% chromium can form a protective scale consisting of an outer layer of spinel $(Mn,Fe)Cr_2O_4$ and an inner layer of chromia (Cr_2O_3) *[8]*. For maximum protection in high-temperature corrosion environments this scale must grow quickly to a sufficient thickness, and must not consist of iron oxides (Fe_2O_3 and $(Fe,Cr)_3O_4$), since an iron-rich oxide layer is not protective *[8]*. If there is not sufficient chromium available on the surface to form a pure Cr_2O_3 scale, then iron will take part in the oxidation and fast growing iron oxides and mixed (Fe,Cr) oxides (spinel phase) will be formed *[9]*.

Although chromia is the only solid chromium oxide that is thermodynamically stable at high temperatures, volatile chromium oxides may be important in the high-temperature oxidation of chromium. The evaporation of CrO_3, which is formed by the oxidation of Cr_2O_3 shown in Equation 2.10, is important at high oxygen partial pressures *[1]*.

$$\frac{1}{2}Cr_2O_3(s) + \frac{3}{4}O_2(g) = CrO_3(g) \qquad \textbf{Equation 2.10}$$

A consequence of the preferential oxidation of chromium, which leads to the development of a protective chromia layer on an alloy, is that zones depleted in chromium are subsequently created in the alloy. The chromium-depleted zones have an inferior resistance to oxidation and other forms of corrosion to those of the bulk steel, and are therefore particularly vulnerable to localized attack when an oxide scale cracks or spalls *[10]*.

2.2.5 Stress Relief in Oxide Layers

Stresses develop in oxide layers during growth, temperature change and creep, and must be relieved in some way *[5]*. Stress may be relieved by the development of porosity in the scale, plastic deformation of the alloy or scale, cracking of a brittle scale, or separation of the scale from the metal when the internal stress exceeds the adhesive interfacial forces *[5]*. The stresses generated in an oxide layer during growth and thermal cycling are described here.

2.2.5.1 Growth Stresses

The growth of a scale leads to the development of large growth stresses and strains in the scale, due to several causes, and the stresses tend to be compressive *[1]*. The proposed mechanisms for growth stresses include *[11]*:

- Volume differences between the oxide and substrate, as described by the Pilling-Bedworth theory
- Epitaxial stresses that occur when the scale is very thin
- Changes in composition in the scale or alloy
- A gradient in the number of point defects across a scale that result in lattice-parameter variation across the scale
- Oxide formation within scale grain boundaries
- Specimen geometry due to curvature

2.2.5.2 Mechanism of Spalling

Spallation of an oxide layer does not usually occur under tensile stress, but occurs frequently when under compressive in-plane stress, by either a ‘buckling’ or ‘wedging’ process *[12]*. During compression, in order for a particle of spalled oxide to be released from a scale, interfacial adhesion

between the metal and oxide layer must be lost and through-thickness cracking must occur in the scale *[10]*. In compression, there are two different routes by which spalling can occur, and a summary of these is given in Figure 2.4 *[10, 12]*.

For Route I in Figure 2.4, the oxide-metal interface is assumed to be stronger than the oxide itself, and the oxide initially fails by compressive shear cracking. Differential contraction strains, caused by further cooling, then force wedges (hence the term 'wedging') of the adjacent oxide layer under the segment affected by the cracks, thereby gradually creating decohesion at the metal-scale interface *[10, 12]*. For Route II in Figure 2.4, the interfacial adhesion between the oxide and metal is assumed to be poor, and therefore buckling will occur during compression. Spallation then results when cracking occurs in areas of high tensile stress within the oxide. Buckling has been found to be an unlikely spallation mechanism for oxidation-resistant alloys. This is because areas of decohesion at the oxide-metal interface are small, and because buckling is not likely for oxide thicknesses greater than 0.5μm *[12]*.

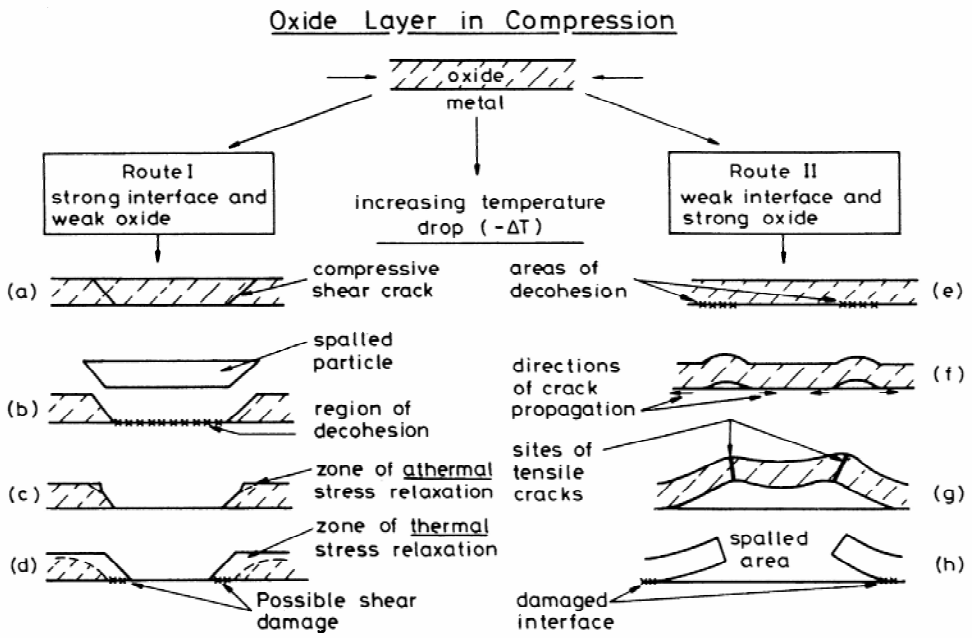

Figure 2.4: Routes leading to the cracking and spallation of oxide layers, caused by compression *[12]*

2.2.5.3 Thermal Cycling Stresses

Thermal cycling can have a detrimental effect on the performance of protective oxide layers due to the development of differential strains between the oxide and substrate, which may induce tensile or compressive in-plane stresses within the scale. The differential strains are caused by the difference in thermal expansion coefficients between the metal phase and the oxide. For example, in the range from 100-1000°C the linear coefficient thermal expansion for chromia (Cr_2O_3) is $7.3x10^{-6}$, while between 0-1000°C it is $9.5x10^{-6}$ for chromium *[5]*. If, as is the case for chromia, the thermal expansion coefficient for the metal is greater than that for the oxide, then cooling induces compressive stresses in the oxide layer, whereas heating generates tensile stresses *[12]*.

Tensile stresses can cause cracking, but are unlikely to cause spallation, whereas compressive stresses can easily cause spallation by wedging or buckling, as described previously. The most likely process for spallation in high temperature alloys is wedging. The critical temperature drop to induce spallation for the wedging process decreases with increasing oxide thickness *[12]*, so spallation becomes more likely over time as the oxide layer gains thickness, since a smaller temperature drop is required to induce spallation.

In cyclic oxidation conditions, the performance of an alloy depends mainly on scale adherence, which is affected by scale morphology, as well as alloy and scale compositions *[2]*. Once the scale starts to crack and deteriorate due to stresses and poor adherence, breakdown occurs and the useful service life of the alloy is over. Breakdown occurs in a chromia-forming alloy when the concentration of chromium at the scale-alloy interface, necessary for scale healing and reformation, goes below a critical concentration *[2]*. Many factors must be taken into account when predicting the lifetime of alloys exposed to thermal cycling, such as scale growth rate, cracking and spalling of the oxide layer, and subsurface changes in composition of the alloy *[2]*.

Figure 2.5 shows the change in weight with time for a typical chromia-forming alloy undergoing cyclic oxidation. An initial weight gain, corresponding to the growth of the oxide layer, usually occurs as shown between points 0 and a in Figure 2.5. After reaching the thickness at point a, or a certain number of cycles, the oxide layer partially spalls, and weight loss occurs. The extent of weight loss depends on the amount of spalling that takes place relative to the amount of scale healing and reformation that occurs, as shown between points a-c. Eventually the scale stops healing so that the weight change is negative, and protective scale breakdown occurs when the chromium content at the scale-alloy interface is reduced below a critical level of chromium, as at point c in Figure 2.5 *[2]*.

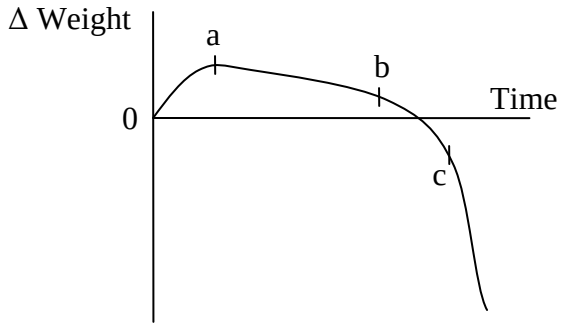

Figure 2.5: Characteristic long-term cyclic oxidation behaviour of a chromia-scale forming alloy *[2]*

2.2.6 Structure and Texture of Oxide Layers

Oxide layers have either a crystalline or non-crystalline structure. Non-crystalline materials can be either amorphous or vitreous, where the term amorphous refers to a frozen state without short-range order, and the term vitreous denotes glassy materials with short-range order but no long-range order *[1]*. Vitreous oxide layers are not restricted by epitaxial effects, and can therefore form on various types of substrates, including polycrystalline substrates *[1]*. Although several oxides have a vitreous structure at low temperatures, the only oxide to have a vitreous structure at high temperature is silica (SiO_2), so the formation of polycrystalline scales is a more important aspect of

high-temperature corrosion *[1]*. Epitaxy refers to the growth of an oxide which aligns its crystal structure to be compatible with the structure of the metal substrate, and finds the best fit rather than a perfect fit *[5]*. Stresses develop in the epitaxial oxide layer as it grows due to a misfit between the oxide and metal crystals. Stress increases as the oxide layer grows in thickness, until eventually the bulk scale becomes polycrystalline and the exitaxy is lost, which seldom occurs at a thickness over 100nm *[5]*.

2.3 High-temperature Corrosion

The main forms of high-temperature corrosion are oxidation, carburisation and metal dusting, nitridation, halogen corrosion, sulfidation, ash/salt deposit corrosion, molten salt corrosion and molten metal corrosion *[13]*. The forms of high-temperature corrosion relevant to this thesis are oxidation, carburisation and nitridation, and will therefore be described in this section.

2.3.1 Oxidation

Oxidation is the most commonly encountered form of high-temperature corrosion. Oxidation is not always detrimental, since most corrosion and heat resistant alloys rely on external oxidation in the form of a protective oxide film in order to provide resistance to forms of high-temperature corrosion such as carburisation and nitridation *[13]*. The aim of high-temperature alloys is to avoid excessive metal loss by scale formation (external oxidation), and to minimise the penetration of oxidation products into the alloy (internal oxidation), as internal oxidation reduces the load bearing area of an alloy *[13]*.

An environment can be classified as either “oxidising” or “reducing”, depending on the extent of oxygen activity in the atmosphere. An oxidising atmosphere has a high oxygen activity, and

contains molecular oxygen (O_2), while a reducing atmosphere is characterized by low oxygen activity, and is controlled by the partial pressure ratios, P_{H_2} / P_{H_2O} or P_{CO} / P_{CO_2}. A reducing atmosphere causes an increase in corrosion by modes such as carburisation and nitridation, since the development of a protective oxide layer is impaired *[13]*.

The most common way of improving oxidation resistance is to increase the chromium content of an alloy, although additions of other elements including aluminium, silicon and some of the rare earth elements can also enhance oxidation resistance *[14]*. An increase in the nickel content of up to about 30% in Fe-Cr-Ni alloys, with relatively constant chromium content, dramatically reinforces the effect of chromium on oxidation resistance *[13]*. The oxidation of metals and alloys is strongly influenced by cold work. For Incoloy 800H, an increase in cold work resulting in a decrease in oxidation has been reported, in contrast to results reported for AISI 304 *[15]*.

2.3.2 Carburisation

Carburisation occurs when alloys are exposed at elevated temperatures to an environment rich in carbon, such as an atmosphere of carbon monoxide, ethane or other hydrocarbons *[13]*. Carbon in the atmosphere diffuses into the base metal and reacts with carbon active elements such as chromium, silicon, aluminium or iron to form carbides within the grains and along grain boundaries. The ductility and toughness of an alloy deteriorates through carburisation, especially at low temperature, and the formation of internal carbides leads to a volume increase which generates additional stresses *[3]*. The thermodynamic likelihood for an alloy to be carburised or decarburised depends on the carbon activity (a_c) of both the environment and of the alloy. If the carbon activity of the environment is greater than that of the steel, then the steel will be carburised, and the converse also holds true *[5, 13]*.

The main protection mechanism against carburisation for an austenitic alloy is the formation of a protective oxide scale made up of Cr_2O_3 and $(Fe,Mn)Cr_2O_4$, as the solubility of carbon in such oxides is almost nil and carbon permeation through the scale is extremely slow *[3]*. An increase in nickel content has been observed *[16]* to improve carburisation resistance in iron-nickel-chromium alloys. This is due to a reduction in the diffusivity and solubility of carbon with increasing nickel content, as demonstrated by Demel *et al. [13]*. Silicon also has an important role in improving carburisation resistance, due to the formation of a SiO_2 inner layer beneath the chromia layer, which can increase the high-temperature carburisation resistance of alloys *[17]*. Small additions of minor alloying elements, such as titanium and rare earth elements, can further improve an alloy's resistance to carburisation *[13]*. Surface finish can have a very important effect in carburisation reactions. Lai *[13]* states that improvements in surface finish by machining can significantly increase an alloy's carburisation resistance.

Carburisation is very non-uniform and the degree can vary dramatically, making it difficult to interpret measurements of carburisation. Carburisation causes normally non-magnetic heat resistant alloys to become magnetic, so the resulting magnetic permeability can be used to assess the degree of carburisation that has occurred *[14]*.

2.3.3 Nitridation

Similar to carburisation, nitridation occurs when nitrogen from the environment is absorbed at the metal surface and diffuses into the interior of the metal, and metal loss does not occur. If the solubility limit for nitrogen in the alloy is exceeded, then nitride precipitates form with chromium and other elements. Nitridation can have a negative impact on the ductility and toughness of steel, as nitrides can cause the steel to become brittle *[13]*. Nitridation usually occurs at high temperatures, when steel is either exposed to an ammonia-bearing environment, or a nitrogen-base

environment exposed to an environment with a low oxygen partial pressure. As with carburisation, higher nickel alloys are very resistant to nitridation attack due to the low solubility and diffusivity of nitrogen in nickel *[5, 13]*.

The nitridation of steel exposed to nitrogen gas at high temperature proceeds according to Equations 2.11 and 2.12, where k is the equilibrium constant and P_{N_2} is the partial pressure of nitrogen in the atmosphere. Hence in nitrogen-rich atmospheres, the nitriding potential is proportional to $(P_{N_2})^{1/2}$, so an increase in the partial pressure of nitrogen leads to an increase in the thermodynamic potential for nitridation to occur.

$$\tfrac{1}{2} N_2(g) \Leftrightarrow [N] \text{ (dissolved in metal)} \qquad \textbf{Equation 2.11 } \textit{[13]}$$

$$[\%N] = k(P_{N_2})^{1/2} \qquad \textbf{Equation 2.12 } \textit{[13]}$$

Oxygen partial pressure can have an important effect on nitridation. A study by Odelstam *et al. [18]*, the results of which are shown in Figure 2.6, found that nitride penetration into 253MA was significantly increased when the oxygen partial pressure in nitrogen was reduced from 205 to 43ppm. However, the change in oxygen partial pressure had little effect on the depth of nitride penetration into alloy 800H *[18]*.

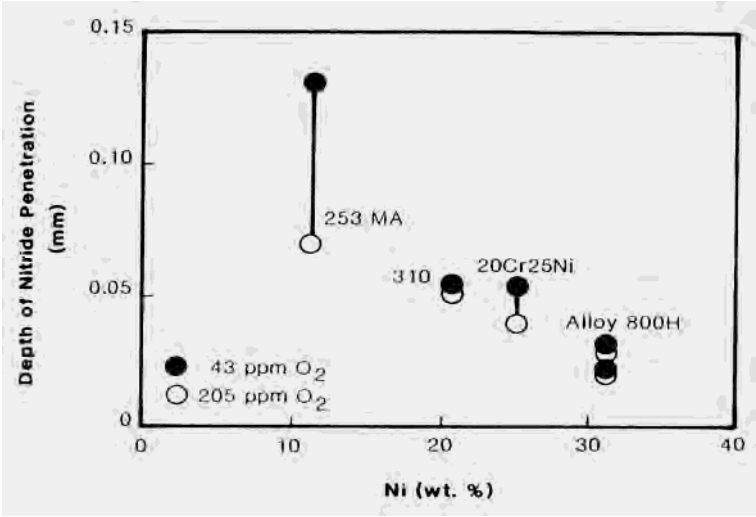

Figure 2.6: Results of nitridation tests in nitrogen with two different levels of oxygen content at 825°C for 400 hours

2.3.4 Effect of Grain Size on High-temperature Corrosion

Grain size has an important effect on the kinetics of high-temperature corrosion, as diffusion through grain boundaries is magnitudes faster than through the bulk material. A reduction in grain size leads to a higher proportion of grain boundaries or fast diffusion paths, so a smaller grain size leads to increased oxidation attack for low-chromium steels, due to an increase in oxygen diffusion through grain boundaries *[19]*. On the other hand, the high-temperature oxidation resistance of austenitic steel (with higher chromium content) is improved by smaller grain sizes, due to the increased outward flux of chromium along grain boundaries, which promotes the formation of protective chromium-rich oxide scales (Cr_2O_3 and/or $FeCr_2O_4$). As a result, fine-grained materials require a smaller chromium concentration than coarse-grained materials in order to form a protective Cr_2O_3 scale over the entire surface *[19]*.

2.4 Phases Formed During High-temperature Aging

2.4.1 Phases Formed in Austenitic Alloys at Elevated Temperature

A number of phases can develop in austenitic alloys when aged at high temperature; all phases relevant to this thesis are listed in Table 2.1, which includes the space group and lattice parameters for each phase. Figure 2.7 shows a ternary phase diagram of the precipitate phases present at 900^{o}C in an iron-chromium-nickel alloy, including the placement of Alloy 800H, 310 and 253MA. The placement of the alloys in the phase diagram shows the susceptibility of AISI 310 stainless steel to the formation of sigma phase, and the relative resistance of Incoloy 800H to the formation of sigma phase. This phase diagram does not account for the presence of carbon and alloying agents, and assumes thermodynamic equilibrium, and as such can only be used as a rough indication of phases that may be present during aging in service.

Table 2.1: The composition, space group and lattice parameters for phases relevant to this thesis that occur in austenitic alloys *[5, 20, 21]*

Phase	*Composition*	*Space Group*	*Lattice Parameter (nm)*
$M_{23}C_6$	$(FeCr)_{23}C_6$	225	a=1.057-1.068
MC	NbC; TiC	225	a=0.430-0.470
MN	CrN	225	a=0.4144
M_2N	Cr_2N	162	a=0.4796, c=0.4470
γ'	$Ni_3(Ti,Al)$	221	a=0.3561 for pure Ni_3Al to 0.3568 for $Ni_3(Al_{0.5}Ti_{0.5})$
σ	FeCr; $(Fe,Ni)_x(Cr,Mo)_y$	136	a=0.8799-0.9188, c=0.4544-0.4599

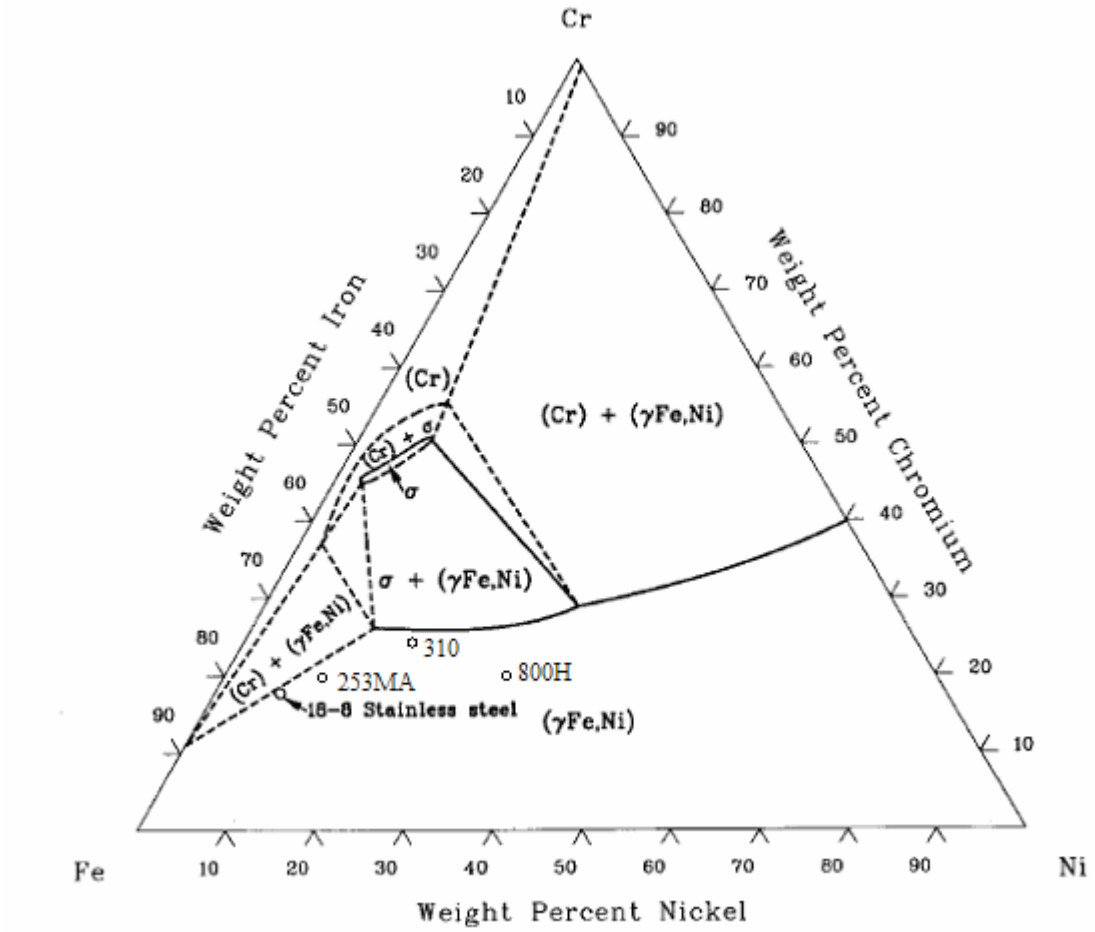

Figure 2.7: The isothermal section at 900°C of the iron-chromium-nickel ternary phase diagram, showing the nominal composition of 18-8 Stainless Steel, 253MA, 800H and 310 ***[20]***

2.4.2 Intermetallic Phases

Sigma Phase (σ)

Sigma phase is a hard, brittle intermetallic phase of nominal composition FeCr which forms in austenitic alloys. It generally appear after long exposure times in the temperature range from 565 to 980°C, although this can vary depending on processing and composition *[20]*. Sigma phase has a complex tetragonal crystal structure with 30 atoms per unit cell *[20, 22]*. Molybdenum, chromium, titanium and silicon (all ferrite-stabilisers), encourage the formation of sigma phase, whereas austenite stabilisers (such as nickel and carbon), inhibit it *[20, 23]*. Precipitation of sigma phase can cause embrittlement, which leads to a reduction in ductility and notch toughness at both room

and elevated temperatures. The extent of embrittlement caused by the precipitation of sigma phase depends on the amount and distribution. Grain boundary precipitation of the sigma phase is more detrimental than intragranular precipitation, which can actually increase creep ductility *[22]*.

Gamma Prime (γ'):

Gamma prime is an intermetallic strengthening phase found in iron-nickel-base alloys such as Incoloy 800H, with the chemical formula $Ni_3(Al,Ti)$. Precipitation of γ' contributes to high-temperature strength and creep resistance of the material, with the strength increasing as the γ' volume fraction increases. The volume fraction of γ' in iron-nickel-base alloys is usually less than 25% *[5]*.

2.4.3 Carbide Phases

$M_{23}C_6$ carbides

$M_{23}C_6$ carbide has a complex face-centered cubic structure with 92 metal atoms and 24 carbon atoms per unit cell *[22]*. If strong carbide formers such as niobium and titanium are not present, then $M_{23}C_6$ is the main precipitate formed in the 300 series of austenitic stainless steels. $M_{23}C_6$ is mainly made up of chromium such that the composition is $Cr_{23}C_6$, although other elements can partially substitute for chromium, so the general composition can be written as $(Cr,Fe,Mo)_{23}C_6$. When $M_{23}C_6$ precipitation occurs in the presence of more stable MC carbides (such as in 800H), it tends to be delayed *[22]*.

MC carbides

When elements such as niobium and titanium are added to an alloy in an amount ideally stoichiometric with the amount of carbon present, thermal aging leads to the precipitation of NbC and TiC, respectively *[20]*. To avoid sensitisation (see Section 2.5.1), a heat treatment is given

prior to service in order to precipitate MC. MC precipitation reduces the matrix carbon content available to form $M_{23}C_6$ and therefore reduces sensitisation *[20]*.

2.4.4 Nitride Phases

Low temperature nitridation usually results in a surface layer of nitrides comprised mostly of the iron nitrides Fe_2N and Fe_4N *[13]*. High-temperature nitridation results in internal nitrides of the form CrN, Cr_2N and/or $(Fe,Cr)_2N$ *[13]*. Aluminium is a very strong-nitride former so AlN, a needle phase, can be found in alloys such as 800H that contain aluminium *[13]*. Tests have found that AlN and Cr_2N may be found in nitrided 800H *[13]*. Nitrogen may replace the carbon in carbides, reducing the net nitrogen level, whilst TiN and Ti(CN) may be found in alloys stabilised with titanium. It has been found that when both MC and MN are present in an austenitic stainless steel, the high solubility of nitrides leads to considerably faster rates of coarsening for MN precipitates than MC precipitates during high-temperature thermal aging *[23]*.

2.5 Non-metallic Inclusions

Inclusions created during the steelmaking process can be expected even in the best steels *[24]*. Inclusions originate during part of the steel-making process, and are used to remove non-metallic elements such as oxygen from the steel at solidification. Not only is the amount of inclusions important to the properties of steel, but also their size, shape, composition and distribution *[25]*. The most detrimental type of inclusion for mechanical properties is manganese sulfide (MnS), followed by inclusions of Al_2O_3 and calcium aluminates *[26]*.

Sulfides and oxides are often arranged in groups called ‘stringers’. A stringer is an elongated body made up of non-metallic inclusions aligned in the direction of working (usually hot rolling) in wrought materials. The presence of stringers in materials is usually undesirable, as they cause the material to be brittle and have anisotropic properties.

The addition of rare-earth elements can be used to eliminate alumina and manganese sulfide inclusions *[26]*. Elements such as cerium have a greater affinity for sulfur than manganese, and the resulting rare-earth sulfides have different morphology and characteristics to usual sulfide inclusions. Rare-earth sulfides are solid at the moment of solidification, and are small and dispersed within the iron matrix. They are harder and therefore less deformable than manganese sulfides, which reduces the anisotropy of mechanical properties *[25]*.

2.6 Austenitic Stainless Steel

Austenitic stainless steels are essentially Fe-Cr-Ni steels with a face-centred cubic (FCC) structure that is attained through the addition of austenite stabilising elements such as nickel, manganese and nitrogen. Of all the types of stainless steel, austenitic stainless steel has the highest strength at high temperatures, and is therefore commonly utilised in high temperature applications. Austenitic stainless steels are nonmagnetic in the annealed condition, and can only be hardened by cold work. Stainless steels are susceptible to forms of thermally induced embrittlement such as sigma-phase embrittlement and sensitisation. Embrittlement refers to the severe loss of toughness or ductility, or both.

2.6.1 Sensitisation of Austenitic Stainless Steel

Austenitic stainless steel becomes susceptible to sensitisation when in the temperature range between 480 and 815°C *[5]*. Sensitisation is a breakdown in corrosion resistance associated with the precipitation of chromium-rich carbides such as $M_{23}C_6$ and M_7C_3 along grain boundaries. Interstitial carbon can diffuse rapidly to and within grain boundaries, while chromium diffuses much more slowly. This results in a chromium depleted zone adjacent to grain boundaries, as shown in Figure 2.8, caused by the formation of chromium carbides which remove chromium from solution.

The depletion of chromium places the grain boundary region in a "sensitised" state, with the depleted region anodic with respect to the bulk material, which results in accelerated corrosion along the grain boundaries. Sensitisation can lead to severe intergranular corrosion in situations where the alloy is exposed to an environment capable of attacking the alloy *[20]*. In general, a slight increase in tensile strength occurs, while embrittlement is caused to varying extents, depending on the situation *[20]*.

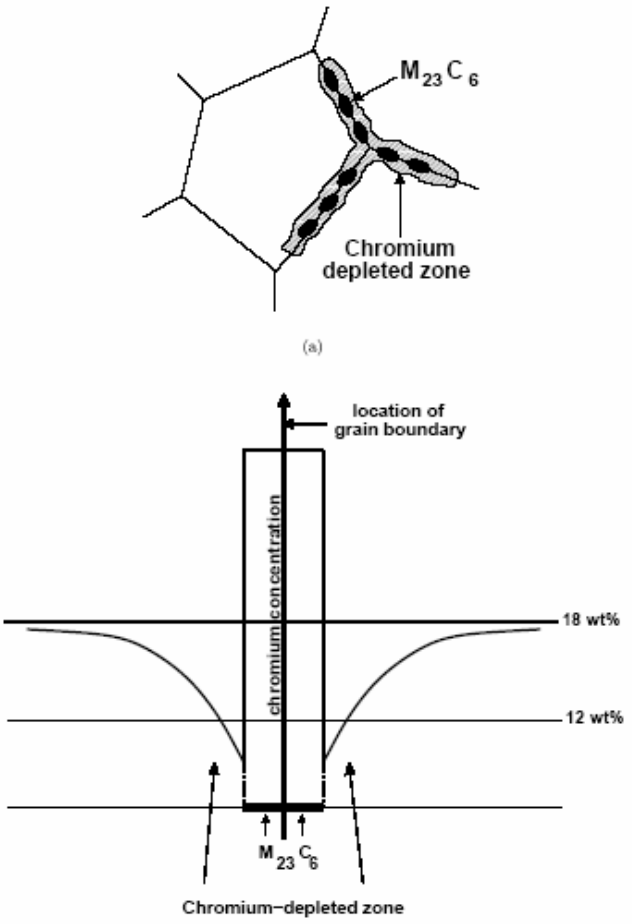

Figure 2.8: Schematic diagram showing the chromium depletion at a grain boundary *[27]*

The precipitation of chromium carbides can be controlled by reducing the carbon content of the steel, or by adding stabilising elements such as titanium and niobium. A reduction in carbon content to below 0.03% will prevent sensitisation during welding and heat treatment, but is not sufficient to prevent sensitisation during long-term aging *[20]*. Stabilising elements help prevent sensitisation by forming carbide and nitride precipitates, thereby reducing the amount of dissolved carbon available for chromium carbide formation. In order to stabilise an alloy, a stabilising heat treatment is conducted at a temperature where carbides of titanium and niobium are stable, but chromium carbides are unstable, so that carbon is taken out of solution, and chromium carbide precipitation is prevented at lower temperatures *[20]*.

This section described the chromium-depletion theory for sensitisation. However, it should be noted that there has been contention regarding the mechanism for sensitisation. The chromium-depletion theory was widely accepted until the electron microprobe was developed in the 1950s. Researchers could not confirm the theory with this technology, which prompted a number of alternative theories to explain sensitisation, such as strains at the carbide-austenite interface, and grain-boundary stain energy acting as the driving force for intergranular attack.

A further complication was the occurrence of intergranular corrosion in non-sensitised stainless steels with no evidence of grain-boundary precipitation. This lead to the proposal that intergranular corrosion of austenitic stainless steels was due to the segregation of impurity elements, such as phosphorus, to the austenite grain boundaries. Direct evidence of impurity segregation has been obtained from intergranular fracture surfaces. The advent of scanning transmission electron microscopes with electron beams of around 10nm, used in conjunction with energy-dispersive spectroscopy, provided direct proof of chromium depletion due to carbide precipitation at grain boundaries in the 1980s *[20]*.

2.7 Superalloys

Superalloys can be either nickel-, iron-nickel-, or cobalt-based, and are used at temperatures above about 540°C. They exhibit a combination of high-temperature corrosion resistance and stress-rupture strength unparalleled by any other alloy system. Iron-nickel base alloys such as Incoloy 800H are based on stainless steel technology, with alloying additions made according to alloy requirements *[5]*.

2.8 The Alloys Sandvik 253MA, Incoloy 800H and AISI 310

Three alloys were investigated during this thesis; two were the austenitic stainless steels Sandvik 253MA and AISI 310, and the third was Incoloy 800H, an iron-nickel base superalloy strengthened mostly by solid solution. The thesis was primarily a material selection problem in which the aforementioned alloys' high-temperature corrosion performance was assessed. The compositions of the three alloys are given in Table 2.2. The nickel content of the three alloys is substantially different, with the levels increasing from approximately 10% nickel in 253MA, to approximately 20% in 310 and 31% in 800H.

Table 2.2: Composition (weight percent) of the alloys Sandvik 253MA, AISI 310 and Incoloy 800H, taken from the materials certificates

Steel Type	Ni	Cr	C	Mn	S	P	Si	Mo	Ce	N	Al	Ti	Cu	Fe
253MA	10.74	20.8	0.07	0.65	<0.0005	0.023	1.53	-	0.05	0.159	1	-	-	Bal
310	19.23	24.37	0.046	1.25	0.001	0.023	0.62	0.29	-	0.031	-	-	0.29	Bal
800H	31.49	20.31	0.07	0.77	0.001	-	0.24	-	-		0.58	0.49	0.15	45.95

2.8.1 Comparison of Some Properties for Alloys 253MA, 800H and 310

Table 2.3 gives a comparison of some important parameters for the three alloys. The mean coefficient of thermal expansion is similar for all three alloys, so a difference in performance during thermal cycling would have to be attributed to other alloy properties, such as adherence of the oxide layer to the substrate. The table shows that while alloys 253MA and 800H have similar yield and creep strengths, both the yield strength and creep strength of alloy 310 are significantly inferior to the other two alloys. Typical grain sizes for the alloys vary from a coarser ASTM 2 (corresponding to an average grain diameter of 180μm), to a finer ASTM 6 (average grain diameter of 45μm). The

superalloy Incoloy 800H is the most costly alloy, with a cost 1.5 times that for 253MA quarter inch plate, and 1.15 times that for 310 plate *[28]*.

Table 2.3: Relevant data for alloys 253MA, 800H and 310 *[28]*

Property	253MA	800H	310
Mean Coefficient of Thermal Expansion (m/m K) at 900℃	1.9E-05	1.8E-05	1.9E-05
0.2% Yield Strength (MPa) at 900℃	125	128	84
Stress to rupture in 1,000 hours (MPa) at 900℃	30	33	23
Typical ASTM Grain Size	3-6	2-4	3-4
Relative Cost*	1.15	1.5	1

*1991-1992 prices/lb., 1/4-in. plate.

2.8.2 Sandvik 253MA

Sandvik 253MA, also referred to as alloy 253MA, is an austenitic stainless steel that was developed by Avesta AB for high-temperature applications. The high silicon content and cerium additions, which reduce the rate of oxidation, result in an alloy suitable in temperatures up to 1100°C, despite the low nickel content (of 11%) *[29]*. The creep strength of 253MA is superior to that of 310, and competes with 800H at temperatures above 900°C *[29]*. The high creep strength is attributed to its comparatively high nitrogen and carbon content *[18, 29]*. Nitrogen also reduces the tendency for the formation of sigma phase, and allows for a fully austenitic structure *[18]*.

Certain phases have been shown to precipitate in 253MA during aging at high temperatures. Andersson and Odelstam *[18]* found that aging at 800°C for 1000 hours resulted in the precipitation of $M_{23}C_6$ in grain boundaries and within the grains, while to some extent Cr_2N formed within the

grains. Longer aging times were found to result in the precipitation of sigma phase, but to less of an extent than in alloy grades such as AISI 310.

The addition of silicon and the rare earth metal cerium contributes to the good oxidation resistance of 253MA. Cerium reduces the rate of oxide growth by promoting the growth of a continuous silica (SiO_2) subscale beneath the chromia scale *[18]*. Silicon additions improve oxidation kinetics, and a silicon-rich scale (SiO_2) slows the diffusion of iron cations through the oxide scale *[30]*. However, silicon has been shown to increase oxide spallation during cyclic oxidation, an effect offset by the addition of cerium *[30, 31]*. 253MA has excellent resistance to oxide growth and spalling under cyclic conditions in air, in comparison to AISI 310 *[18]*. Rare earth metals such as cerium are believed to contribute to the oxidation resistance of austenitic Cr-Ni alloys by the following mechanisms: decreasing the rate of oxide growth, promoting the nucleation and initial growth of the oxide layer, creating a finer oxide grain size, and leading to better scale adherence *[32]*.

2.8.3 Incoloy 800H

Incoloy alloy 800H is an austenitic iron-nickel-based superalloy which has good strength and corrosion properties at high temperatures. The composition of alloy 800H (given in Table 2.2) is very similar to that of alloy 800, with the difference that the carbon content of alloy 800H is more restrictive (0.05-0.10%) than alloy 800 (0-0.10%) *[33]*. Alloy 800H is also heat treated such that a coarse grain size is produced, with an average size of ASTM 5. The higher carbon content and coarser grain size provide 800H with greater high-temperature strength.

The excellent oxidation resistance of alloy 800H is attributed to high nickel and chromium content, with the high nickel content ensuring good adherence of the protective chromia scale *[33]*. Titanium is added to 800H to act as a carbide- and nitride-former, thereby encouraging the

precipitation of titanium nitrides and titanium carbides. The formation of titanium carbide takes carbon out of solution that could otherwise react with chromium to form chromium carbides in a process known as sensitisation (see Section 2.5.1).

The resistance of alloy 800H to the formation of sigma phase is superior to that of alloy 310. After aging at 760°C for 1000 hours, alloy 310 showed a drastic reduction in toughness due to the formation of sigma phase, while alloy 800H remained almost unaffected *[33]*. At temperatures between 700 and 800°C, both $M_{23}C_6$ and TiC are commonly present. Although TiC is more thermodynamically stable at these temperatures, the kinetics frequently favour the formation of $M_{23}C_6$ *[34]*. One study showed *[34]* that aging at 850°C for 500 hours resulted in the grain boundary precipitation of $M_{23}C_6$, which in turn reduced the notched impact strength of the alloy at temperatures between 20 and 800°C. The same study showed that with an increasing degree of carburisation, the impact strength of the alloy was progressively reduced. Other minor phases which have been detected in small amounts in alloy 800 are sigma phase and G phase *[34]*.

2.8.4 AISI 310

AISI type 310 is a 300-series chromium-nickel austenitic stainless steel based on type 304 stainless steel, with chromium and nickel additions for strength and oxidation resistance. It is well established that the austenitic stainless steel AISI 310 is susceptible to deleterious sigma phase formation during aging at elevated temperatures *[20, 22, 35]* which leads to significant embrittlement. The precipitation of sigma phase is usually preceded by the precipitation of carbides, and the rate of formation of sigma depends on many factors, including temperature, carbon content, degree of cold work and solution treatment temperature *[35]*. Several carburisation studies have been conducted on the performance of alloy 310 in varying CH_4/H_2 environments between the temperatures of 800 and 1100°C *[36-39]*. The studies investigated the effect of

varying temperature and carburising potentials on the extent of external oxidation, external carburisation and internal carburisation in the alloy.

2.8.5 Literature Comparing Alloys 253MA, 800H and 310

A large amount of literature can be found about the performance of various alloys subjected to various conditions. However, the majority of this literature does not include 253MA, 310 and 800H in direct comparison. No studies conducted at high pressure were found for these alloys. Studies conducted in nitrogen-based atmospheres are limited, and more studies in pure nitrogen are needed according to Lai *[13]*, as the majority of studies have been conducted in ammonia-bearing atmospheres. This section describes the direct comparisons in performance that could be found for the three alloys.

The carburisation resistance of 800H and 310 was tested in Ar-5H_2-5CO-5CH_4 at 870°C for 215 hours, 930°C for 215 hours and 980°C for 55 hours *[13]*. All three tests found that the mass of carbon pickup per unit area for 800H was far less than for 310. The results of a gas carburisation test conducted on all three alloys at 1000°C in 10% methane and 90% argon for 500 hours are shown in Figure 2.8 *[18]*. The test showed that Sandvik 253MA has a lower degree of carbon pick-up than the other two alloys, while AISI 310 has the highest degree of carbon pick-up under these conditions.

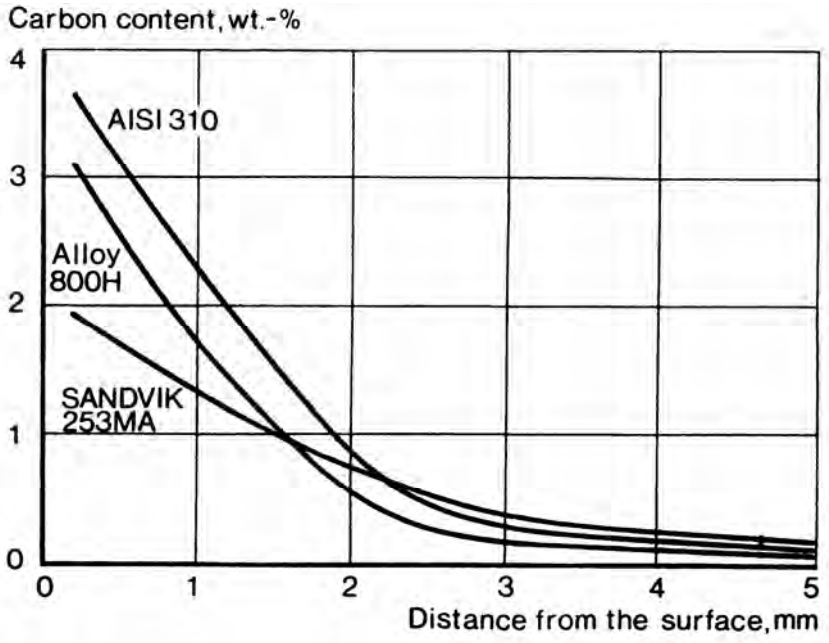

Figure 2.9: Carbon content profile for the alloys Sandvik 253MA, AISI 310 and Incoloy 800H after carburisation in 10% CH_4 and 90% Ar at 1000°C for 500 hours *[18]*

A cyclic oxidation test was conducted on the two alloys 800 (similar to 800H) and 310 in air at 980°C with 15-minute heating and 5-minute cooling cycles for 1000 hours *[13]*. The results showed that no appreciable weight loss occurred for either alloy until after approximately 600 hours, at which point type 310 began to lose weight at a greater rate than 800. After 1000 hours, Incoloy 800 had lost very little weight, while AISI 310 had had more than a 10% change in weight. Another cyclic oxidation test *[18]* conducted at temperatures between 1000 and 1150°C, compared the performance of 253MA and 310, and showed that the weight loss of 310 at all these temperatures was greater than the weight loss of 253MA, suggesting that 253MA is superior to 310 in cyclic oxidation conditions.

A nitridation test conducted by Andersson and Odelstam *[18]*, described previously in section 2.3.4 of this thesis, found that in pure nitrogen at 825°C for 400 hours, the depth of nitride penetration was least for 800H, and greatest for 253MA (see Figure 2.6). The oxygen partial pressure of the

environment significantly affected the performance of 253MA, while it did not have much effect on the performance of 800H and 310S (a low carbon version of 310).

2.9 The Effect of Alloying Additions on Spallation Behaviour

In order to be effective in cyclic oxidation conditions, an alloy should develop an oxide layer resistant to spalling. The variation in performance of various alloys under cyclic oxidation conditions is caused largely by differences in alloy content. The mechanisms by which chromium and nickel increase the high-temperature corrosion resistance of austenitic alloys were discussed previously in this literature review. Chromia-forming alloys also contain minor alloying additions that significantly affect alloy behaviour during oxidation and cyclic oxidation. Even a small variation in minor-alloy content can have a major effect on cyclic oxidation behaviour, and it is usually necessary to analyse the effects of minor elements collectively, rather than separately *[2]*. The oxides of minor additions such as Mn, Ti, Si and Al, are more thermodynamically stable than that of Cr, and therefore have a strong tendency to oxidise internally *[2]*. Internal oxidation and the formation of voids have been consistently found in commercial chromia-forming alloys during long-term cyclic oxidation *[2]*.

Studies have shown that aluminium has a beneficial effect on the spallation behaviour of chromia-forming alloys, but titanium has a detrimental effect. This is because growth kinetics of a chromia layer would be decreased by the formation of an Al_2O_3-rich layer beneath the chromia scale, whereas titanium tends to oxidise on grain boundaries in the subsurface region of an alloy *[2]*. Silicon is added for deoxidation purposes and to improve isothermal oxidation resistance, as additions of greater than 0.6% lead to the development of an internal silica (SiO_2) layer. This silica

layer decreases the rate of growth of the outer chromia layer, however, it has been shown to greatly worsen the extent of spallation during cyclic oxidation *[2]*. Manganese has little effect on the property and structure of Fe-Cr-Ni alloys, although it can influence oxidation behaviour by reacting with the chromia scale to form a $MnCr_2O_4$ spinel at the scale surface, which is less protective than chromia and therefore tends to decrease oxidation resistance *[2]*. The addition of small amounts of reactive elements such as cerium, promotes spallation resistance by suppressing cation diffusion through the scale, thereby improving scale adhesion *[2]*.

2.10 Discussion

This review revealed a lack of publications about the effects of an environment similar to that of a WhisperGen™ heater head. However, the review suggests that alloys with a higher nickel content, such as Incoloy 800H (~30% nickel) would generally perform better in a high-temperature environment than alloys with lower nickel contents, such as Sandvik 253MA (~10% nickel) and AISI 310 (~20%). Alloys with higher nickel content produce a more adherent oxide scale, which is more resistant to spalling. In addition, alloys with higher nickel content are more thermodynamically stable, and are therefore less susceptible to the formation of deleterious phases during aging. The disadvantage with higher nickel content is the associated increase in alloy price *[28]*.

This review has shown that the subject alloys have certain tendencies. AISI 310 is susceptible to the formation of embrittling sigma phase in the temperature range from 565 to 980°C, although this can vary depending on processing and composition. Alloys 253MA and 800H have similar yield and creep strengths, but both the yield strength and creep strength of alloy 310 are significantly

inferior to the other two alloys. The rare earth additions to 253MA encourage a more adherent oxide layer. Nevertheless, the relatively high silicon content of the alloy, and the relatively low nickel content, are likely to contribute to a lack of spalling resistance. Overall, one would expect Incoloy 800H to outperform the two alternatives, Sandvik 253MA and AISI 310.

References

[1] P. Kofstad, *High Temperature Corrosion*, Elsevier Applied Science Publishers Ltd, **1988**.
[2] B. Gleeson, B. Li, "Cyclic oxidation of chromia-scale forming alloys: Lifetime prediction and accounting for the effects of major and minor alloying additions", Les Embiez, France, **2004**.
[3] A. Rahmel, H. J. Grabke, W. Steinkusch, *Materials and Corrosion* **1998**, *49*, 221.
[4] D. A. Jones, *Principles and prevention of corrosion*, Macmillan Pub. Co. ; Collier Macmillan Canada ; Maxwell Macmillan International Pub. Group, New York, Toronto, New York **1991**.
[5] J. R. Davis, ASM International. Handbook Committee., *Heat-resistant materials*, ASM International, Materials Park, Ohio **1997**.
[6] R. A. Holm, H. E. Evans, *Werkst. Korros.*, *38*, 115.
[7] J. P. Schaffer, *The science and design of engineering materials*, WCB McGraw-Hill, Boston **1999**.
[8] C. Ostwald, H. J. Grabke, *Corrosion Science* **2004**, *46*, 1113.
[9] V. B. Trindade, U. Krupp, H. J. Christ, M. J. Monteiro, F. C. Rizzo, *Materialwissenschaft und Werkstofftechnik* **2005**, *36*, 471.
[10] H. E. Evans, R. C. Lobb, *Corrosion Science* **1984**, *24*, 209.
[11] N. Birks, G. H. Meier, F. Pettit, *High-Temperature Oxidation of Metals*, Cambridge University Press, Cambridge **2006**.
[12] H. E. Evans, *International Materials Reviews* **1995**, *40*, 1.
[13] G. Y. Lai, *High-Temperature Corrosion of Engineering Alloys*, ASM International, **1990**.
[14] D. J. Tillack, J. E. Guthrie, *Nickel Institute Technical Series #10071*
[15] J. C. Langevoort, L. J. Hanekamp, P. J. Gellings, *Applied Surface Science (1985)* **1987**, *28*, 189.
[16] S. K. Bose, H. J. Grabke, *Zeitschrift fuer Metallkunde* **1978**, *69*, 8.
[17] R. A. Rapp, *Corrosion* **1965**, *21*, 382.
[18] T. Andersson, T. Odelstam, *R&D Centre AB Sandvik Steel* **1984**.
[19] V. B. Trindade, U. Krupp, P. E. G. Wagenhuber, H. J. Christ, *Materials and Corrosion* **2005**, *56*, 785.
[20] J. R. Davis, ASM International. Handbook Committee., *Stainless steels*, ASM International, Materials Park, Ohio **1994**.
[21] P. Villars, L. D. Calvert, *Pearson's Handbook of Crystallographic Data for Intermetallic Phases*, ASM International, **1996**.
[22] A. K. Sinha, *Ferrous physical metallurgy*, Butterworths, Boston **1989**.
[23] P. Marshall, *Austenitic stainless steels : microstructure and mechanical properties*, Elsevier Applied Science, London **1984**.

[24] K. Farrell, E. D. Specht, J. Pang, L. R. Walker, A. Rar, J. R. Mayotte, "Characterization of a carburized surface layer on an austenitic stainless steel", **2005**.
[25] M. Olette, C. Gatellier, "Effect of Additions of Calcium, Magnesium or Rare Earth Elements on the Cleanness of Steels", presented at *Clean Steel*, Balatonfured, Hungary, **1981**.
[26] W. C. Leslie, *Transactions of the Iron & Steel Society of AIME* **1983**, *2*, 1.
[27] C. H. Too, in *Materials Science and Metallurgy*, Vol. Master of Philosophy, University of Cambridge, Cambridge **2002**.
[28] HAYNES International, *HAYNES HR-120 alloy*, HAYNES International Inc., **1998**.
[29] M. Yu, R. Sandstrom, *Scandinavian Journal of Metallurgy* **1988**, *17*, 156.
[30] P. Vangeli, B. Ivarsson, "Investigation of a new methodology in high temperature oxidation application to commercial austenitic steels", Les Embiez, **2001**.
[31] S. N. Basu, D. Nath, J. Tebbets, "Microstructural evolution of multilayered oxide scales on stainless steels", Boston, MA, USA, **1993**.
[32] Y. Maode, R. Sandstrom, *High Temperature Technology* **1988**, *6*, 153.
[33] D. E. Wenschhof, Jr., *American Society of Mechanical Engineers (Paper)* **1975**, 148.
[34] A. Czyrska-Filemonowicz, P. J. Ennis, *Nuclear Technology* **1984**, *66*, 149.
[35] A. V. Kington, F. W. Noble, *Materials Science & Engineering A: Structural Materials: Properties, Microstructure and Processing* **1991**, *A138*, 259.
[36] N. Tabet, I. Allam, R. C. Yin, *Applied Surface Science* **2003**, *220*, 259.
[37] R. Yin, *Corrosion Science* **2005**, *47*, 1896.
[38] R. Yin, *Materials Science and Engineering A* **2005**, *391*, 19.
[39] R. C. Yin, I. M. Allam, A. Al-Farayedhi, *Oxidation of Metals* **2003**, *60*, 315.

3 Experimental

3.1 Summary

This section describes the design, setup and testing undertaken during the experimental section of research. The aim of the experimental work was to simulate the environment of a WhisperGen™ heater head in a controlled laboratory setting, and then to compare these results with heater heads run in an actual engine. It proved impracticable to conduct tests at a pressure of 24 bar. Therefore, the equilibrium carbon and nitrogen chemical potentials of the working gas at 24 bar were determined via Thermo-Calc™. Gas mixtures with the same chemical potential at 1 bar as would have been experienced at 24 bar were obtained. The experiments were then conducted in a tube furnace at temperatures of 900, 800 and 700°C with the gas mixture continuously flowing over the coupons.

3.2 Design of Experiments

3.2.1 Laboratory Experiments

A set of experiments was designed to simulate the heater head environment, the results from which were subsequently compared with heater heads run in a WhisperGen™. The main design requirement of the laboratory setup was to subject alloy coupons of the types 253MA, 800H and 310 to a high pressure, high temperature environment with a gaseous atmosphere comparable to that of the WhisperGen™ working gas. In an AC WhisperGen™ MicroCHP system the working gas is

at a pressure of 24 bar, and temperatures of up to 900ºC. The working gas of the WhisperGen™, after several hundred hours, was previously determined to be approximately 3% carbon monoxide, 1% carbon dioxide, 3% hydrogen, 1% oxygen and 92% nitrogen.

It was not possible to simulate the WhisperGen™ heater head environment using a pressure vessel. In principle, the behaviour of a gaseous environment at 24 bar can be simulated through an experiment at 1 bar if the gas composition is adjusted so that the chemical potentials are the same. Consequently an alternative testing method was used, in which the effect of pressure was modelled using thermodynamic calculations. The calculations were carried out with the software Thermo-Calc™.

Chemical potential (μ) is a measure of the change in free energy of a system (dG_i) when a number of particles (dn_i) of species i are added to or removed from a system while the number of other particles, temperature and pressure are kept constant (see Equation 1) [1]. Put more simply, the chemical potential of a species i in a phase is a measure of the driving force for the species to leave the phase. If the chemical potential is different between two different phases then the species i will have a tendency to move from the phase in which it occurs at a higher chemical potential into the phase in which it occurs at a lower chemical potential. A difference in chemical potential is the driving force for chemical diffusion, and equilibrium is reached when the chemical potential is the same in all phases such that the species i is distributed throughout the phases [1].

$$\left(dG_i = \frac{\delta G}{\delta n_i} \cdot dn_i \right)_{T,p,i \neq j} \qquad \textbf{\textit{Equation 3.1}}$$

The software Thermo-Calc™ is commonly used for the calculation of multicomponent thermodynamics and phase diagrams. Thermo-Calc™ is highly versatile, and can be used in many different applications for thermodynamic calculations. The program was used in this work to find a gas composition at 1 bar with the same chemical potentials as the WhisperGen™ working gas at 24 bar. It was not possible to perform the calculations for the full working gas composition, so the carbon and nitrogen chemical potentials of the working gas mixture were modelled separately. This allowed the effect of each species to be studied in isolation. The Thermo-Calc™ results for the carbon and nitrogen chemical potentials of the working gas mixture at a pressure of 24 bar, and at temperatures of 900, 800 and 700ºC, are provided in Table 3.1.

Table 3.1: The carbon and nitrogen chemical potentials calculated for the working gas mixture at 24 bar and a range of temperatures

	Chemical Potential (Gas)	
Temperature (°C)	**Carbon**	**Nitrogen**
900	4.11E-03	1.53E-05
800	1.94E-02	1.72E-05
700	1.12E-01	1.96E-05

Thermo-Calc™ was then used to find the gas compositions required to model the chemical potentials shown in Table 3.1. It was found that to recreate the carbon potentials given in Table 3.1, gas mixtures combining carbon monoxide and carbon dioxide were required, and these are provided in Table 3.2 for each temperature. A catalyst was used to ensure that the correct chemical potential was reached during the tests, which is described in more depth in Section 3.3.1.1.

Table 3.2: The gas compositions required to model the carbon activity given in Table 3.1

Temperature (°C)	Carbon Monoxide (%)	Carbon Dioxide (%)
900	59.15	40.85
800	55.66	44.33
700	49.78	50.21

The gas compositions required to model the nitrogen chemical potentials in Table 3.1 are provided in Table 3.3. The required gas mixtures consist of a very small amount of ammonia with a balance of hydrogen. It is not possible to create mixtures of this accuracy, and the use of hydrogen around a furnace presents a safety issue. Therefore, the nitrogen-activity tests were instead undertaken using nitrogen gas.

Table 3.3: The gas compositions required to model the nitrogen activity given in Table 3.1

Temperature (°C)	Ammonia (%)	Hydrogen
900	0.001035	Balance
800	0.0017532	Balance
700	0.0033062	Balance

The set of tests undertaken during the laboratory section of the experimental work, including those run in nitrogen, is summarised in Table 3.4. Tests 1 to 6 were conducted in three different CO/CO_2 gas mixtures, one for each temperature, with the tests running for 300 hours and 600 hours at each temperature. The remaining tests (7-12) were conducted in nitrogen gas with the same approach as for the first set of tests. The gas utilized for the nitrogen tests (7-12) was industrial grade oxygen free nitrogen 152 ($\leq$ 10 ppm oxygen) from the company BOC Gases. The CO/CO_2 gas mixtures utilised for the carbon tests were also prepared by BOC, and were of the accuracy shown in Table 3.4.

Table 3.4: A summary of the tests undertaken for the laboratory section of the experimental work

Test No.	Temperature (℃)	Gas	Time (hours)
1	900	41±1% CO_2 in CO	300
2	900	41±1% CO_2 in CO	600
3	800	44.1±0.8% CO_2 in CO	300
4	800	44.1±0.8% CO_2 in CO	600
5	700	49.8±0.8% CO_2 in CO	300
6	700	49.8±0.8% CO_2 in CO	600
7	900	N_2	300
8	900	N_2	600
9	800	N_2	300
10	800	N_2	600
11	700	N_2	300
12	700	N_2	600

A number of simplifications were required in order to experimentally simulate the heater head environment without the use of a pressure vessel. The effects of the carbon and nitrogen chemical potentials were decoupled, taking away the combined effects of nitrogen and carbon, such as the formation of carbonitrides. The working gas in the engine also contains oxygen and hydrogen, the effects of which could not be included in this experimentation. Examination of the heater heads run in a real engine showed that oxygen plays an important part in the high temperature corrosion of the heater heads, but this will be discussed in depth in Chapter 6. An additional limitation was that the calculations undertaken using Thermo-Calc™ Software assume equilibrium in both the gas and the alloy, but in reality equilibrium conditions will not prevail in the alloy, and may or may not prevail in the gas. Another minor limitation was that it was assumed in the calculations that the tests would be conducted at a pressure of 1 bar absolute, an impossible feat in reality as a positive gauge pressure is required for flow to occur.

3.2.2 Testing of heater heads in a WhisperGen™

A test in a WhisperGen™ AC Mark 5 MicroCHP System was conducted to ascertain the effect of the working gas environment on heater heads fabricated from 253MA, 800H and 310, in a real engine, so that these results could be compared with those found during the laboratory simulations. Heater heads were fabricated out of each of the three alloys by WhisperGen Limited for this purpose, and were subsequently placed in a test engine which was run for 600 hours.

3.2.3 Laboratory Testing Setup

The laboratory test setup was designed to subject alloy coupons to a continuously flowing gaseous environment while they were held at high temperature, and is shown in both a schematic in Figure 1, and a photograph in Figure 2. A cradle made out of silica glass which held the alloy coupons was placed inside a tube also made of silica glass which was located in a tube furnace. This arrangement allowed the coupons to contact silica only at small areas. The gas mixture was controlled by a pressure regulator and a flow meter, and was flowed continuously through the glass tube. The temperature of the furnace was controlled by the furnace control unit and monitored via a thermocouple mounted near the coupons inside the glass tube.

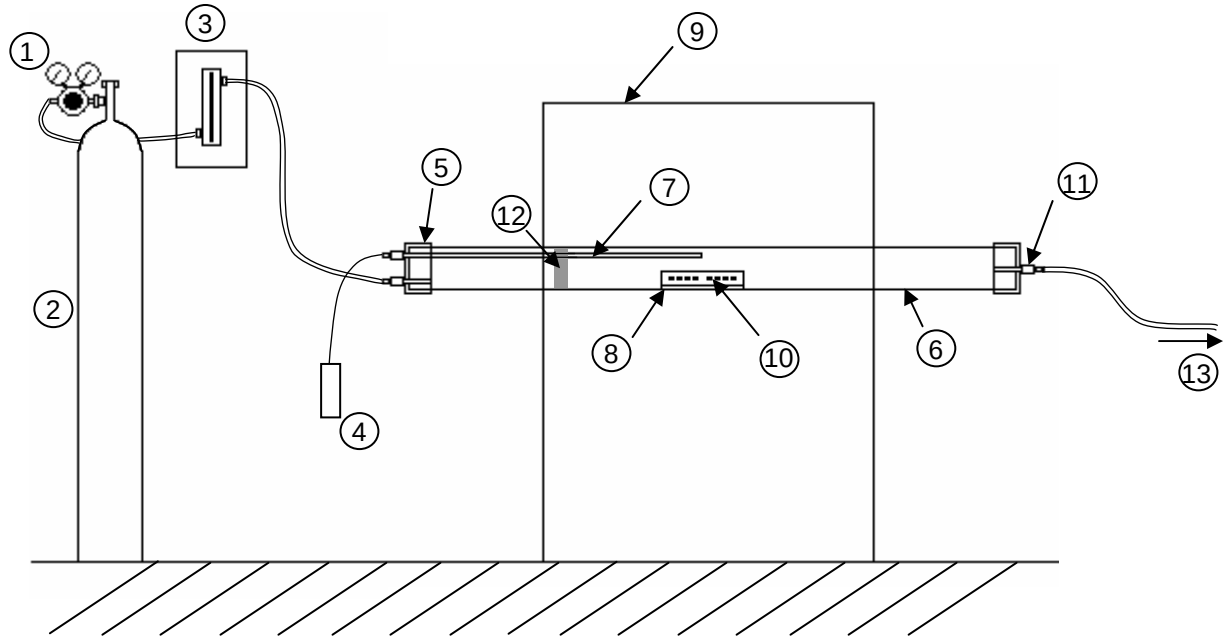

1. Gas Bottle Pressure Regulator
2. G-Size Gas Bottle
3. Flow meter
4. Thermocouple Reader
5. End Cap
6. Silica Glass Tube
7. Thermocouple Probe
8. Silica Glass Coupon Cradle
9. Tube Furnace
10. Alloy Coupons
11. Tube Fitting
12. Ceramic wool catalyst for carbon experiments only
13. Exhaust

Figure 3.1: Schematic of the laboratory setup for the experiments

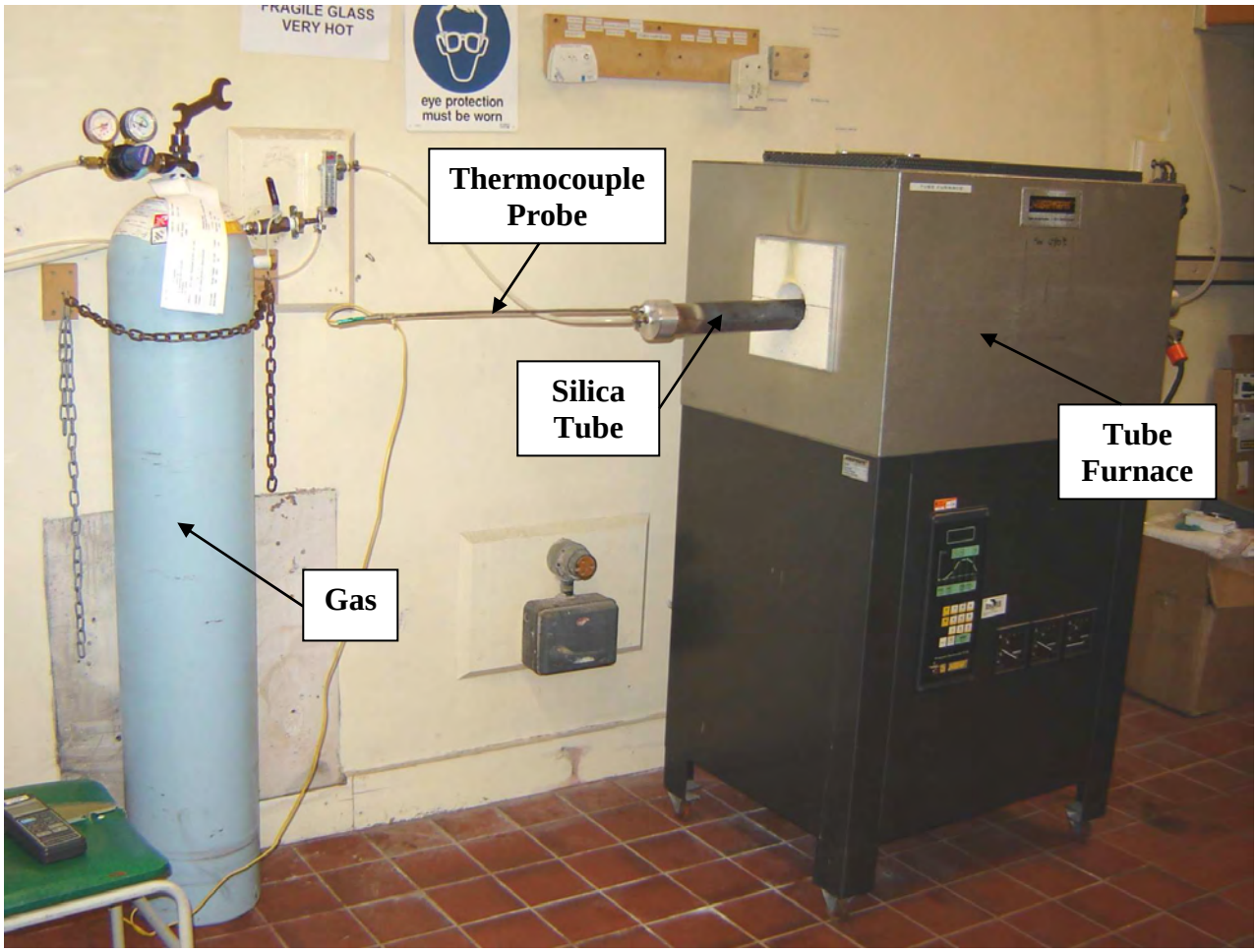

Figure 3.2: Photo of the laboratory setup for the experiments

The silica glass tube was sealed by two end caps, one on each end, which contained fittings to allow for thermocouple insertion on the inlet side, and allowed the inlet and outlet of gas to and from the tube. The glass tube was deliberately designed to overhang the furnace by 400mm on either side to ensure that the end caps would be cool enough for the seals and fittings in the end caps to withstand the temperature.

The two end caps were fabricated out of aluminium for weight considerations, and each had a double o-ring design to seal in the gas and ensure pressure integrity, as shown in the two CAD drawings in Appendix A. All threads were sealed using P.T.F.E. thread seal tape, and the end caps were sealed using Viton® O-Rings. The gas flowed through plastic tubing that could withstand

temperatures up to 200°C, with the tubing connections' integrity ensured by Jubilee® Clips. The accuracy of the thermocouple probe and reader was checked by Homersham Limited (3E Homersham Place, Burnside, Christchurch), and was found to be only one degree higher than their reference probe at both 700 and 800°C, and three degrees higher at 900°C, so this discrepancy was taken into account during use.

A temperature profile of the furnace with respect to distance from the centre was also generated as part of the furnace calibration, as shown in Figure 3.3. Once the furnace had reached a steady 900°C, temperature readings were taken at various distances from the centre of the furnace using the thermocouple probe. This information was used to determine the placement of coupons within the furnace so that all coupons were subjected to the same temperature within a one degree tolerance. It was ascertained that all the coupons for a given test would need to be placed within 75mm on either side of the furnace, so the width of each coupon had to be a maximum of 15mm in order to fit in the required number of samples.

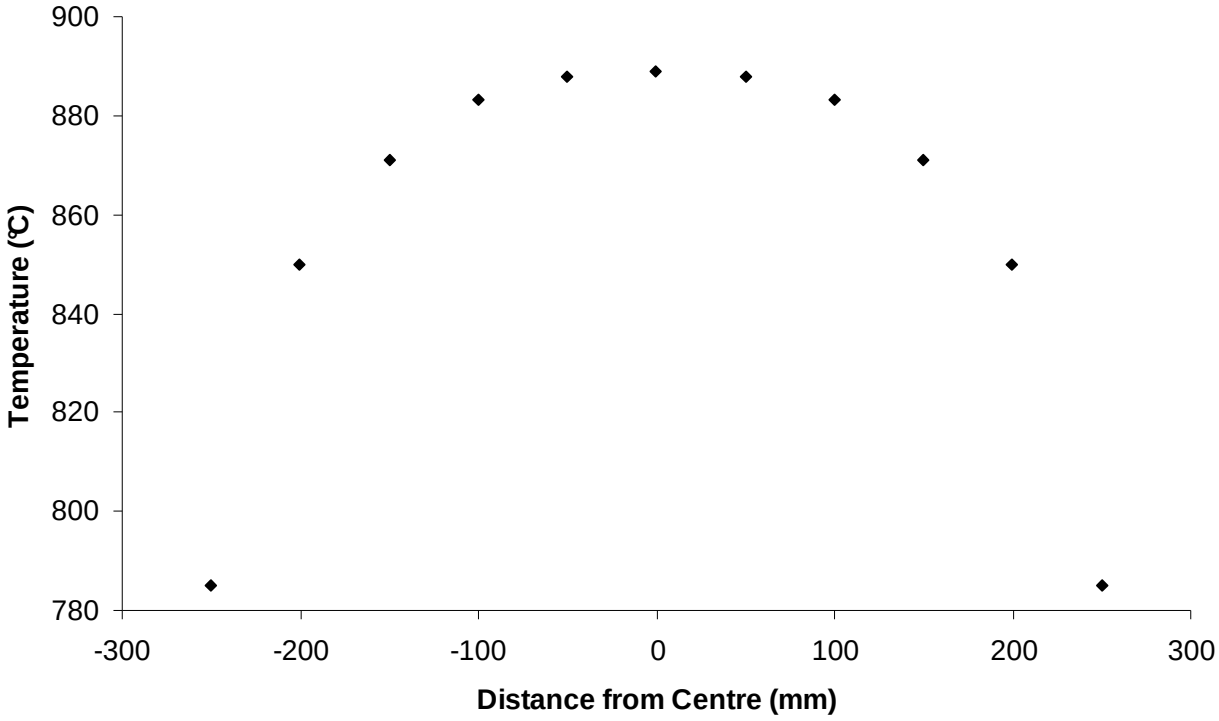

Figure 3.3: The temperature profile of the tube furnace with respect to distance from the centre when set to 900°C and stability is reached

An important factor in the experimental setup was the flow rate of the gas mixture, controlled by a flow meter and calculated such that the gas mixture would last for the full 600 hours. The flow meter used was a Dwyer Rate-Master Flow meter of the type RMA-150-SSV, with the ability to control flow between 0-100 cc/min (0-0.1 LPM air). The flow meter was calibrated using argon and adjusted using the molecular weight of the other gases used. The flow rate was selected to keep the flow laminar (see the calculation in Appendix B), and so that the gas cylinder would last the duration of the test (600 hours).

Some experimental error was present during the laboratory experimentation due to limitations in the accuracy of some instruments and consumables. The flow meter gave fluctuating flow rate readings between checks, with an inaccuracy approximated to be 50 ± 20 cc/min. This fluctuation in flow rate may have been caused by the fluctuation in pressure that the pressure regulator exhibited. The

accuracy of the flow meter was checked using argon gas for safety reasons, as was mentioned earlier in this section.

The uncertainties associated with the gas mixtures received from BOC for the CO/CO_2 tests are given in Table 3.4, in which they are compared with the values stipulated by Thermo-Calc™ for the CO_2 constituent of the mixtures. The nitrogen gas used for the nitrogen tests was industrial grade oxygen free nitrogen 152, certified to contain $\leq$ 10 ppm oxygen. The Sartorious balance used to weigh the samples before and after each test was assumed to be accurate to four decimal places, and was last calibrated in 2003 by Biolab Limited (105 Hayton Road, Wigram, Christchurch).

3.2.4 Safety

Health and safety were important considerations for the experimental setup. A risk management spreadsheet (see Appendix C) was written in order to ensure a safe working environment. This document detailed possible safety issues along with level of risk, and the steps taken to mitigate these issues. The main safety issue was the use of carbon monoxide gas due to flammability and toxicity. Hence a carbon monoxide detector (SF Detection Model SF350EN) was installed, the door to the laboratory was kept shut, and the gas mixture was exhausted out the window instead of solely relying on the fume fan. In addition, the gas bottle was chained to the wall, visible warning signage was placed on and near the laboratory setup, and relevant staff members were informed of the issues.

3.3 Experimental Methodology

3.3.1 Laboratory Experiments

A significant amount of preparation took place prior to each test run in the laboratory, and also after each test in order to prepare the samples for analysis using techniques such as energy dispersive spectroscopy (EDS). In this section, a description of the methodology used to prepare the coupons before testing, and the samples after testing, will be given, followed by the procedure used during the tests, and an explanation of how the chloroplatinic acid catalyst was prepared.

3.3.1.1 Preparation of catalyst for CO/CO_2 tests

A catalyst was prepared for the CO/CO_2 tests to ensure that equilibrium was reached in the gas mixtures, and that the correct chemical potential for the atmosphere was therefore reached. First, several drops of chloroplatinic acid (H_2PtC_{l6}) were added to a small beaker of ethanol, turning the ethanol slightly yellow. A portion of alumina-silica ceramic fibre blanket was then added to the beaker, and the fibre was lit so that the alcohol burnt off and the wool turned grey. This process was repeated several times with the same piece of fibre. The fibre was then placed inside the silica glass tube through which the CO/CO_2 mixture passed, so that it filled the cross section of the tube loosely.

3.3.1.2 Coupon preparation before placement in the furnace

The wrought alloy bars were cut in several 5mm slices in a lathe using a parting tool. Each slice was then marked with a scribe in 14 x 23 mm rectangles, and roughly cut with a band saw. The resulting samples were subsequently milled, and then ground with 180 grit, on every surface.

The dimensions of each coupon were measured using a micrometer, after which each coupon was cleaned thoroughly with a brush in pegasol solvent. A Sartorius balance with a four decimal place display was used to weigh each coupon. The appropriate coupons were handled with gloves and placed into the silica glass cradle. The cradle was then placed in the silica tube and pushed in the correct distance in order for the coupons to be in the centre of the furnace.

3.3.1.3 Sample preparation after testing in the furnace

After each test the coupons were removed from the silica cradle with gloves, and the coupons were ultrasonically cleaned in ethanol before each was reweighed using the Sartorious balance. A section at least 2mm thick was then cut from each coupon using a Buehler® low speed saw, after which each section was coated in electroless nickel plate in order to ensure retention of the scale during subsequent processing procedures.

Experience showed that alloy 800H required a layer of gold sputter prior to nickel plating. After cleaning ultrasonically in petroleum spirit, the sample was placed into the Polaron E5100 Series II Cool Sputter for two minutes on each edge. The samples were electroless nickel plated using a Buehler® Edgemet® Kit. All alloy sections were ultrasonically cleaned first in petroleum spirit and then in the cleaning fluid provided in the kit, before being placed in the kit formula for at least four hours. The kit formula was prepared by mixing two supplied liquids together in a beaker in equal amounts and then heating the mixture to 85°C with a hot plate. A temperature controller attached to a thermocouple placed in the fluid was used to ensure that the temperature of the fluid stayed constant during plating.

When the nickel plating was complete, each section was taken out of the beaker and rinsed thoroughly in water and ethanol, and then dried. The sections were then each placed, using a

standard procedure, into Buehler® Probemet™ conductive moulding compound. Each moulded sample was then polished through the following sequence: 240, 400 then 600 grit, followed by 9μm and then 3μm diamond paste, and finally 0.04 μm Buehler® Mastermet® colloidal silica polishing suspension.

Once polished, each sample was examined using the Leica optical microscope in order to find a suitable representative area for examination during the subsequent analysis with energy dispersive spectroscopy, electron back scatter diffraction and optical microscopy. The examination area was marked with three hardness indents using the Vickers micro hardness indenter, after which the given sample was ready for analysis.

3.3.1.4 Procedures for furnace and daily checks during a test

The gas was flowed continuously both when starting the furnace and waiting for it to get to temperature, and when stopping the furnace and waiting for it to cool. This was to purge any oxygen present in the silica tube prior to heating, and to stop any oxygen entering the tube while the furnace was still hot. The exact procedure to start or continue a test was to turn on the gas regulator tap, start the furnace and wait for three hours or until the furnace reached the appropriate temperature, then check the flow rate and temperature, and correct if necessary. During a given test a leak check using detergent was conducted daily, along with a check of the flow rate, gas regulator pressure, gas bottle pressure and furnace temperature. At the end of either a 300 or 600 hour test, the furnace was switched off, and the gas was left flowing until the furnace cooled to below 100°C, which took approximately 12 hours.

3.3.2 Heater Head Test

A 20 x 20mm square was cut out of the centre of the top of each of the three heater heads from the WhisperGen^{TM} microCHP system test, and then a section at least 2mm thick was cut out of each square using the low speed saw. Each section was then prepared for analysis with exactly the same method as described for the laboratory samples in Section 3.3.1.

References

[1] D. R. Gaskell, *Introduction to metallurgical thermodynamics*, Scripta [Distributed by] McGraw-Hill, Washington, D.C. **1973**

4 Experimental Techniques for Microstructural Characterisation

4.1 Introduction

Several advanced techniques were used to characterise the microstructure of each sample in order to deduce the extent and form of high- temperature corrosion that had occurred. A representative area containing both the alloy substrate and the scale of each sample was examined. An example of each technique is given in this section by displaying the results for an AISI 310 heater head. Each sample was studied using a scanning electron microscope (SEM), with which secondary electron images (SEI) of the microstructure were created, and the energy dispersive spectroscopy (EDS) attachment was used for elemental mapping. Electron back-scatter diffraction (EBSD) was used in conjunction with EDS to identify phases present in the microstructure. Finally, optical microscopy was undertaken to show the size and shape of the grains present in each representative area.

4.2 EDS

Secondary electron images were obtained for a characteristic area of each sample using a JEOL JSM 7000F High Resolution Field Emission Gun Scanning Electron Microscope (FEG SEM), with an accelerating voltage of 20kV. An elemental map was then generated on each SEI area with a JEOL EX-2300-BU EDS system, which uses JEOL Analysis Station software as an interface between the SEM and EDS detector. An example of an image generated using the Analysis Station

software is given in Figure 4.1, which shows an elemental map of a characteristic cross-section of an AISI 310 heater head run in a WhisperGen™ for 600 hours, with the images for oxygen, chromium and silicon overlapped. A region of the suspected sigma phase present in the alloy was selected using Analysis Station, and an EDS spectrum of the region was generated using the pop-up function, and is shown in Figure 4.2. The spectrum in Figure 4.2 confirmed that the phase was rich in chromium and iron, and could therefore be sigma phase. However, in order to confirm the identification of the phase a technique known as EBSD, which can confirm crystal structure, was required.

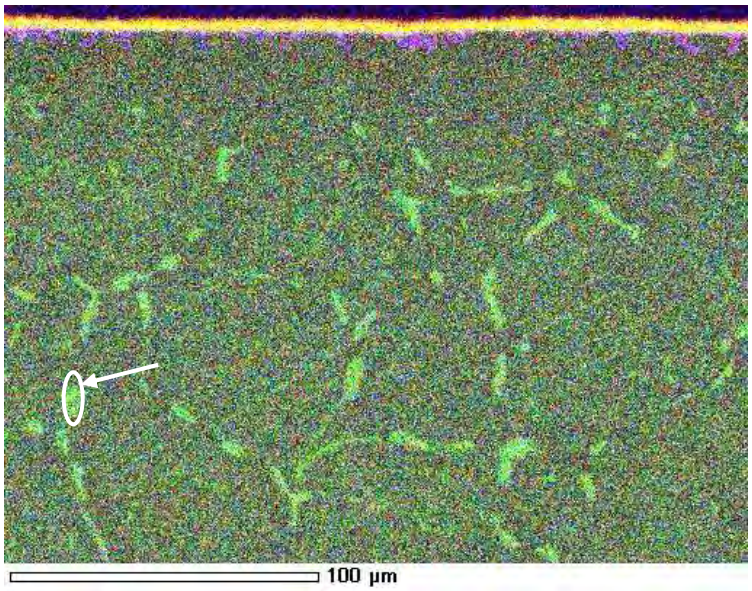

Figure 4.1: A characteristic cross-section at 500x from an AISI 310 heater head run in a WhisperGen™ for 600 hours. The map is an overlap of the elements oxygen, chromium and silicon, and a region of sigma phase is circled.

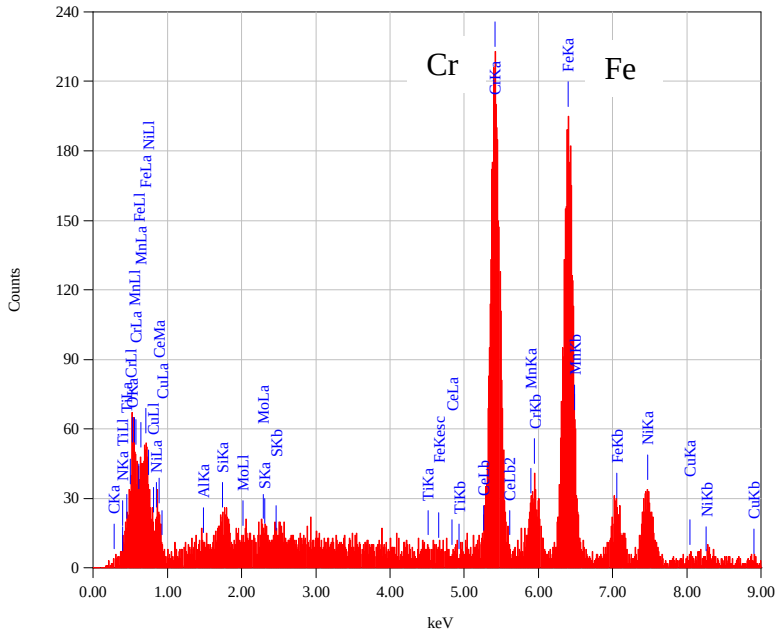

Figure 4.2: An EDS pop-up spectrum generated from a region of sigma phase shown in Figure 4.1. The spectrum shows that the phase is rich in chromium and iron, as expected for sigma phase

4.3 EBSD

EBSD is a technique that can be used to identify crystal structures. In this work, it was used in conjunction with EDS to identify the phases present in the alloys' microstructures. The apparatus consists of a JEOL JSM 6100 Scanning Electron Microscope with a HKL Technology EBSD detector, and an HKL Flamenco data acquisition program (Version 5.0.9.0). The Flamenco camera was set to high gain and no binning, and noise reduction was set to 10 frames. An example of phase identification using EBSD is given in Figures 4.3 and 4.4, showing the identification of sigma phase in an AISI 310 heater head. The electron beam was placed within a region of phase believed to be sigma phase, which is shown in the image obtained by Flamenco at 3000x magnification in Figure 4.3. The EBSD diffraction pattern acquired by Flamenco for this point is shown before and after the 'positive' identification of sigma phase in Figure 4.4. In order to obtain this positive

identification, a number of steps were followed in the EBSD process. First, the crystallographic data for possible phases was entered into the HKL Channel 5 software database. The EBSD pattern was obtained from the phase, and the HKL software automatically suggested solutions ranked by lowest 'mean angular deviation' (MAD). A MAD of less than 1 indicated a desirable solution for the phase.

Figure 4.3: A SE image of the AISI 310 heater head, with the arrow on a region of sigma phase.

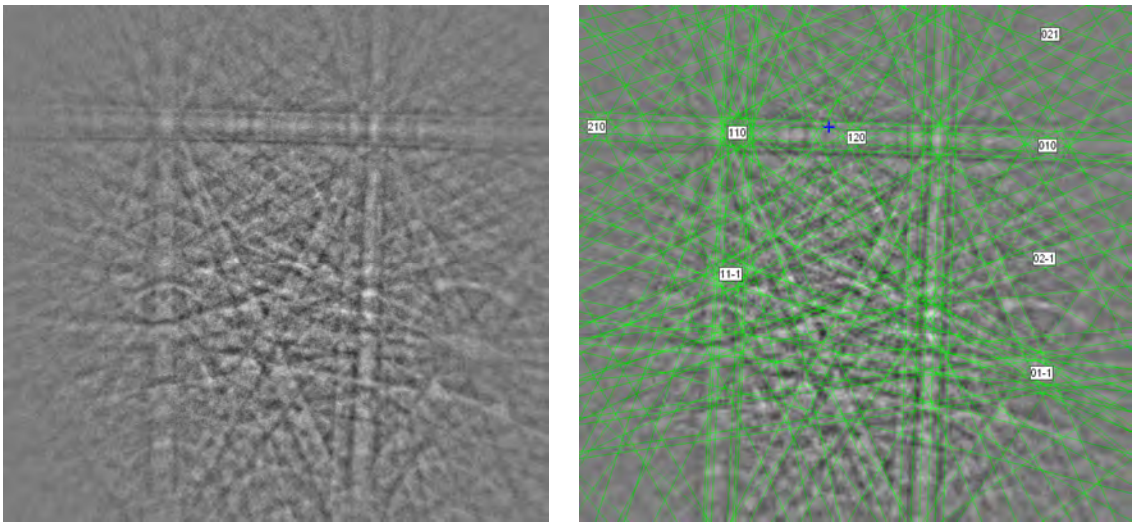

Figure 4.4: The EBSD diffraction pattern obtained for the point displayed in Figure 4.3, before (left) and after (right) identification using Flamenco. The identification confirmed that the phase in Figure 4.3 is sigma.

4.4 Optical Microscopy

The aim of the optical microscopy undertaken was to display the grain and interphase boundaries present in the representative area of each sample. A Leica DM IRM optical microscope with a Zeiss AxioCam HR camera was used to obtain the bright-field images. The alloys were etched using glyceregia, a mixture of glycerol (33%), hydrochloric acid (50%) and nitric acid (17%) used for austenitic steels to show austenite grain boundaries, attack sigma phase and outline carbides. An example of an optical micrograph is given in Figure 4.5, and shows a representative area of an AISI 310 heater head. This figure shows the sigma phase is distributed on austenite grain and twin boundaries.

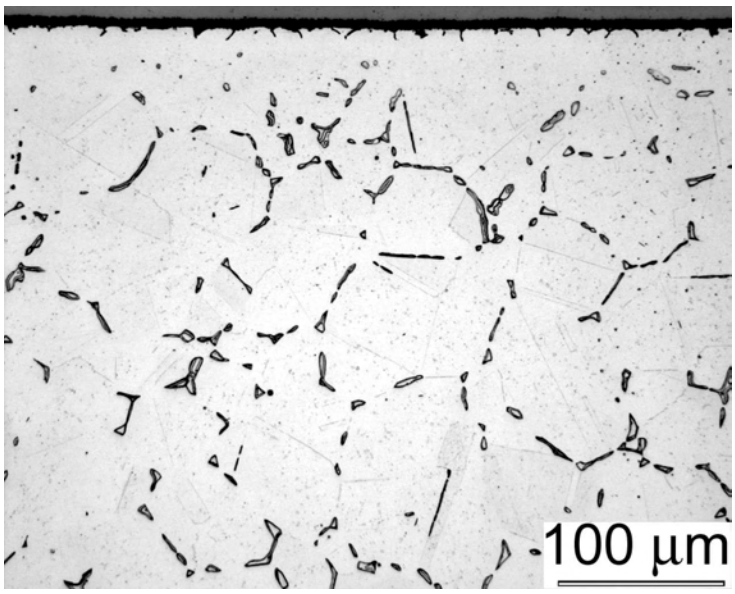

Figure 4.5: An optical micrograph (etched using glyceregia) of a representative area of an AISI 310 heater head run in a WhisperGen™ for 600 hours.

5 Experimental Results and Discussion

Alloying additions affect the performance of an alloy collectively, and as such it is difficult to predict the performance of an alloy under unusual conditions without conducting experiments. The environment that Sandvik 253MA heater heads are subjected to within the WhisperGen™ engine is unique, in that the working gas of the engine is of unusual composition, and is at high pressure and high temperature. The literature review (Chapter 2) found that high-temperature corrosion tests of alloys in nitrogen-based atmospheres are rare. Specifically, no tests undertaken in a nitrogen-based atmosphere with carbonaceous impurities were found. In addition, no studies were found that investigate the effect of high-pressure atmospheres on alloys 253MA, 310 and 800H, or any other austenitic alloys. This lack of relevant literature made the current study necessary to compare the performance of alloys 253MA, 800H and 310 in a high-pressure, high-temperature nitrogen-based atmosphere with carbonaceous (e.g. CO, CO_2, etc) impurities.

Three heater head materials were compared by conducting experiments in a laboratory setting that simulated the conditions in a WhisperGen™. Testing was also undertaken in an actual WhisperGen™ so that the results could be compared to those from the laboratory experiments (see Chapter 3 for details). This chapter provides a summary of results obtained from the aforementioned experimentation, and a discussion of these results. Section 5.1 compares the spalling performance of the three alloys. A weight-change method and observation using electron microscopy were used to assess the laboratory and heater head test results. Section 5.2 provides a comparison between the microstructural developments for each of the alloys under different conditions, and describes the implications of these observations on the performance of the alloys.

Finally, section 5.3 provides an overview of the findings for the three alloys, and presents the factors that need to be considered during selection of an alloy for the heater head application.

5.1 Comparison in Spalling Performance

The assessment of spalling characteristics under different conditions was an important part of determining the performance of the three prospective heater head alloys. Two methods were used to evaluate the extent of spalling: the change in weight measurements gave a quantitative indication (for the laboratory experiments only), while observation at high magnification provided further insight.

The results for the weight-change method are shown in Figures 5.1 and 5.2. These figures show that 253MA usually (8 out of 10 samples) experienced net weight loss regardless of temperature and atmosphere. The net weight loss is due to the weight loss of spalling exceeding the gain of weight of the oxide layer growth during oxidation. The four remaining 253MA samples experienced a net weight gain, which suggests that if spalling did occur, then the weight loss due to spalling was exceeded by the weight gain during regrowth of the oxide layer.

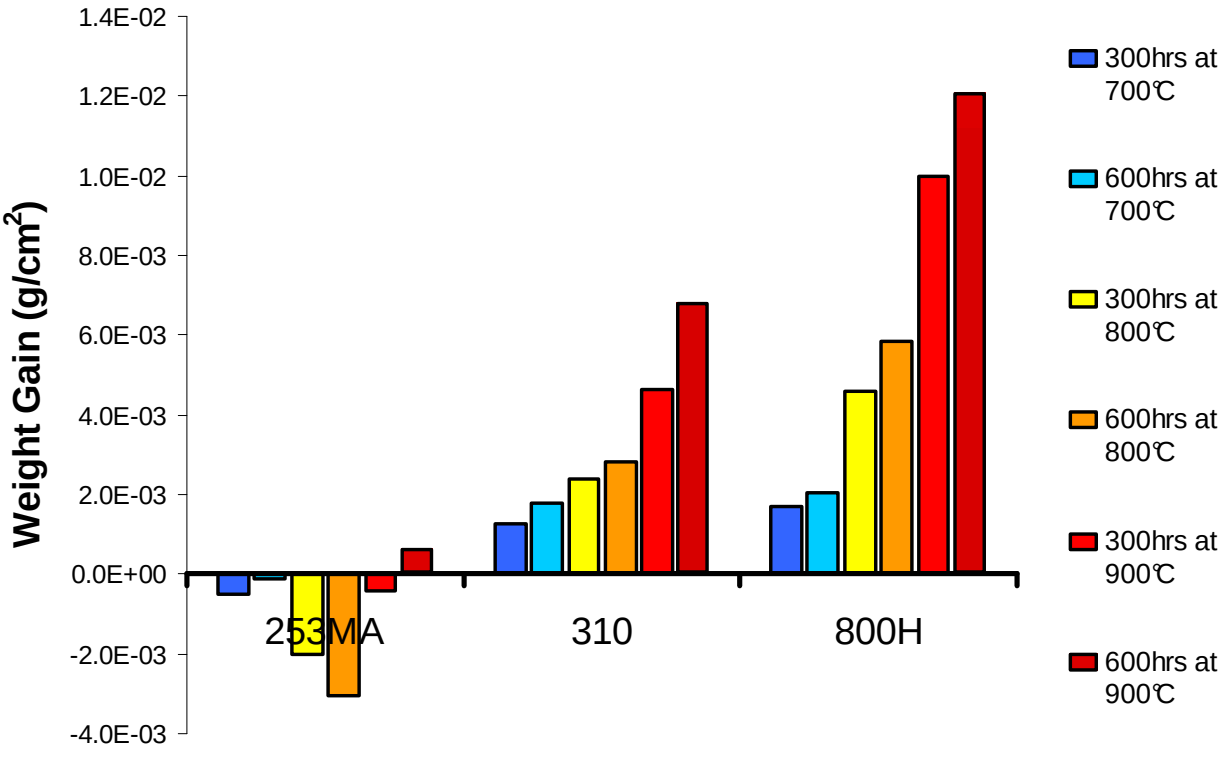

Figure 5.1: Change in weight measurements before and after testing for 253MA, 310 and 800H for the laboratory tests undertaken at 700, 800 and 900°C in CO/CO_2 gas mixtures.

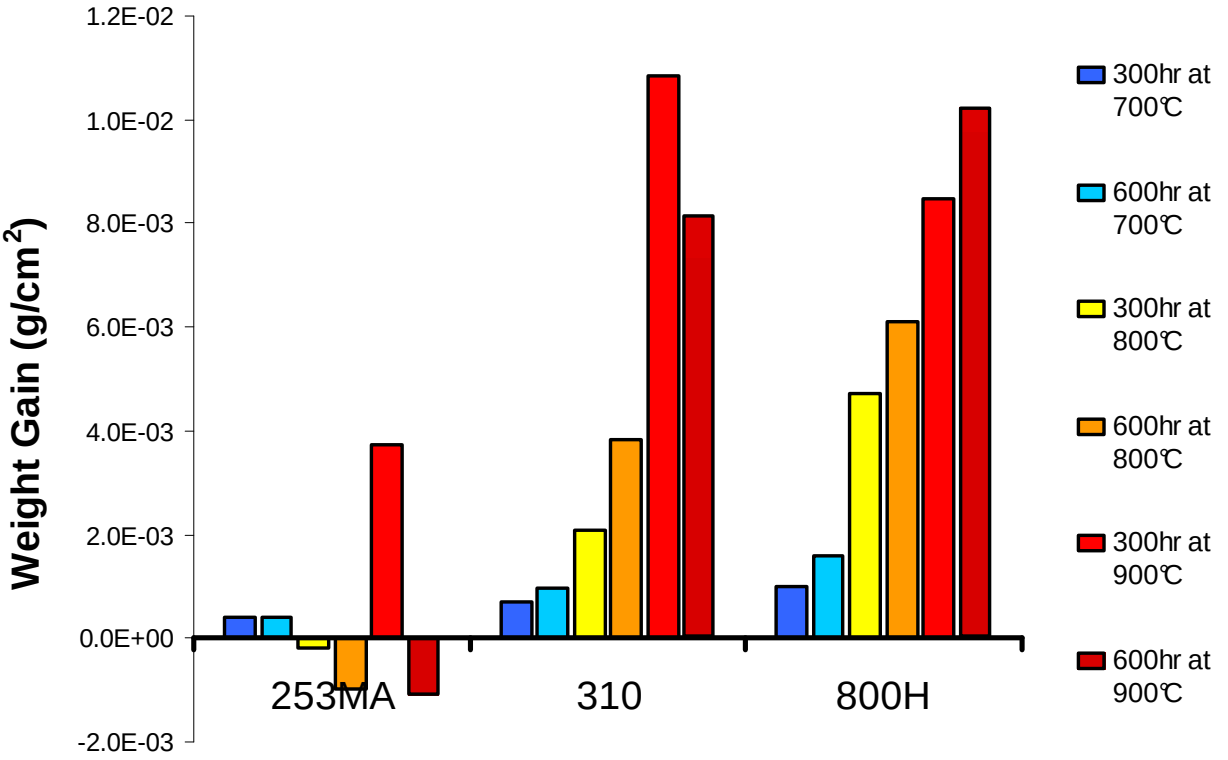

Figure 5.2: Change in weight measurements before and after testing for 253MA, 310 and 800H for the laboratory tests undertaken at 700, 800 and 900°C in nitrogen.

Weight measurements for the other two alloys, 310 and 800H, show that net weight loss did not occur on any occasion. The weight gains shown in Figures 5.1 and 5.2 follow trends as expected for Equations 2.7 and 2.8 in Chapter 2, which describe the parabolic rate law, and the Arrhenius rate law, respectively. At each temperature there is a gain in weight between 300 and 600 hours (with the exception of 310 at 900°C in nitrogen), as expected in Equation 2.7. For a given temperature the parabolic rate constant (k_p) stays the same. However, an increase in temperature leads to an exponential increase in the parabolic oxidation rate, as described in Equation 2.7, which leads to a corresponding increase in the oxide-layer thickness. The results in Figures 5.1 and 5.2 for alloys 310 and 800H display the increase in oxide-layer thickness with increasing temperature clearly. Figure 5.3 is a schematic depicting the aforementioned relationship between temperature, k_p and time.

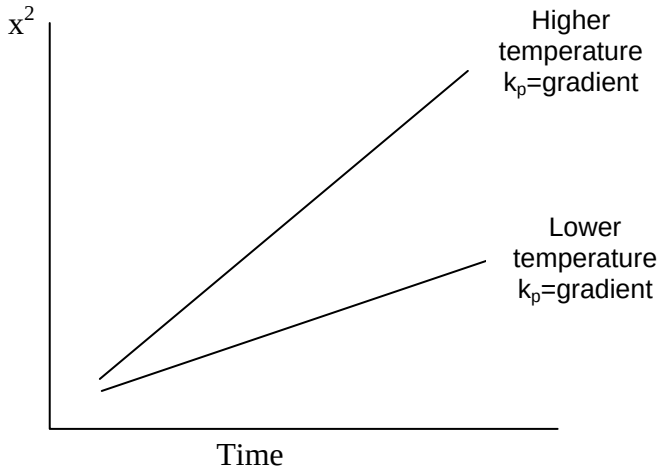

Figure 5.3: The relationship between oxide layer thickness (x), time and parabolic rate constant k_p

Although the weight-change method was useful as an indication of spalling, there are some limitations with the results, and as such, they should be interpreted in conjunction with other information. The use of one sample per test prevented the ability to investigate whether there was statistical variance or anomalies. Another limitation of this technique is the discontinuous nature of assessment. A disadvantage of discontinuous sampling is that the progress of the reaction between

the sampling points is not known, so possible features can be missed, such as when the scale spalls. However, the advantages of a discontinuous technique include the simplicity of apparatus, and the ability to obtain metallographic information from each data point.

The other method used to evaluate the extent of spalling was to observe a section of each sample with optical and scanning electron microscopy. The results of these observations are given in Tables 5.1, 5.2, and 5.3 for the heater heads, the laboratory tests in CO/CO_2, and the laboratory tests in nitrogen, respectively. Tables 5.1-5.3 give an indication of the amount of spalling observed, and include the thickness of each oxide layer. It is apparent from these results that 253MA undergoes significant spalling in every laboratory test, but appears not to spall for the heater head test. However, it is impossible to say whether or not spalling occurred for this 253MA heater head from this observation alone, as the oxide layer could have healed after spalling on this occasion.

Table 5.1: Summary of spalling results for heater head tests in a WhisperGen™ for 600 hours

Sample	Extent Of Spalling	Scale Thickness
253MA Heater Head	No spalling	3-6μm
310 Heater Head	No spalling	3-4μm
800H Heater Head	No spalling	2.5-3.5μm

Table 5.2: Summary of spalling results for laboratory testing undertaken in CO/CO_2 gas mixtures

Sample	Extent Of Spalling	Scale Thickness
900°C in CO/CO_2		
253MA (300 hours)	Some spalling	1.5-5µm
253MA (600 hours)	Some spalling	3-6µm
310 (300 hours)	No spalling	1.4-2.8µm
310 (600 hours)	No spalling	3-4µm
800H (300 hours)	No spalling	4.5-9µm
800H (600 hours)	No spalling	4-8µm
800°C in CO/CO_2		
253MA (300 hours)	Extensive spalling	*
253MA (600 hours)	Extensive spalling	*
310 (300 hours)	No spalling	1.5-3µm
310 (600 hours)	Some spalling	2.5-3.5µm
800H (300 hours)	No spalling	2-3µm
800H (600 hours)	No spalling	2-4µm
700°C in CO/CO_2		
253MA (300 hours)	Extensive spalling	*
253MA (600 hours)	Extensive spalling	*
310 (300 hours)	No spalling	2-2.5µm
310 (600 hours)	Small amount of spalling	0.8-1.3µm
800H (300 hours)	No spalling	1-2.5µm
800H (600 hours)	No spalling	1-2µm

* Difficulty measuring thickness due to extent of spalling

Table 5.3: Summary of spalling results for laboratory testing undertaken in nitrogen

Sample	Extent Of Spalling	Scale Thickness
900°C in nitrogen		
253MA (300 hours)		
Case 1	Some spalling	1-1.5μm
Case 2	Extensive spalling	*
253MA (600 hours)	Some spalling	2.8-3.6μm
310 (300 hours)	No spalling	2-4μm
310 (600 hours)	No spalling	3-6μm
800H (300 hours)	No spalling	7-10μm
800H (600 hours)	No spalling	3-10μm
800°C in nitrogen		
253MA (300 hours)	Some spalling	1-3μm
253MA (600 hours)	Extensive spalling	*
310 (300 hours)	No spalling	2-2.5μm
310 (600 hours)	Some spalling	2-4μm
800H (300 hours)	No spalling	2-5μm
800H (600 hours)	No spalling	3-4μm
700°C in nitrogen		
253MA (300 hours)	Possible spalling	No scale
253MA (600 hours)	Possible spalling	No scale
310 (300 hours)	No spalling	0.5μm
310 (600 hours)	No spalling	0.6-0.8μm
800H (300 hours)	No spalling	<1μm
800H (600 hours)	No spalling	1-2.5μm

* Difficulty measuring thickness due to extent of spalling

The spalling observations for the two other alloys, 310 and 800H, are in stark contrast to those for 253MA. The 310 and 800H heater heads did not exhibit spalling, but as mentioned for the 253MA heater head, this observation was inconclusive. It was the laboratory test results for the two alloys that gave an interesting comparison to 253MA. Alloy 310 was observed to spall on three out of a total twelve occasions, at both 800 and 900°C in CO/CO_2 after 600 hours, and at 800°C in nitrogen after 600 hours. The observations show that alloy 800H did not exhibit spalling on any occasion during the laboratory testing.

A consideration of both the weight-change measurements and microscopic observations leads to a clear comparison between the spalling performances of the three alloys. Both the weight loss

measurements and microscopic observations showed that 253MA spalled when subjected to both atmospheres at all three temperatures. Although the weight-change measurements did not exhibit a net weight-loss for alloy 310, the microscopic observations showed that the 310 coupons did exhibit limited spalling. This indicates that even though there was not a measurable net weight-loss for the 310 coupons, it was likely that oxide layer rehealing masked any spalling that did occur. Both sets of results considered together indicate that spalling did not occur in alloy 800H at any time. Hence the laboratory tests suggest that alloy 800H would be the best choice of alloy to avoid spalling, followed by alloy 310, and 253MA is clearly the most inferior alloy in terms of resistance to spalling.

It should be noted at this point that the laboratory tests undertaken to assess spalling performances of the three alloys were conducted at a low oxygen partial pressure. The gas mixtures used for the laboratory tests were reported by BOC to contain oxygen impurities of less than 10 parts per million, which corresponds to an oxygen partial pressure of less than $1x10^{-5}$ atm. This oxygen partial pressure is magnitudes greater than the theoretical value that must be exceeded to form a thermodynamically stable Cr_2O_3 layer as calculated using an Ellingham diagram (pO_2 of $1x10^{-24}$ atm at 900°C). However, the oxygen partial pressure for the working gas of a WhisperGen™ with the composition reported in this thesis (1% oxygen), is 0.24 atm at 24 bar. Hence the oxygen partial pressure for the working gas in WhisperGen™ is orders of magnitude greater than that at which the laboratory testing was conducted. The effect of oxygen partial pressure on the parabolic oxidation rate is given by Equation 2.9 in Chapter 2 of this thesis. As explained in Chapter 2, the parabolic rate constant for Cr_2O_3 increases with increasing oxygen partial pressure. Thus, the heater head test results may be misleading for a comparison of spalling characteristics.

This increased oxidation rate for the WhisperGen™ working gas compared to that for the laboratory tests is likely to have had a profound effect on the spalling characteristics of the alloys. It is possible that if the laboratory tests had been conducted at a higher oxygen partial pressure then the extent of spalling observed on 253MA would have been far less. However, this would not mean that spalling did not take place, as regeneration of the oxide layer is faster at a higher oxidation rate, and the thickness of the oxide layer would be greater at any given time. As mentioned in Chapter 2, spallation becomes more likely as an oxide layer gains thickness, since a smaller temperature drop is required to induce spallation. This suggests that spalling would still take place for 253MA at higher oxygen partial pressures such as those in a WhisperGen™, but the oxide layer would heal until the concentration of chromium at the scale-alloy interface went below a critical concentration, at which time the useful life of the alloy would be over. Therefore, it is possible that a higher partial pressure of oxygen would have masked the spalling occurring in the 253MA heater head samples.

Up to this point it has been shown that spalling occurred in the 253MA samples tested. Spalling is a mechanism which allows the accommodation of the growth and thermal stresses generated in an oxide layer during oxidation. The oxide layers on most engineering alloys are in compression, as growth stresses tend to be compressive, and thermal stresses are compressive during cooling (for Cr_2O_3). As stated in Chapter 2 of this thesis, spallation of an oxide layer does not usually occur under tensile stress, but frequently occurs when under compressive in-plane stress, by either a 'wedging' or 'buckling' process. It is explained in Chapter 2 that the wedging route to spallation occurs when there is a strong interface between the oxide and alloy but a weak oxide, whereas buckling occurs when there is a weak interface but a strong oxide. Buckling has been found to be unlikely for oxide thicknesses greater than 0.5μm. It is difficult to judge which route(s) to spallation occurred for the 253MA samples since the oxide layers were too discontinuous to judge

thickness, and buckling can therefore not be ruled out. However, in some cases the spalling that occurred did resemble the appearance of a buckling mechanism.

The spalling performance of the three alloys was compared by subjecting them to identical environments. Since the two routes to spallation depend on either a weak oxide or weak interface, it follows that an alloy that can produce a sufficiently strong oxide and strong interface should be more resistant to spalling, given the same scale thickness and stresses. As stated in Chapter 2, the cyclic oxidation performance of an alloy depends mainly on scale adherence. Scale adherence is dictated by scale morphology, as well as alloy and scale compositions. Therefore, the composition of the alloys 253MA, 310 and 800H has an influence on their spalling characteristics. The high nickel content of 800H ensures good adherence of the oxide layer, in addition to dramatically reinforcing the effect of chromium in providing oxidation resistance (see Chapter 2). The nickel content of 800H is almost three times that of 253MA, which could be one reason for the superior spalling performance of 800H in comparison to 253MA. The nickel content for alloy 310 lies in between those for the other two alloys, and is possibly the reason for the intermediate spalling performance of alloy 310.

Other interesting alloying additions from a spalling perspective are cerium, a rare earth element added to 253MA only, and silicon. The addition of a small amount of cerium promotes spalling resistance by improving scale adhesion, as stated in Chapter 2. However, despite this cerium addition, alloy 253MA spalled more than the other two alloys. The poor performance of 253MA may have been exacerbated by the addition of a large amount of silicon (~1.5%) to the alloy. Although additions of greater than 0.6% silicon lead to improved isothermal oxidation resistance through the formation of an inner silica layer, it has been shown *[1]* that this layer greatly worsens the extent of spallation during cyclic oxidation. Furthermore, the low silicon content of alloy 800H

(~0.2%) may have contributed to the superior spalling performance of this alloy, while the intermediate silicon content of alloy 310 (~0.6%) may be the reason for its intermediate spalling performance.

Spalling is an undesirable characteristic for heater heads in a WhisperGen^{TM} due to the abrasive nature of particles that eventually break down the piston seals. Although this effect on engine performance is the main reason that spalling should be avoided in heater heads, there are other detrimental ramifications of spalling, such as an increase in the kinetics of oxidation. As stated in Chapter 2 of this thesis, if a protective oxide forms on an alloy, and it is ideally dense, continuous and adherent, then a parabolic rate law governs the growth of the oxide layer. In this case, the rate of oxidation is limited by solid-state diffusional transport through the scale. However, if a protective scale spalls off or cracks then a parabolic rate law can shift suddenly or gradually into a linear rate law.

5.2 Microstructural development and implications

5.2.1 Explanation for Layout of Microstructural Results

The microstructure of every laboratory and heater head sample was analysed using optical microscopy and X-ray mapping. A complete atlas of these microstructures is provided on the CD attached to this thesis. One example from the atlas of microstructures is provided in Appendix D. As this example shows, the optical microscopy images, X-ray maps and EBSD phase identification results are provided for each sample that was analysed for this work. The example first provides images obtained at three different magnifications using optical microscopy (Figure D1). X-ray maps are provided at two different magnifications, with elemental X-ray maps and a composite X-

ray map for each magnification (Figures D2-D5). The elements presented in the X-ray maps in Figure D2 (for example) were deemed relevant for alloy 253MA, and are consistently presented in this order for 253MA. For alloy 310, the X-ray map for cerium (Ce) in the bottom right corner of the images (for 253MA) is replaced with the X-ray map for nickel. For alloy 800H, the X-ray map for nitrogen (N) is replaced with the X-ray map for titanium (Ti), and the X-ray map for cerium (Ce) is replaced with the X-ray map for aluminium (Al). The composite X-ray maps (see Figure D3 for an example) provide images of three overlapped X-ray maps. Again, the composite maps differ depending on the alloy, with 253MA and 310 composites made up of oxygen (red), chromium (green) and silicon (blue). 800H composite X-ray maps consist of aluminium (red), chromium (green) and titanium (blue).

The composite maps include the phases identified using EBSD. Specific examples of the identification of each phase found using EBSD are presented in Appendix E. In some cases, phases are referred to in brackets, as for example (Si,O). This infers that the crystal structure could not be determined due to difficulty obtaining an EBSD pattern. Difficulty obtaining patterns can be caused by several different factors: the quality of polish, the phase being amorphous, or the electron beam size being larger than the phase itself and therefore obtaining more than one pattern.

A written summary of the microstructures observed for every sample analysed is provided in Appendix E. Table E1 provides a summary of the microstructures observed in the heater heads run in a WhisperGen^{TM}, while Tables E2-E7 provide a summary of the microstructures observed in the samples that underwent laboratory testing. Tables E2, E3 and E4 contain a summary of microstructures for the laboratory tests undertaken in CO/CO_2 gas mixtures, at temperatures of 900, 800 and 700°C, respectively; tables E5, E6 and E7 contain a summary for the laboratory tests undertaken in nitrogen, at temperatures of 900, 800 and 700°C, respectively.

5.2.2 Discussion of Heater head Results

A direct comparison between the X-ray maps and optical micrographs for the three heater heads run in a WhisperGen^{TM} is provided in Figures 5.4 and 5.5. The results show that the 253MA heater head underwent extensive internal oxidation in the form of oxygen- and silicon- rich (Si,O) precipitates on austenite grain boundaries beneath the scale to a depth of approximately 35μm. It was not possible to obtain a pattern using EBSD for this phase, which could be explained by the presence of vitreous silica (SiO_2).

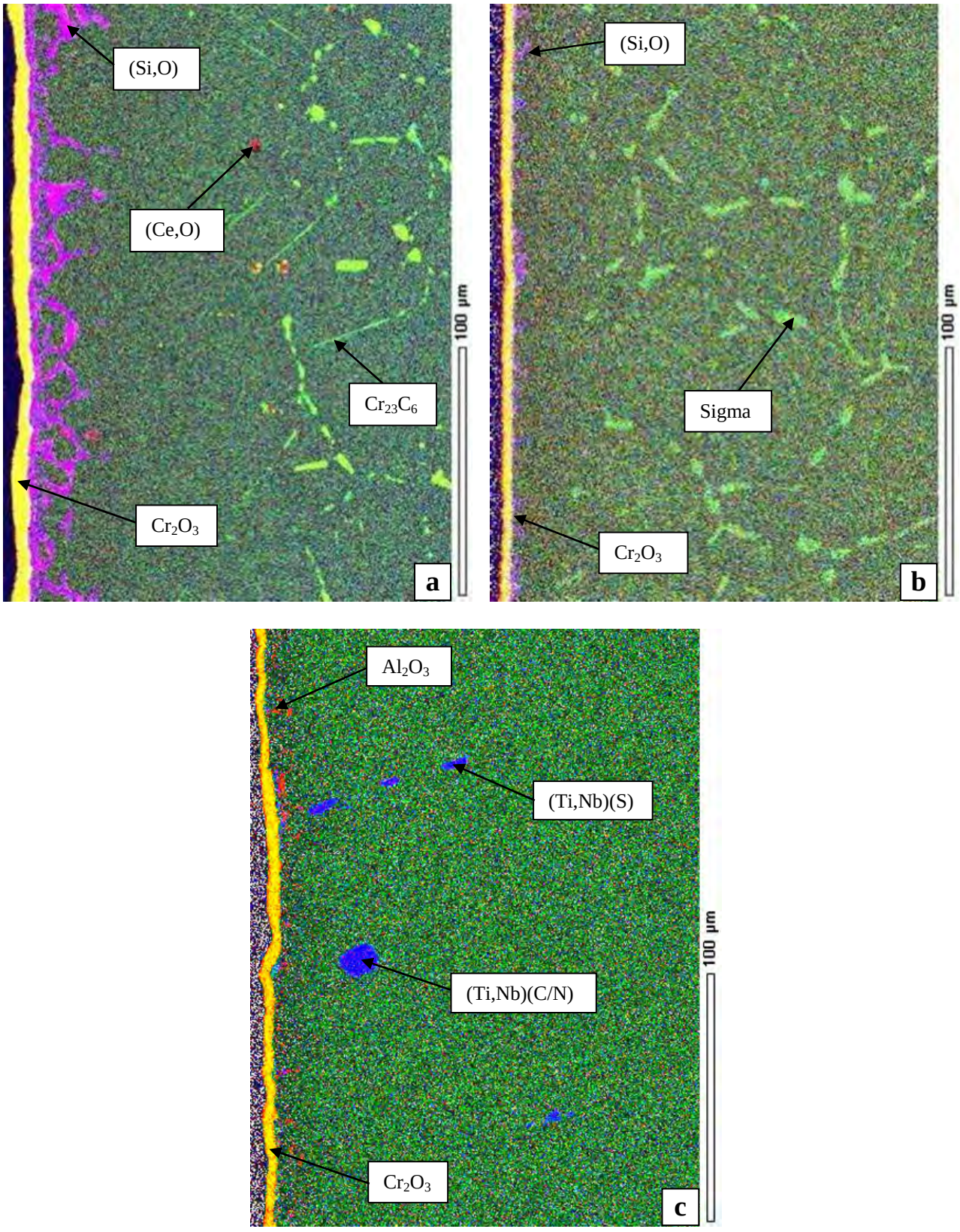

Figure 5.4: Heater head composite X-ray maps for: a) 253MA, b) 310 and c) 800H.

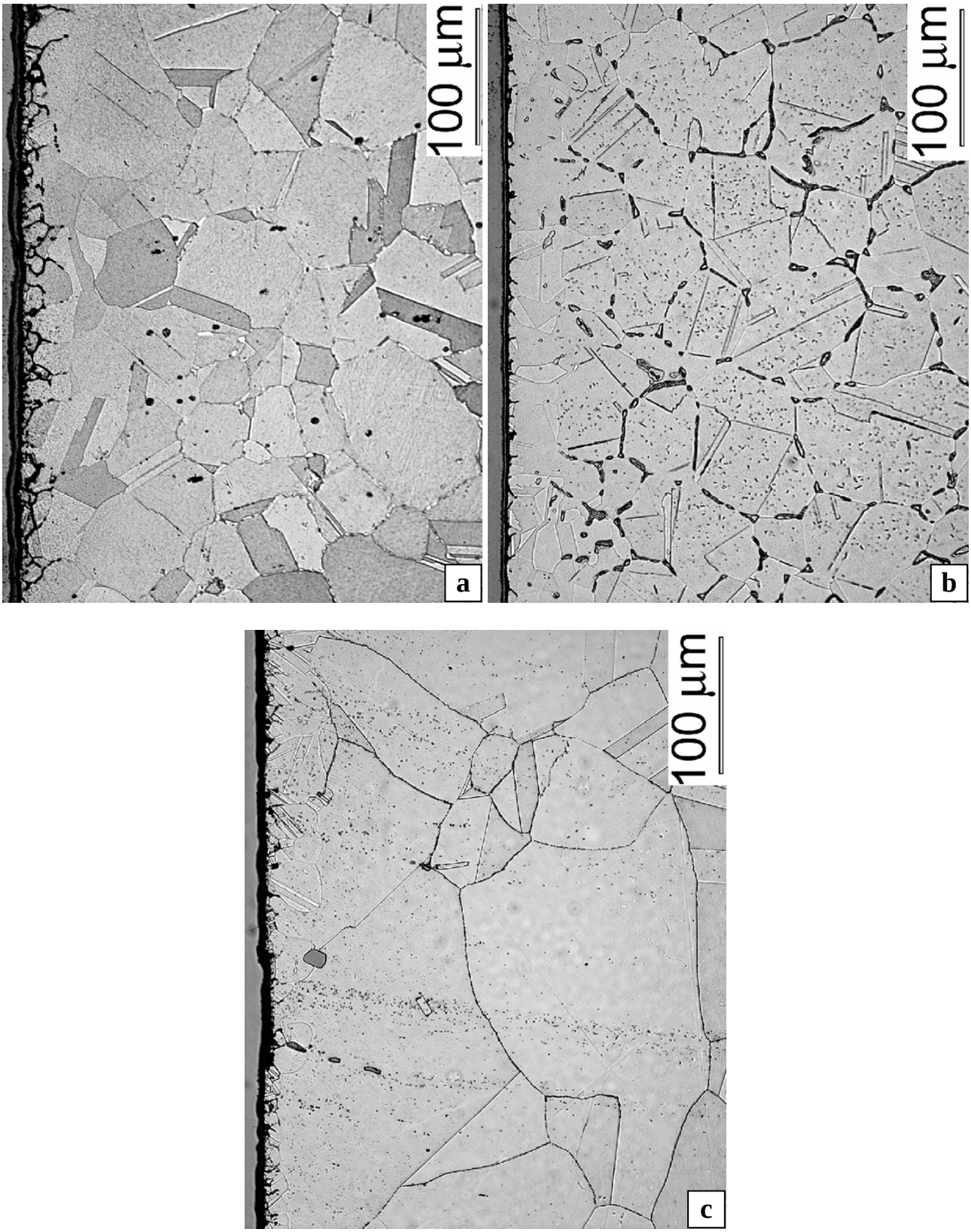

Figure 5.5: Heater head optical micrographs (etchant: glyceregia): a) 253MA, b) 310 and c) 800H.

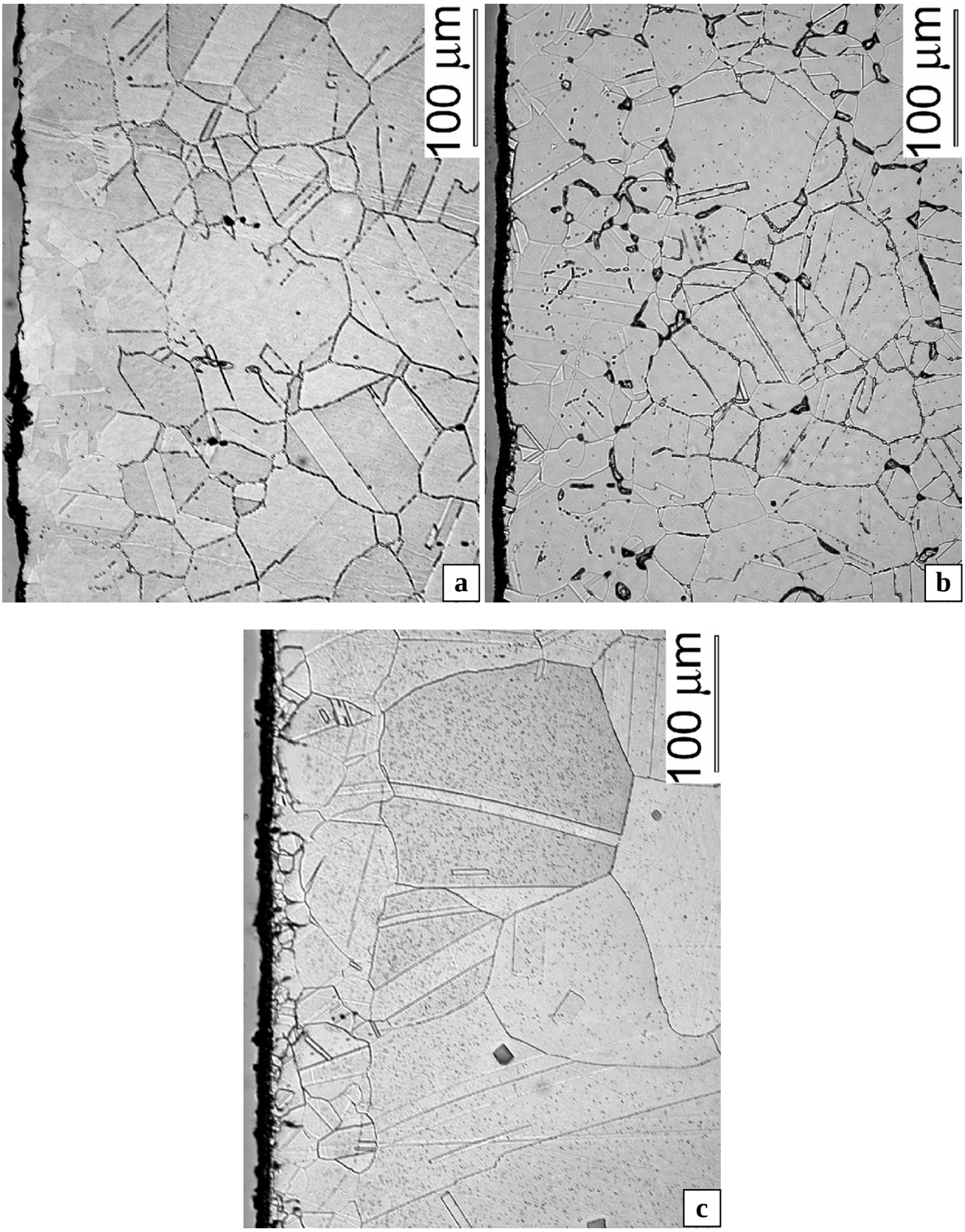

Figure 5.9: Optical micrographs (etchant: glyceregia) from tests at 900°C for 600 hours in CO/CO_2 for: a) 253MA, b) 310 and c) 800H.

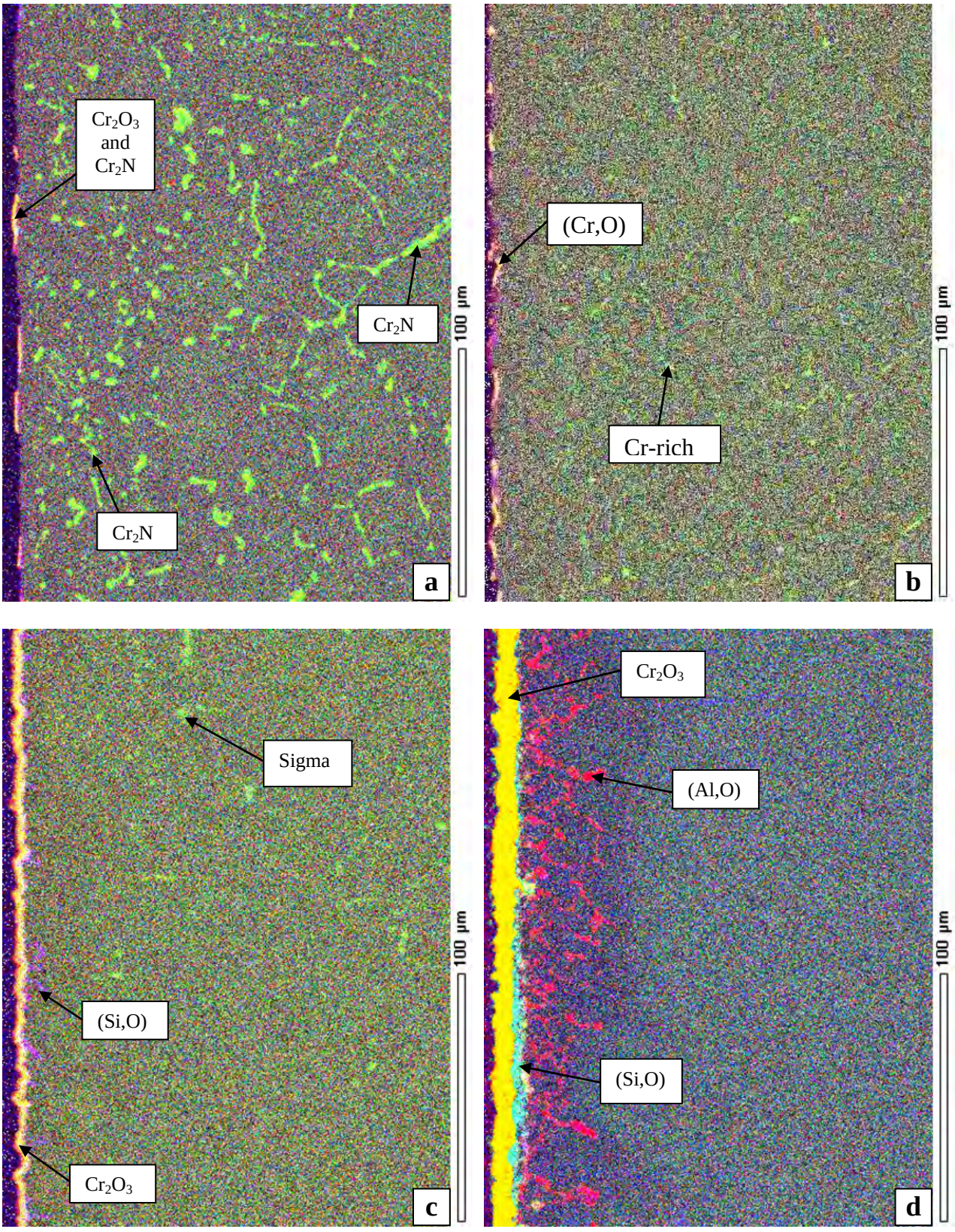

Figure 5.10: Composite X-ray maps from tests at 900°C for 300 hours in nitrogen for: a) 253MA Part 1 – extensive nitridation, b) 253MA Part 2 – less nitridation, c) 310 and d) 800H.

The X-ray map of the 253MA heater head in Figure 5.4 (a) also contains intragranular and intergranular precipitation of $Cr_{23}C_6$ throughout the sample, starting at a depth of approximately 100μm. There are two possible explanations for the area free of precipitates between the internal oxide phase and the $Cr_{23}C_6$ phase. The first possibility is that the material decarburised and was therefore too deficient in carbon near the surface to form $Cr_{23}C_6$. The second possibility is that there was a chromium deficient region beneath the scale due the diffusion of chromium toward the surface in order to form the oxide layer, and therefore insufficient chromium was present to form $Cr_{23}C_6$.

The formation of internal oxides and carbides within the 253MA heater head sample would have reduced the mechanical properties of the alloy. However, the extent of embrittlement caused by these second phases would be difficult to predict without mechanical testing. The 'sensitising' effect of $Cr_{23}C_6$ on austenitic stainless steel is not important here as the heater head is not subjected to an environment capable of attacking the chromium-deficient regions adjacent to affected grain boundaries.

The results for the 310 heater head given in Figure 5.4 (b), a composite X-ray map, and Figure 5.5 (b), an optical micrograph, show that extensive precipitation of sigma phase occurred throughout the alloy on grain boundaries. The heater head experienced internal oxidation in the form of (Si,O) along austenite grain boundaries beneath the scale to a depth of approximately 7μm. Sigma phase begins approximately 30μm beneath the scale, leaving a region free of precipitates. This region may be explained by a chromium deficiency beneath the scale caused by the diffusion of chromium towards the scale. As stated in Chapter 2, precipitation of sigma phase can cause embrittlement, the extent of which depends on the amount and distribution of the phase. Grain boundary precipitation of sigma phase, as experienced in the 310 heater head, is more detrimental than intragranular

precipitation. Mechanical testing would be required to determine the exact amount of embrittlement that occurred.

The 800H heater head results, provided in Figures 5.4 (c) and 5.5 (c), show the relative lack of second phases present in the microstructure. Al_2O_3 is present on grain boundaries beneath the scale to a depth of approximately 10μm, which is evidence of internal oxidation. The composite X-ray map in Section 5.4.1 contains titanium and niobium rich precipitates, some of which are sulfides, and some of which may be either carbides or nitrides (it is difficult to distinguish between the two with EBSD). These precipitates are the result of a heat treatment given to the alloy prior to service (see Section 2.4.3) in order to avoid sensitisation (see Section 2.6.1). MC precipitation reduces the matrix carbon content available to form $M_{23}C_6$ and therefore reduces sensitisation, which explains the absence of $Cr_{23}C_6$ in this microstructure.

A comparison of the three heater head microstructures provides interesting information. The internal oxidation experienced by the 253MA heater head is extensive, whereas the other two alloys underwent a comparatively minor amount of internal oxidation. One possible explanation for this is that the oxide scale on the 253MA heater head was less protective than the scale on the other two alloys, and therefore allowed a greater amount of oxygen ions to diffuse through the scale. The scale may also have allowed direct contact of oxygen with the alloy surface as a result of cracking, spalling or porosity, and although the scale would have healed quickly due to the high oxygen partial pressure of the environment, the extent of internal oxidation would have increased. Regardless of the explanation, it is certain that the severe internal oxidation of the 253MA heater head along grain boundaries would be more detrimental to mechanical properties (such as ductility) than the minor internal oxidation experienced by the other two heater head alloys. Oxidation was observed to be the only form of high-temperature corrosion experienced by the heater head alloys.

A number of phases can form in austenitic alloys during aging at elevated temperature. Alloy content, temperature and time of aging determine which phases form and to which extent. Alloy 800H did not form any precipiate phases during aging in the WhisperGen™ (the titanium carbides and nitrides are part of the solution treated microstructure prior to aging). This may be explained by the comparatively high nickel content of the alloy, which results in a more thermodynamically stable alloy that is more resistant to second phase precipitation. In addition, the strong carbide- and nitride-former titanium is added to soak up free carbon so that the precipitation of $M_{23}C_6$ is delayed or avoided. The 310 heater head develops detrimental sigma phase, possibly due to a higher chromium content than the other two alloys, which encourages sigma phase formation. The sigma phase formation may also be encouraged by the lower carbon content of this alloy, as carbon is an austenite stabiliser. The lowest nickel content of 253MA results in a less stable austenite prone to phase formation during aging, and the higher carbon content may provide more free carbon for $M_{23}C_6$ precipitation.

Finally, Figure 5.5 provides optical micrographs of the three heater head alloys, etched in glyceregia. These micrographs show that the 800H heater head has far larger grains than the other two heater head alloys. Although larger grain sizes provide improved creep strength, it is known (see Section 2.3.4) that the high temperature oxidation resistance of austenitic steel is improved by smaller grain sizes due to increased outward flux of chromium along grain boundaries to from protective oxide scales.

5.2.3 Discussion of Laboratory test results

A direct comparison between the X-ray maps and optical micrographs for all laboratory tests run at 900°C is provided in Figures 5.6 – 5.13. The comparison includes results for the three alloys run at

900°C for: 300 hours in CO/CO_2 (Figures 5.6 and 5.7), 600 hours in CO/CO_2 (Figures 5.8 and 5.9), 300 hours in nitrogen (Figures 5.10 and 5.11), and 600 hours in nitrogen (Figures 5.12 and 5.13).

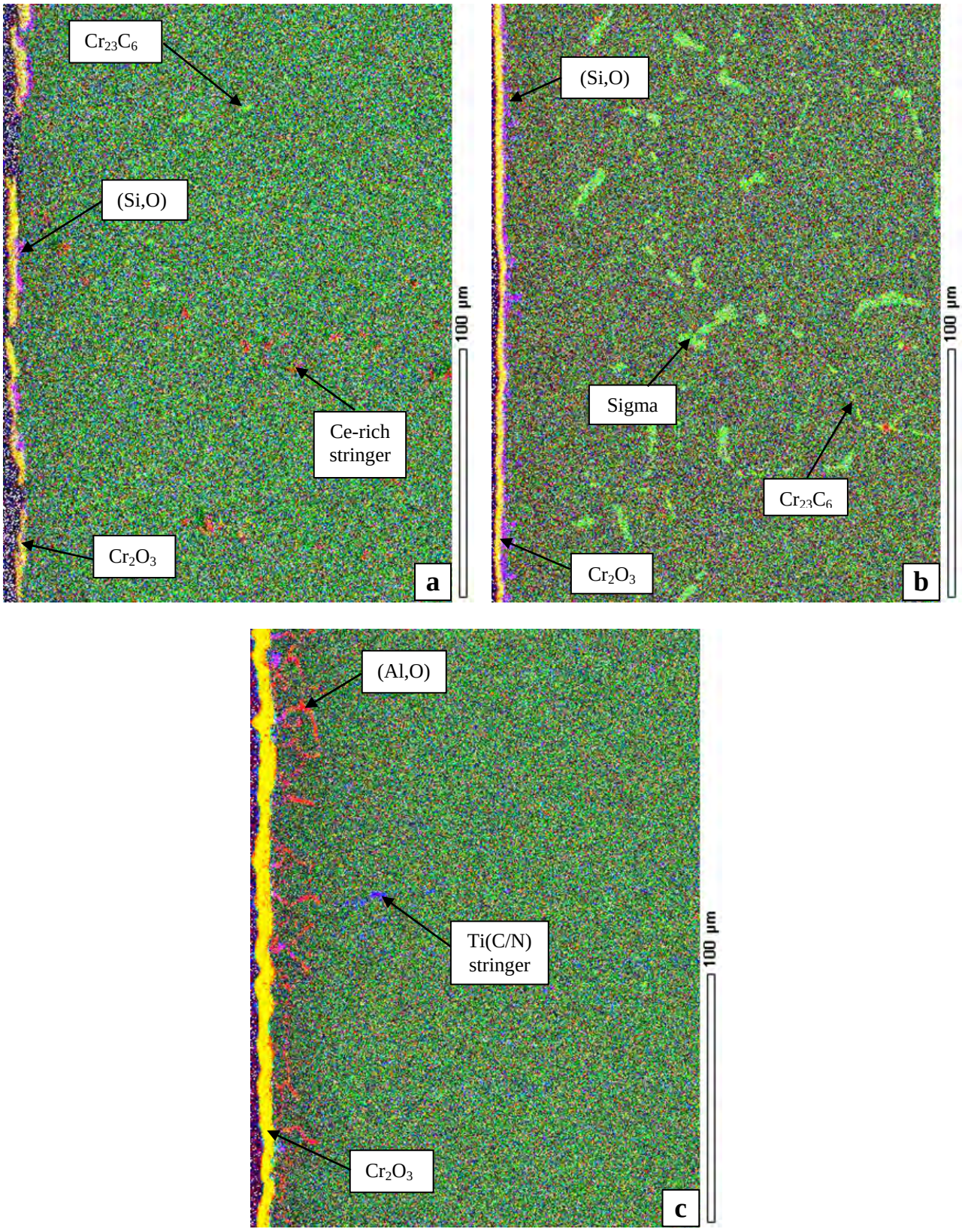

Figure 5.6: Composite X-ray maps from tests at 900°C for 300 hours in CO/CO_2 for: a) 253MA, b) 310 and c) 800H.

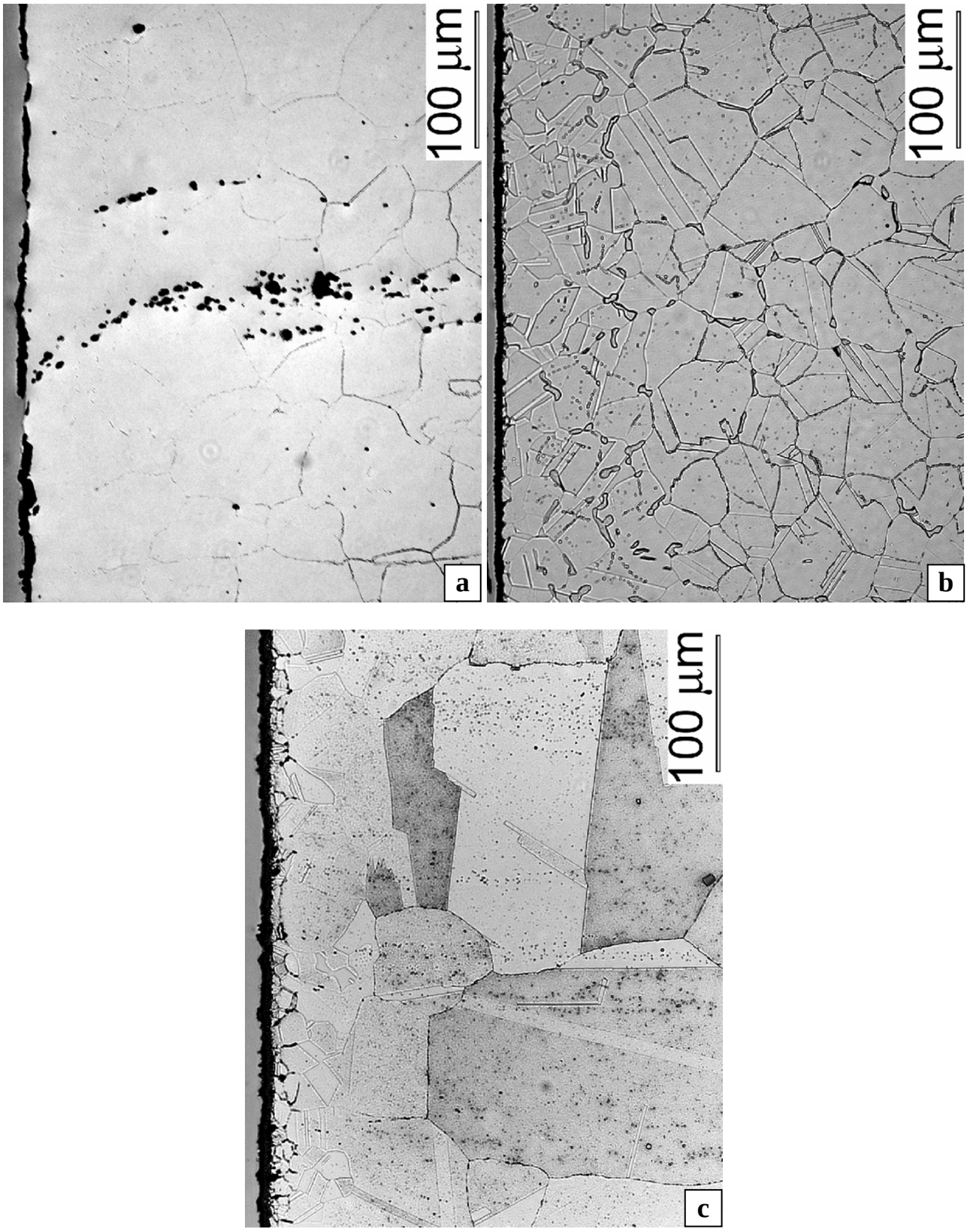

Figure 5.7: Optical micrographs (etchant: glyceregia) from tests at 900°C for 300 hours in CO/CO_2 for: a) 253MA, b) 310 and c) 800H.

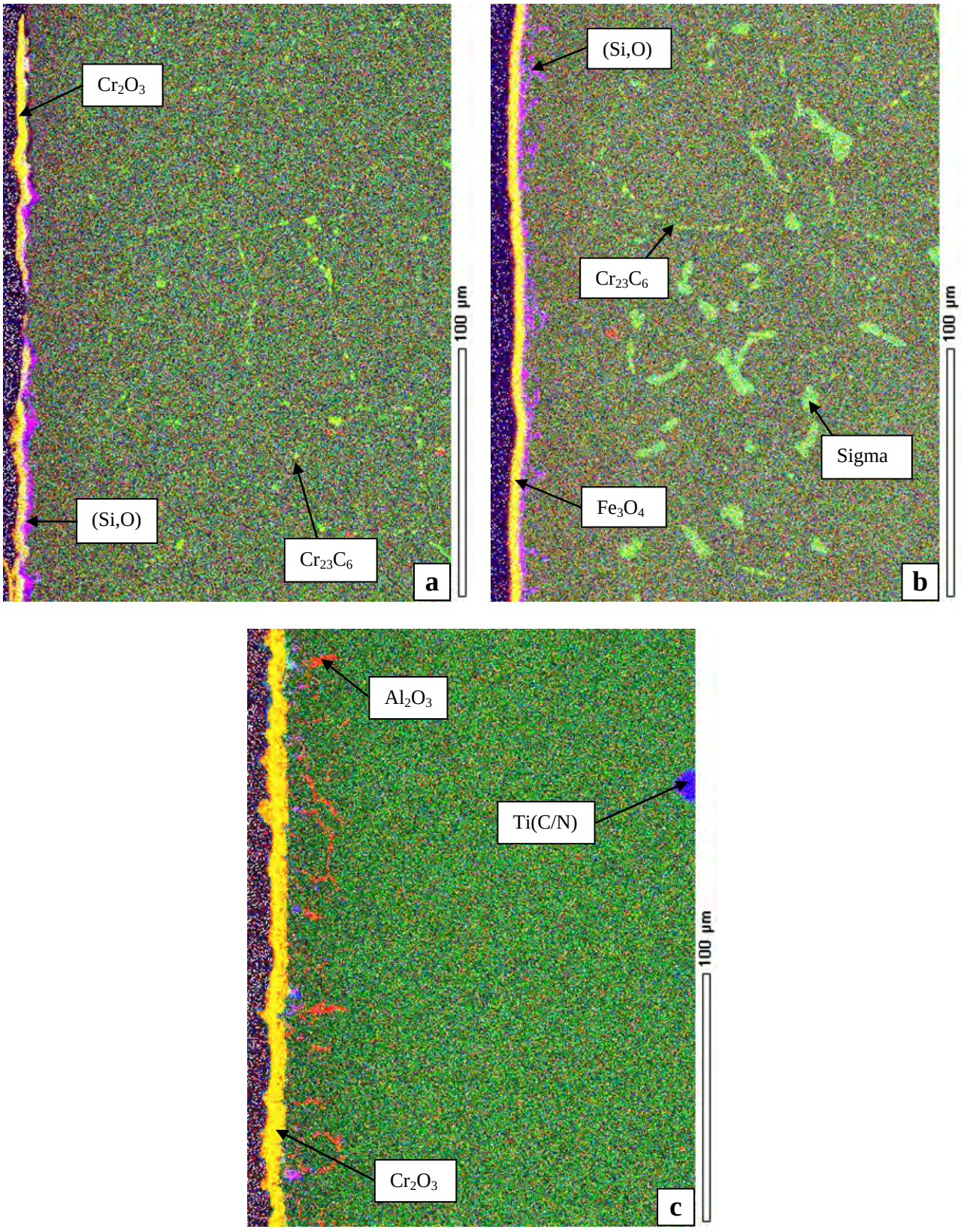

Figure 5.8: Composite X-ray maps from tests at 900°C for 600 hours in CO/CO_2 for: a) 253MA, b) 310 and c) 800H.

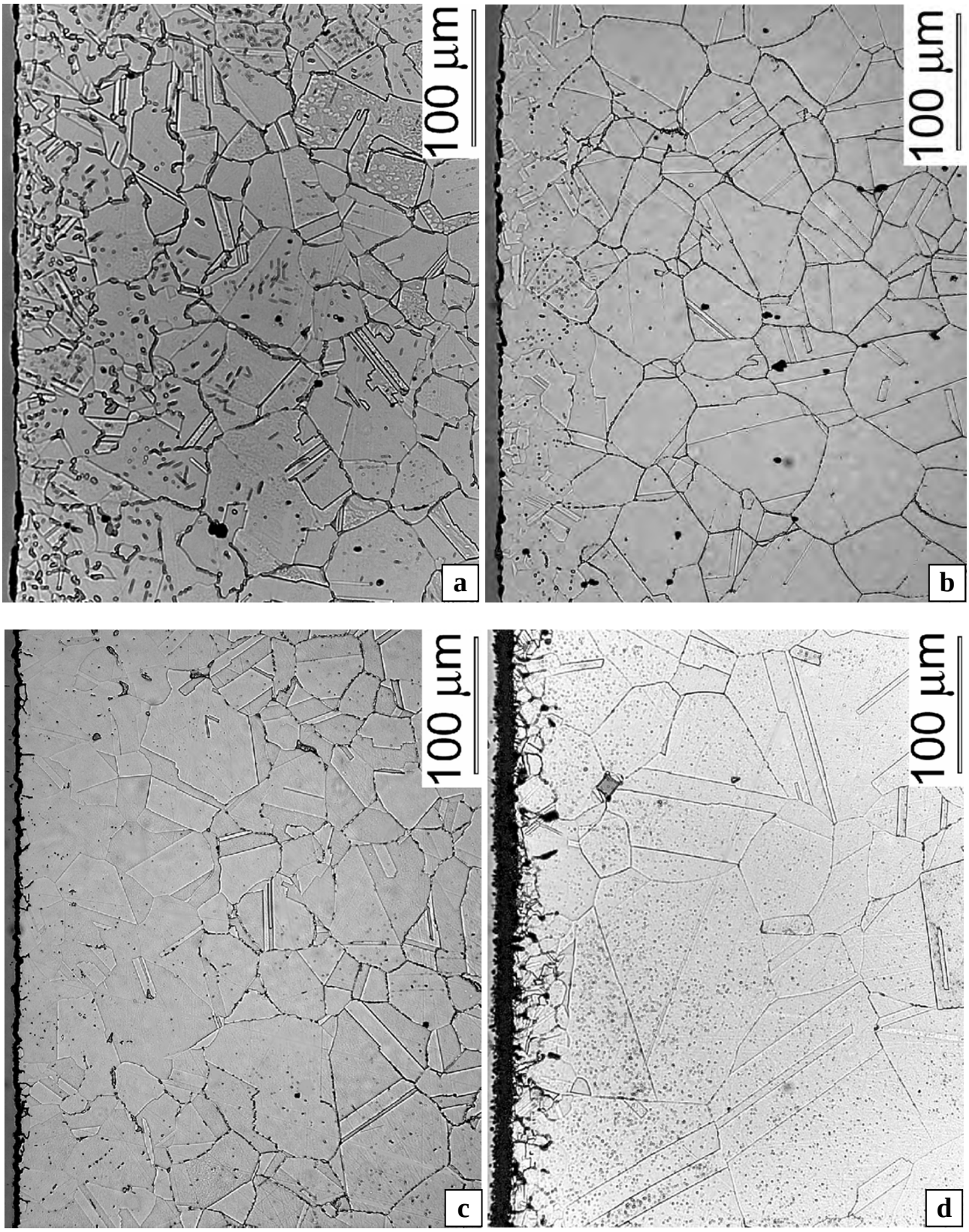

Figure 5.11: Optical micrographs (etchant: glyceregia) from tests at 900°C for 300 hours in nitrogen for: a) 253MA Part 1 – extensive nitridation, b) 253MA Part 2 – less nitridation, c) 310 and d) 800H.

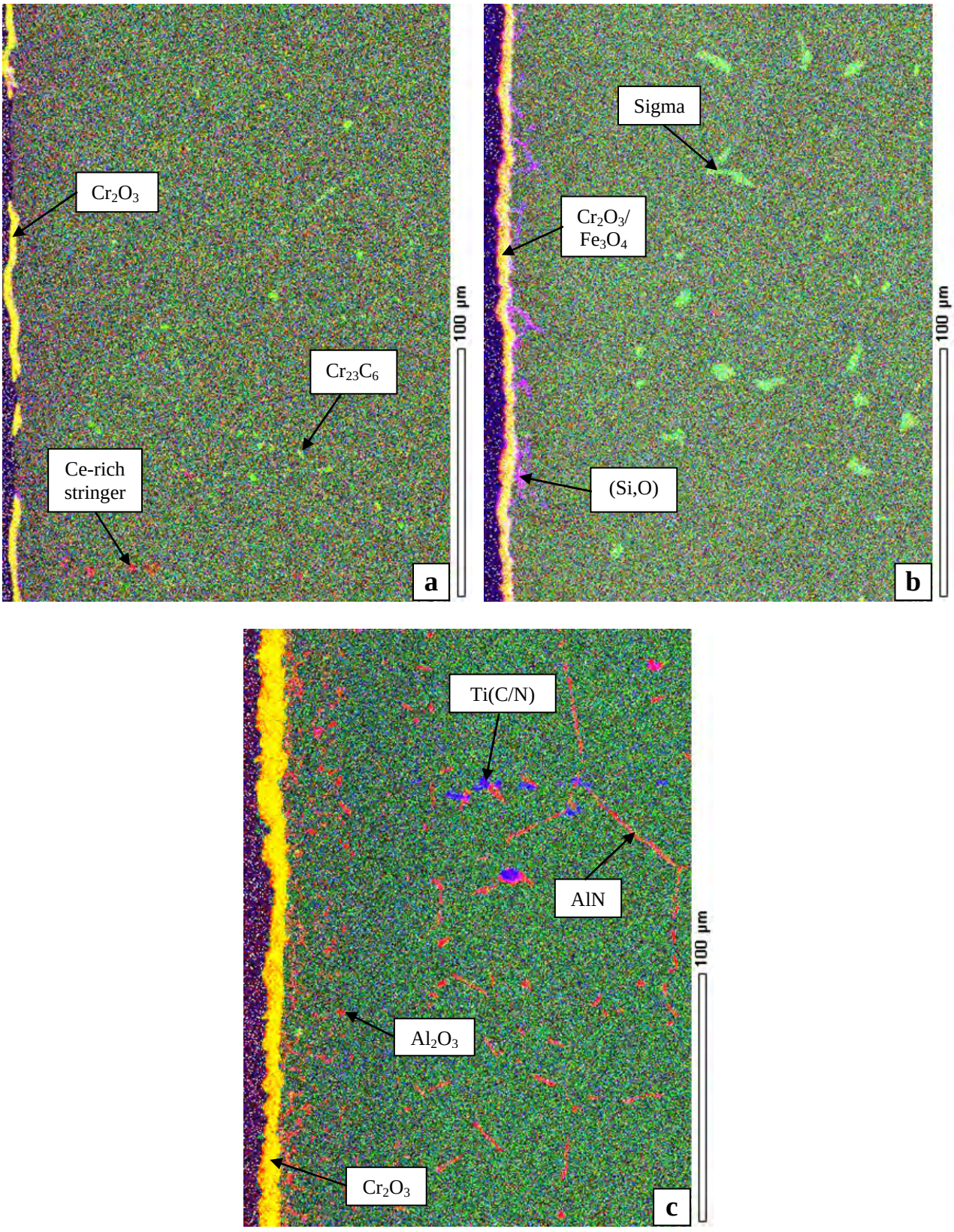

Figure 5.12: Composite X-ray maps from tests at 900°C for 600 hours in nitrogen for: a) 253MA, b) 310 and c) 800H.

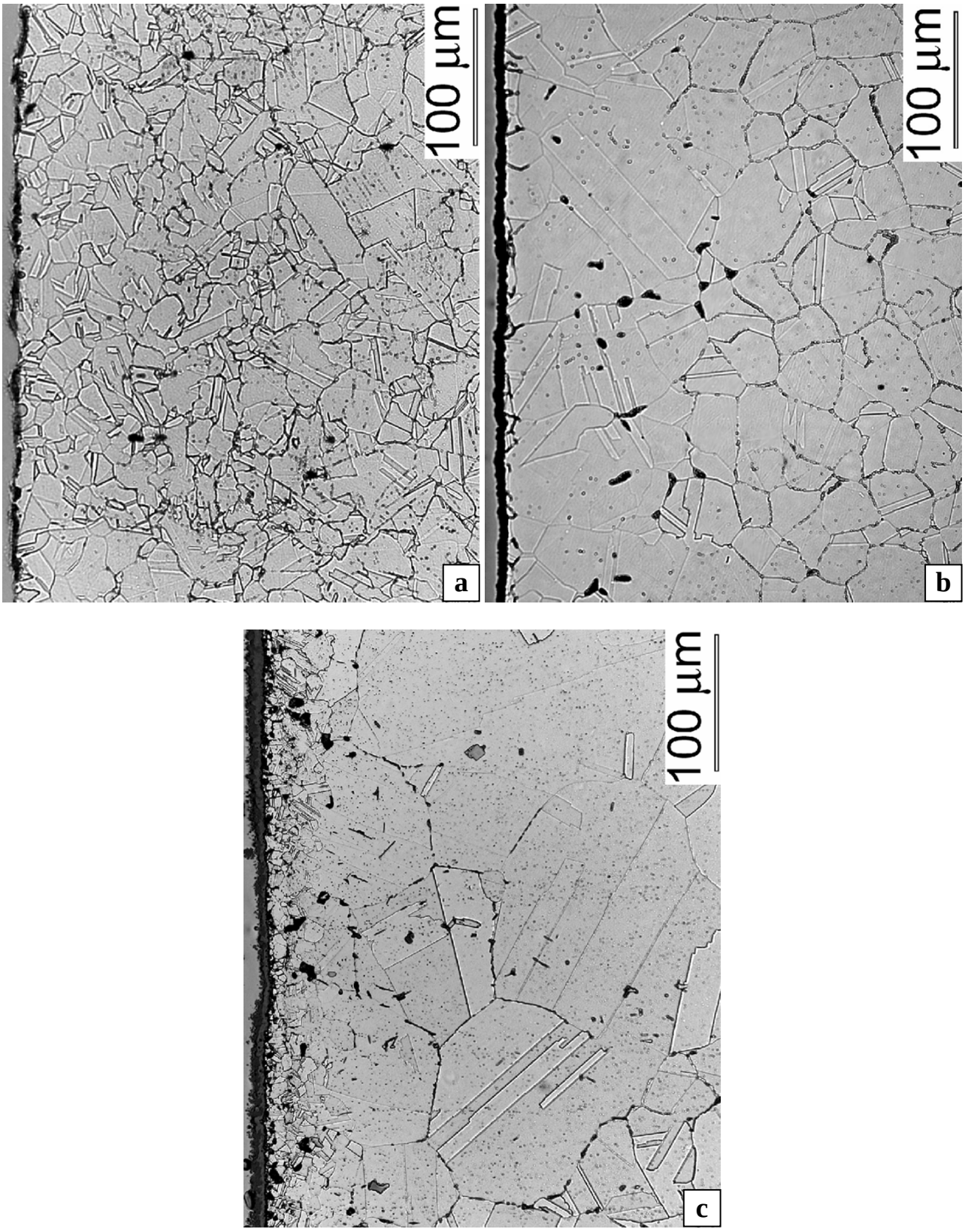

Figure 5.13: Optical micrographs (etchant: glyceregia) from tests at 900°C for 600 hours in nitrogen for: a) 253MA, b) 310 and c) 800H.

The microstructures for the laboratory tests provided a good comparison of performances for the three alloys, although some anomalies were noted. The 253MA samples held at 900°C for 300 and 600 hours in both nitrogen and CO/CO_2 (see Figures 5.6 (a), 5.8 (a), 5.10 (a) and 5.12 (a)) contain fine $Cr_{23}C_6$ precipitates on grain boundaries throughout the microstructure, although the same tests at 800°C contain more obvious $Cr_{23}C_6$ precipitation on grain boundaries throughout. The samples in which $Cr_{23}C_6$ precipitates were found contained a region beneath the scale which was free of $Cr_{23}C_6$ precipitates, suggesting that decarburisation occurred, or that the chromium-depleted region resulted in no precipitation.

The tests for 253MA at 700°C do not contain observable $Cr_{23}C_6$ with the exception of the fine precipitation found on the sample run in CO/CO_2 for 600 hours. It is stated in Section 2.6.1 that austenitic stainless steel becomes susceptible to sensitisation when in the temperature range between 480 and 815°C. This explains the smaller amount of $Cr_{23}C_6$ precipitation observed in 253MA at 900°C than at 800°C, as the precipitates would have begun to dissolve at 900°C. In every case, the 253MA samples showed very little or no evidence of internal oxidation in the form of (Si,O) phase. The extent of embrittlement caused by these phases would need to be determined with mechanical testing.

253MA samples held at 800°C for 300 and 600 hours in both CO/CO_2 and nitrogen (see atlas of microstructures on the attached CD, or Appendices E3 and E6 for a description of the microstructures) contained silicon-rich precipitates beneath the scale which could not be identified, although EBSD patterns were obtained. It is difficult to comment on these results without knowing what the phase is, and it should be noted that the presence of this phase was minimal. One particularly anomalous result was found in a 253MA sample run for 300 hours in nitrogen at 900°C (Figure 5.10 (a)). The results for this sample were so non-uniform that they were divided into two

parts (see Table E5 and/or atlas of microstructures). Part 1 underwent extensive internal nitridation in the form of Cr_2N precipitates to a depth of 130 μm beneath the scale, whereas the Cr_2N precipitates found in Part 2 went to a depth of 60 μm beneath the scale. This sample was also found to have Cr_2N present in the scale, suggesting that external nitridation also occurred. However, the sample run in nitrogen at 900°C for 600 hours (Figure 5.12 (a)) shows no sign of nitridation, which is very strange indeed. There must be either a non-intuitive explanation for this phenomenon, or an inadvertent exchange of samples occurred at an early stage of the research, despite the utmost care being taken. Further testing would allow this question to be answered.

Sigma phase appeared at every temperature in both CO/CO_2 and nitrogen for the 310 samples. However, the morphology, extent and distribution varied depending on the temperature and time of aging. Figure 5.14, Figure 5.15 and Figure 5.16 give a direct comparison between the appearance of 310 at 700, 800 and 900°C in CO/CO_2 after 600 hours, as an example. The sample at 700°C (Figure 5.14) shows that a layer of sigma phase formed beneath the scale, and a precipitate-free region exists between the layer and the scale. This region may be caused by the depletion in chromium beneath the scale. Figure 5.15 shows that the sample at 800°C developed sigma phase on grain boundaries throughout, with a concentration of sigma phase near the scale. There is again a precipitate-free region between the sigma phase and the scale, which may be explained in the aforementioned way. Figure 5.16 shows that the morphology and distribution of sigma phase at 900°C differs greatly to that at 800°C. In addition, $Cr_{23}C_6$ was found in the microstructure at 900°C, although this would seem to contradict the literature which states that $Cr_{23}C_6$ forms between 480 and 815°C (Section 2.6.1).

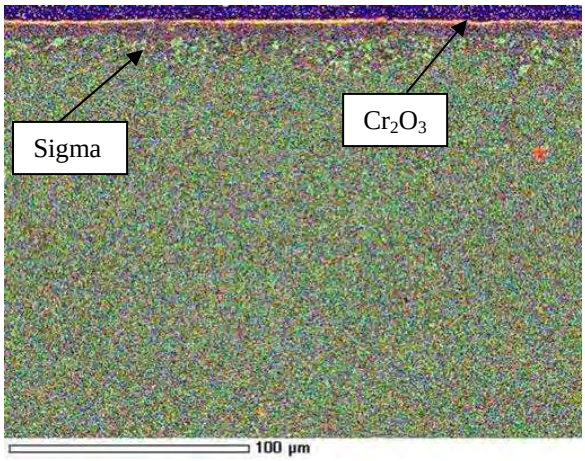

Figure 5.14: Composite X-ray map for 310 after laboratory testing in CO/CO_2 at 700°C

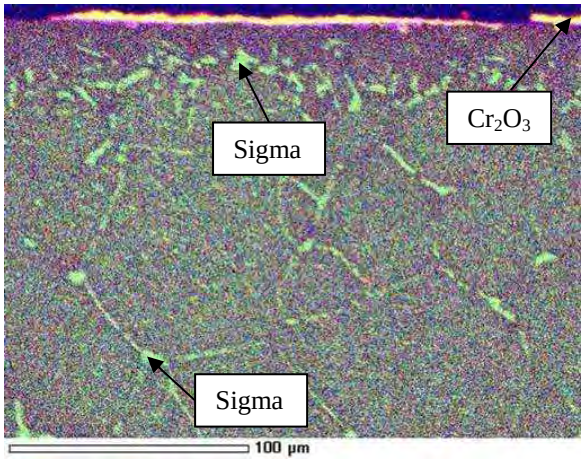

Figure 5.15: Composite X-ray map for 310 after laboratory testing in CO/CO_2 at 800°C

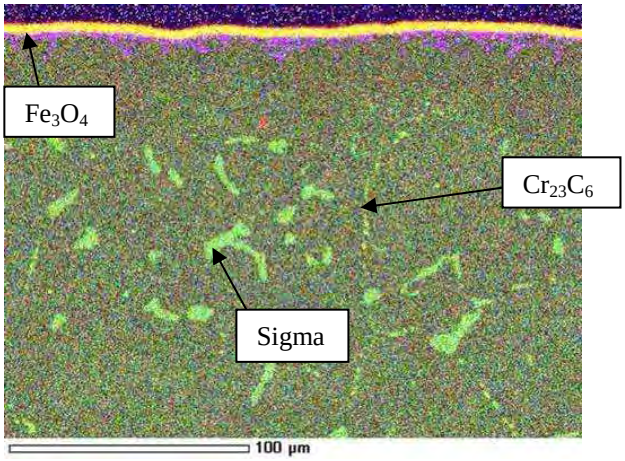

Figure 5.16: Composite X-ray map for 310 after laboratory testing in CO/CO_2 at 900°C

Some internal oxidation occurred at 900°C in the form of (Si,O) on grain boundaries beneath the scale, but the internal oxidation at 800 and 700°C was minimal or non-existent. As mentioned previously, grain boundary precipitation of sigma phase is detrimental to mechanical properties, but the exact extent would need to be determined with mechanical testing. The tests at 900°C in nitrogen gave anomalous results with very little sigma phase forming at both 300 hours and 600 hours, and this phenomenon cannot be explained at this time. An interesting finding was that after 600 hours at 900°C in both CO/CO_2 (Figure 5.8 (b)) and nitrogen (Figure 5.12 (b)), the crystal structure of the chromium-rich oxide layer transformed from Cr_2O_3 (corundum) to Fe_3O_4 (the inverse spinel magnetite). It is likely that this spinel is less protective than Cr_2O_3 and would therefore lead to a reduced resistance to high-temperature corrosion.

The 800H samples were found to be resistant to the development of precipitate phases such as $Cr_{23}C_6$ and sigma phase. The phase $Cr_{32}C_6$ was found on grain boundaries in the samples run at 800 and 700°C in CO/CO_2 (see atlas of microstructures on the attached CD for images, or Appendices E3 and E4 for a written summary of the microstructures). However, the amount of the phase found was so small that it is difficult to discern in the X-ray maps, except at magnifications such as in the example in Figure 5.17, run at 800°C for 600 hours in CO/CO_2. Also shown in this figure is the internal oxidation in the form of an aluminium-rich (Al,O) phase, the protective Cr_2O_3 layer, a titanium carbide/nitride precipitate, and the tiny titanium-rich particles that make up the stringers found throughout the 800H samples. The titanium-rich particles beneath the scale seen in the figure may have a detrimental effect on spallation resistance and are likely to be oxygen rich (although the EDS results did not conclusively show this), as titanium tends to oxidise on grain boundaries in the subsurface region of an alloy (see Section 2.9).

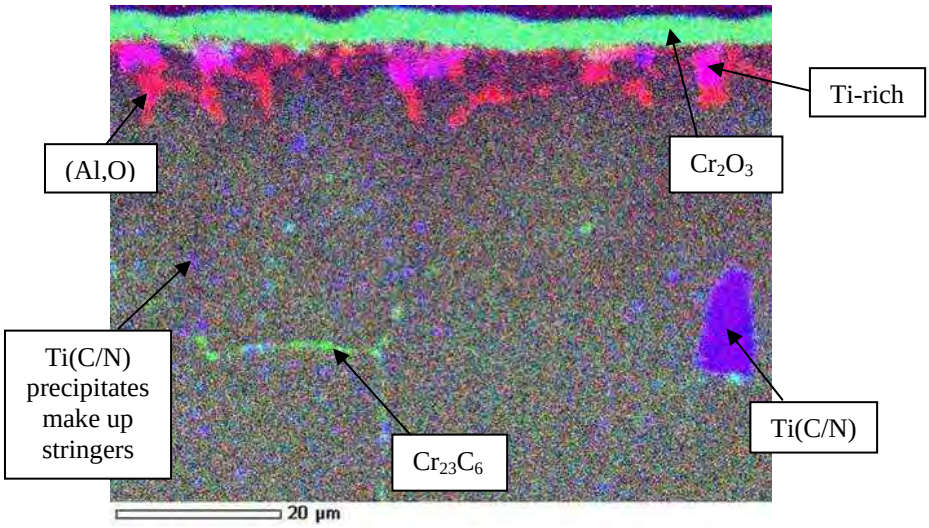

Figure 5.17: Composite X-ray map of an 800H sample run at 800°C for 600 hours in CO/CO_2

Evidence of extensive internal oxidation was found on every 800H sample run at 900°C in both nitrogen and CO/CO_2, as shown in Figures 5.6 (c), 5.8 (c), 5.10 (c), 5.12 (c). Internal oxidation was also observed to a lesser extent in the samples run at 800 and 700°C in nitrogen and CO/CO_2 (see atlas of microstructures or written summary in Appendices E3, E4, E6 and E7). The internal oxidation experienced by the 800H samples at a given temperature was far greater than that experienced by the other two alloys. This is an unexpected and currently inexplicable result, as the high nickel content of 800H has been shown to dramatically increase oxidation resistance in other studies (see Section 2.3.1). However, the consistency of this finding across all the laboratory tests makes the phenomenon difficult to dismiss as merely an anomaly. As mentioned previously, this internal oxidation would have a detrimental effect on the mechanical properties of the alloy to an extent that could only be determined by mechanical testing. Nitridation occurred in one case for the 800H sample run in nitrogen for 600 hours at 900°C (Figure 5.12 (c)). AlN can be observed on grain boundaries starting at a depth of 45µm and continuing to a depth of 330µm. No AlN precipitation was observed after 300 hours.

Stringers were observed in almost all of the 253MA and 800H laboratory samples, but were not found in any 310 samples. Figure 5.18 shows an example of the titanium carbide and/or nitride stringers found in 800H with both a low- magnification optical micrograph and a high-magnification composite X-ray map. Figure 5.19 provides an example of the cerium oxide and/or sulfide stringers found in 253MA, in the same format as was provided for 800H. Stringers are usually undesirable because they reduce mechanical properties, and cause anisotropy due to their alignment in the direction of rolling (see Section 2.5). The cerium-rich sulfide inclusions found in 253MA are preferable to detrimental manganese sulfide inclusions, and this is one of the reasons that rare earth elements are added to alloys (see Section 2.5).

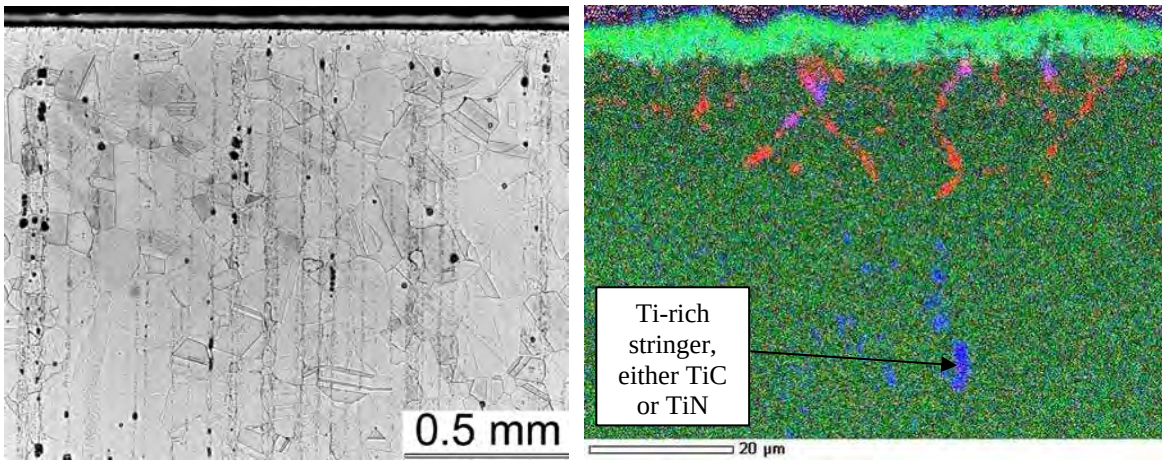

Figure 5.18: Optical micrograph (left) and composite X-ray map (right) of the 800H sample run for 300 hours in CO/CO_2 at 900°C

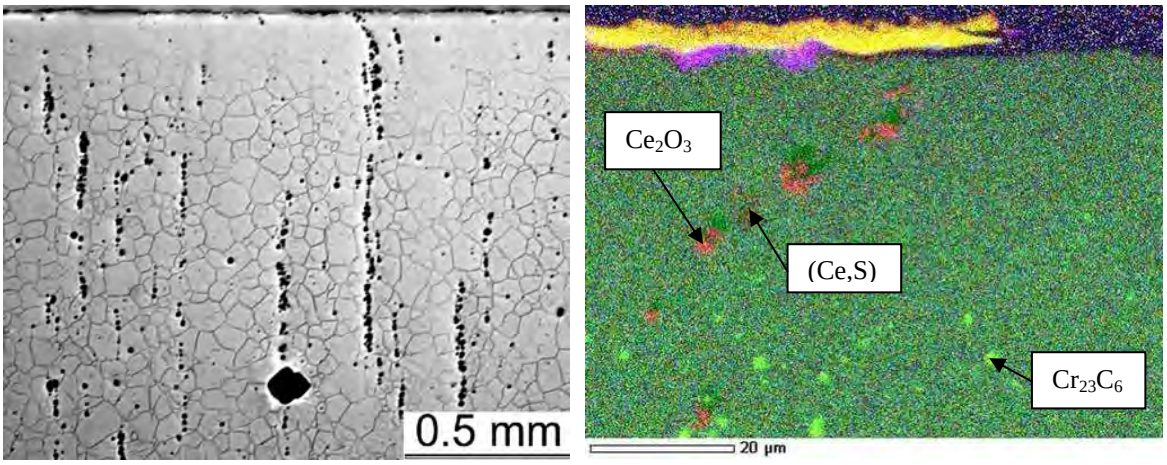

Figure 5.19: Optical micrograph (left) and composite X-ray map (right) of the 253MA sample run for 300 hours in CO/CO_2 at 900°C

5.2.4 Comparison between heater head and laboratory results

A comparison between the heater head results and laboratory results shows good similarity in some cases, but major discrepancies in other cases. The most obvious explanation for the discrepancies is the simplification of the heater head environment that allowed the laboratory tests to be undertaken at atmospheric pressure. This section provides a description of the similarities and discrepancies between the heater head and laboratory test results, and where possible gives an explanation for these observations. The laboratory test result most similar to the heater head for each alloy will be provided. Interestingly, there were similar laboratory test results to the heater head results for both 310 and 800H, but the heater head results for 253MA could not be matched to any laboratory test results.

A composite X-ray map of the 253MA heater head is compared to a composite X-ray map of the most similar laboratory result found for 253MA, that at 800°C for 600 hours in CO/CO_2, in Figure 5.20. In fact, all the 253MA samples run at 800°C in both nitrogen and CO/CO_2 were similar to the sample shown in this figure. The major discrepancies between the two results are obvious. The blatant difference in oxide appearance was explained earlier by the difference in oxygen partial

pressure (see Section 5.1 of this chapter). The extensive internal oxidation experienced by the heater head could also be due to the higher oxygen partial pressure of the heater head environment, and may have been exacerbated by repeated spalling and/or a slow initial formation of the protective oxide layer. However, it would be expected that the laboratory samples would have at least undergone some internal oxidation, especially with the absence of a protective oxide layer, and taking into account the extensive internal oxidation in 800H samples run in the same conditions.

The laboratory test result in Figure 5.20 was chosen because it displayed the greatest amount of $Cr_{23}C_6$ precipitation, which is however far less and of different morphology to the $Cr_{23}C_6$ seen in the 253MA heater head. The average temperature of the heater heads (850°C) is between the 900 and 800°C laboratory tests runs, but the $Cr_{23}C_6$ precipitation in the heater head does not in any way resemble that of the laboratory tests as expected. This discrepancy cannot be explained at this time. Decarburisation is likely to have occurred in both the heater head and laboratory samples, suggesting that the carbon activity in both the modeled environment and the WhisperGen™ environment is less than that in the alloy.

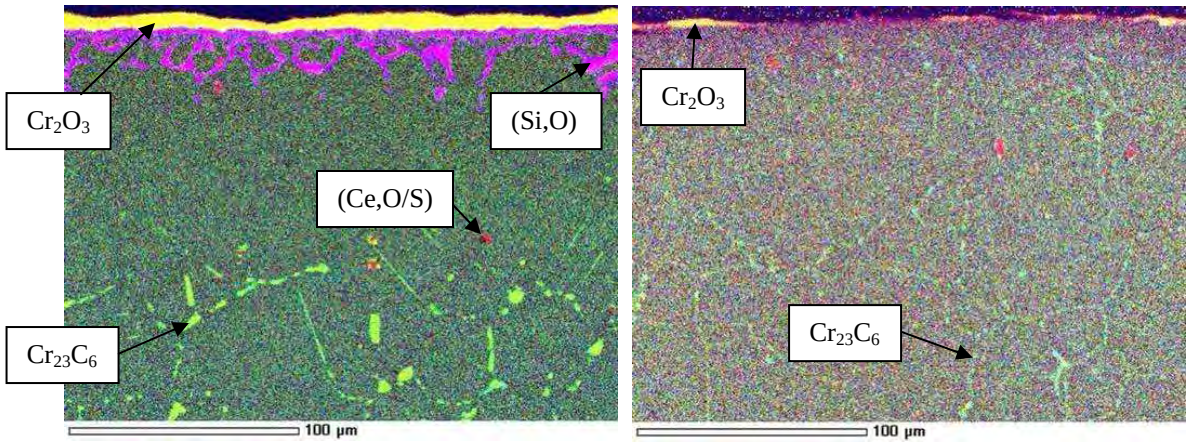

Figure 5.20: 253MA heater head after 600 hours in WhisperGen™ (left) and laboratory test run for 600 hours in CO/CO_2 at 800°C (right)

A composite X-ray map of the 310 heater head is provided along with the most similar laboratory test result in Figure 5.21. The laboratory test result in the figure was at 900°C for 600 hours in CO/CO_2. The oxide layers are of similar thickness and elemental composition, but the laboratory sample has an oxide layer with a spinel structure. The extent of internal oxidation in the form of (Si,O) is similar for both, and appears on grain boundaries beneath the scales. The amount of sigma phase present is similar, and the morphology of the sigma phase in the laboratory sample resembles that in the heater head, and is certainly a better match than at 800°C. The laboratory sample contains fine $Cr_{23}C_6$ precipitation on some grain boundaries, whereas the heater head sample was found not to contain any $Cr_{23}C_6$. This comparison shows that the simulation of the heater head environment was quite successful in the case of alloy 310.

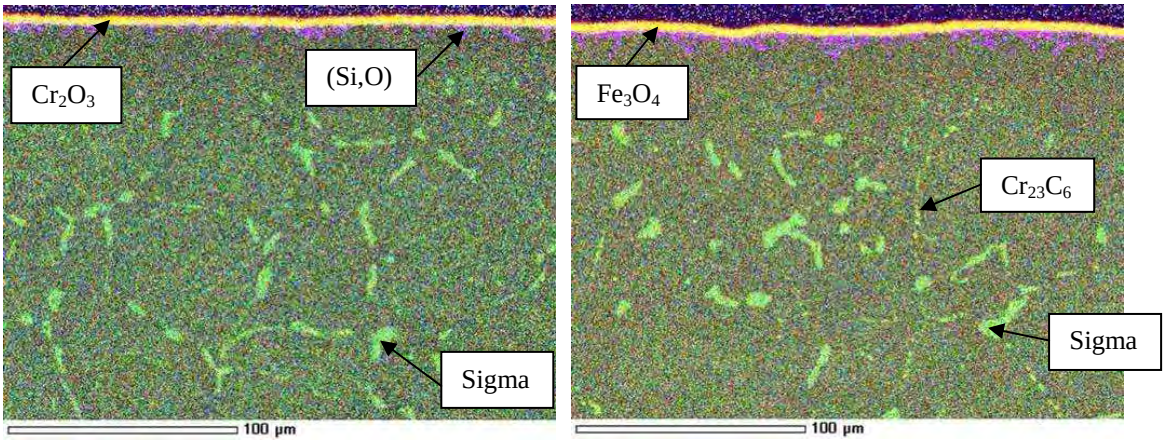

Figure 5.21: 310 heater head after 600 hours in WhisperGen™ (left) and laboratory test run for 600 hours in CO/CO_2 at 900°C (right)

The laboratory test chosen as the most similar to the 800H heater head is given in a composite X-ray map in Figure 5.22, and was run for 600 hours in CO/CO_2 at 800°C. The oxide layers are of similar thickness to each other and have the same crystal structure, and no precipitate phases were found other than the titanium-rich precipitates. The only difference is in the amount of internal oxidation, which is greater in the laboratory test. The laboratory tests at 900°C do not compare well with the heater head results, as the internal oxidation is to a far greater extent, and the thickness of

the oxide layers is greater. These results may suggest that the heater heads are subjected to a temperature closer to 800°C than 900°C, although the 310 laboratory tests contradict this theory.

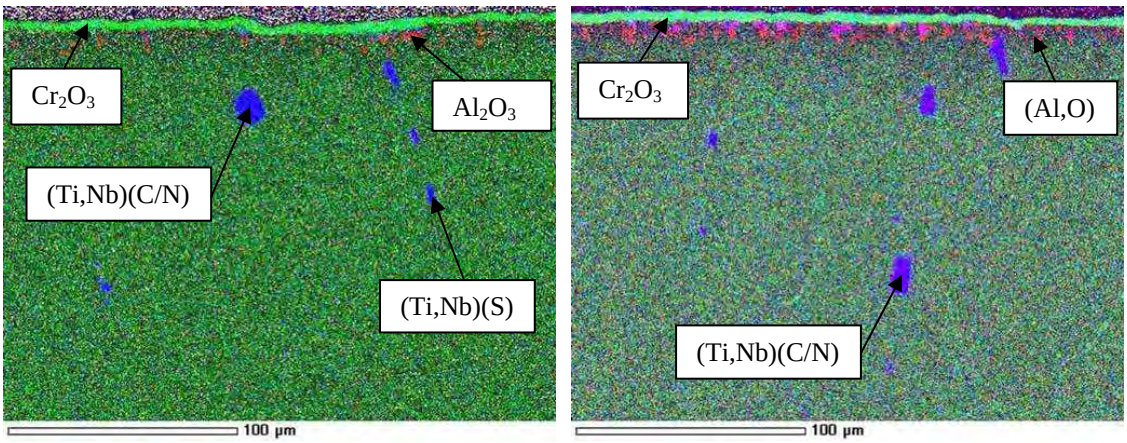

Figure 5.22: 800H heater head after 600 hours in WhisperGen™ (left) and laboratory test run for 600 hours in CO/CO_2 at 800°C (right)

This section has shown that a number of discrepancies as well as similarities were found between the heater head and laboratory results. Stringers were found in both the heater head and laboratory samples for 253MA and 800H, but not for 310. These stringers lead to a reduction in mechanical properties for these alloys, as mentioned earlier in this section. The 253MA heater head results were found not to match any of the laboratory results, due to the extensive internal oxidation and pronounced development of $Cr_{23}C_6$ within the microstructure, neither of which was observed in the laboratory tests. The 310 and 800H heater head results were better matched to the laboratory tests. However, the occurrence of extensive internal oxidation in the 800H laboratory samples at 900°C when the 253MA samples at the same temperature did not undergo any internal oxidation is a phenomenon that cannot be explained.

Nitridation was observed in the laboratory tests at 900°C in nitrogen for both 253MA and 800H, but it was not observed in the heater head samples. Possible explanations for this include the higher temperature of 900°C that the laboratory tests were conducted at, compared to the approximate

850°C that the heater heads were run at. The other factor to be considered is that the nitrogen activity of the laboratory test environment was not adjusted to the same activity as the heater head environment, due to practicality issues that were discussed in Chapter 3 of this thesis. Finally, a low oxygen partial pressure such as that in the laboratory test environment causes an increase in modes of high-temperature corrosion such as nitridation (see Section 2.3.1).

The discrepancies between the 253MA heater head and laboratory test results were a result of the over-simplification of the heater head environment that was necessary in order to conduct the tests without the use of a pressure vessel. In order to simulate the heater head environment it was necessary to decouple the effects of the carbon and nitrogen chemical potentials, which meant that the combined effects of nitrogen and carbon were neglected. It also meant that the effects of oxygen and hydrogen could not be included in the simulation. This lack of control of oxygen partial pressure was subsequently shown to have added to the discrepancies between the results, especially for 253MA, as both the internal and external oxidation observations were very different. A further complication of neglecting the difference in oxygen partial pressure was that forms of high-temperature corrosion such as nitridation and carburisation are more prominent at low oxygen partial pressures (see Section 2.3.1).

Furthermore, it was not possible to implement the nitrogen chemical potential experiments once the decoupling calculations were received, due to the practical impossibility of producing the gas mixture required (see Chapter 3 for details). A pure nitrogen gas mixture was therefore used with the aim of producing results indicative of the effect of nitrogen activity on the three alloys. These tests were useful in showing that pure nitrogen can nitride the alloys 253MA and 800H at 900°C, but not at 800°C. The assumption of equilibrium in the gas mixtures of CO/CO_2 calculated using

Thermo-Calc™ Software in order to reach the correct carbon chemical potential may or may not be correct, although a catalyst was used to promote equilibrium (see Chapter 3).

Overall, this method of modelling the heater head environment appears to be over-simplified, and could be improved upon. It appears that the method is sufficient for modelling the performance of 310 and 800H in the heater head environment, but not for 253MA. The fact that the model was better for 310 at 900°C, but was better for 800H at 800°C is difficult to explain. There were some other anomalies that could not be explained. The results suggest that 800H is more susceptible to internal oxidation at low oxygen partial pressures than the other two alloys, while 253MA is more susceptible to internal oxidation at high oxygen partial pressures than the other two alloys.

The development of precipitate phases within the heater head microstructures is an important aspect of performance for the three alloys, but this simulation was not successful in recreating the precipitate phases found in the 253MA heater head. The only form of high-temperature corrosion observed was oxidation in both the heater heads and laboratory tests, and alloy 310 was overall the most resistant alloy to internal oxidation. This is not to say that the carbon activity of the heater head environment is not important, as decarburisation was found to have occurred in the 253MA heater head, suggesting that the carbon activity of the heater head environment is less than that in the alloy. This decarburisation could be avoided either by increasing the carbon activity of the heater head environment, or by decreasing the carbon content of the alloy. Alloy 800H was in all cases the most resistant alloy to the development of precipitate phases, as a result of the high nickel content.

5.3 Material Selection

A major aim of this thesis was to compare the performance of three potential heater head alloys in a high-temperature, high-pressure environment. In order to achieve this, the heater head environment was simulated in a laboratory setting, and the results were compared with those found in an actual engine. Although the simulation of the heater head environment produced some discrepancies, the testing yielded much important information that will enable a sensible material selection. There are many factors involved in selecting a suitable alloy for this application, including resistance to spalling, high-temperature internal oxidation, decarburisation and the formation of detrimental precipitate phases. In addition, a most important factor from a commercial perspective is expense of the alloy. This section provides an overview of aspects that should be considered when choosing an alloy for the heater head application in a WhisperGen^{TM}. A summary of these aspects is presented in Table 5.4.

Table 5.4: A summary of the different factors to be taken into account during the material selection process

	253MA	310	800H
Spalling performance	By far worst in laboratory tests	Good in laboratory tests but spinel present in scale for laboratory tests at 900°C	Excellent in laboratory tests
Precipitate phases	Large amount of $Cr_{23}C_6$ in heater head	Large amount of sigma phase in heater head and laboratory tests	Minimal in heater head and laboratory tests
High-temperature corrosion	Internal oxidation in heater head but not in laboratory tests; nitridation in nitrogen laboratory test at 900°C; decarburisation in heater head	Small amount of internal oxidation in heater head and in laboratory tests	Internal oxidation minimal in heater head; extensive internal oxidation in laboratory tests at 900°C; nitridation in nitrogen laboratory test at 900°C
Expense	Medium	Least	Greatest
Mechanical properties (prior to aging)	Good	Inferior to 800H and 253MA	Good
Nickel content	~10%	~20%	~30%
Presence of stringers	Yes	No	Yes

The simulation of the heater head environment was not successful for 253MA. Nevertheless, 253MA was shown by the laboratory testing to be the most inferior of the three alloys in terms of resistance to spalling. Undesirable Ce-rich stringers were found throughout the alloy in the direction of rolling for the heater head and the majority of the laboratory test samples. Severe internal oxidation was observed in the 253MA heater head, although very little was observed in the laboratory tests regardless of temperature, an inexplicable phenomenon at this time. The 253MA heater head developed $Cr_{23}C_6$ to a far greater extent than in the laboratory tests, and was found to undergo decarburisation. The $Cr_{23}C_6$ will contribute to a reduction in mechanical properties to an unknown extent, but sensitisation is not an issue in this environment. Nitridation was found to occur at 900°C in pure nitrogen, possibly as a result of the low oxygen partial pressure of the gas.

The poor spalling performance of 253MA in the laboratory tests is likely a result of the low nickel content of the alloy, and the large silicon additions that contribute to spalling. The low nickel content of the alloy does lead to a lower cost, although the addition of cerium somewhat offsets this and makes 253MA a more expensive alloy than 310, which has double the nickel content of 253MA.

The laboratory simulation of the heater head environment for 310 was quite successful at 900°C. The laboratory tests showed that the spalling performance of 310 is far better than 253MA, but slightly inferior to that of 800H. The alloy experienced minimal internal oxidation in both the heater head and laboratory tests, and nitridation was not observed in either case. Other advantages of 310 over 253MA are the relatively lower expense, and the lack of stringers that reduce mechanical properties. However, the major disadvantages are the inferior mechanical properties of 310 prior to aging, in comparison to 253MA and 800H (see Table 2.3), and the development of embrittling sigma phase in the heater head and at all three temperatures of the laboratory tests. The sigma phase formation is encouraged by the relatively high chromium content of the alloy, and the relatively low carbon content. An additional drawback of 310 is the spinel (Fe_3O_4) crystal structure found in the scale after testing at 900°C for 600 hours, which leads to a reduction in the protectiveness of the scale against high-temperature corrosion.

The laboratory simulation of the 800H heater head was successful for the laboratory tests run at 800°C. The 800H laboratory samples did not exhibit spalling on any occasion during the laboratory testing, as a result of an adherent Cr_2O_3 scale. Extensive internal oxidation and some nitridation was found in the 800H laboratory samples (run at a low oxygen partial pressure), but only a small amount of internal oxidation was found on the 800H heater head, and nitridation had not occurred on the heater head. Potentially detrimental titanium-rich stringers were found throughout the alloy

in the heater head and in almost every laboratory test. A distinct advantage of alloy 800H was the minimal amount of potentially embrittling precipitate phases found in both the heater head and the laboratory tests at all three temperatures. The lack of precipitate phases and the superior adherence of the oxide layer in 800H can be explained by the high nickel content of the alloy which acts as an austenite stabiliser. The only disadvantage of this high nickel content is the associated cost increase, which is an important factor for commercial applications such as the WhisperGen™.

References

[1] B. Gleeson, B. Li, "Cyclic oxidation of chromia-scale forming alloys: Lifetime prediction and accounting for the effects of major and minor alloying additions", Les Embiez, France, **2004**.

6 Summary and Conclusions

WhisperGen^{TM} heater heads are subjected to a high-pressure, high-temperature, nitrogen-based environment with carbonaceous impurities. The scale formed on the heater heads during service spalls as a result of thermal cycling, leading to a reduction in engine performance. This thesis compares the performance of alloys AISI 310 and Incoloy 800H to the performance of the current heater head material, Sandvik 253MA, with the aim of recommending the most suitable alloy for the heater head application.

A review (see Chapter 2) of the literature surrounding the high-temperature corrosion of austenitic alloys revealed a lack of publications about the effects of an environment similar to that of a WhisperGen^{TM} heater head. However, the review did predict that alloys with a higher nickel content, such as Incoloy 800H (~30% nickel) would generally perform better in a high-temperature environment than alloys with lower nickel contents such as Sandvik 253MA (~10% nickel) and AISI 310 (~20%).

The austenitic alloys Sandvik 253MA, AISI 310 and Incoloy 800H rely on the formation of a protective chromia (Cr_2O_3) layer for resistance to high-temperature corrosion. The protectiveness of this layer may be impaired by the occurrence of cracking and spalling during creep, growth or thermal cycling, and the spalling resistance of an oxide layer for a given alloy is determined largely by alloy content. Because alloying additions affect the performance of an alloy collectively, experiments are usually required to establish the performance of an alloy under specific conditions. The lack of specific literature led to the decision that a systematic experimental study was necessary to compare the performance of the three alloys in the heater head environment.

In order to conduct a systematic study under controlled conditions, a repeatable experimental setup was designed to simulate the effect of the heater head environment on the performance of the three alloys. It proved impractical to conduct the tests in a pressure vessel, so an alternative method was used to simulate the effect of pressure. For this method the composition of the gas mixture used at 1 bar was determined by Thermo-Calc™ software, such that the equilibrium chemical potentials of the gas mixture at 24 bar matched those at 1 bar.

The actual gas composition obtained during service is complex since many gases are present in the mixture. Therefore, it was necessary to study the effects of the carbon and nitrogen activity separately, and neglect the potential effects of oxygen and hydrogen activity on the alloys, and also neglect the synergistic effect. The experiments were conducted by placing the alloy samples in a silica glass tube inside a furnace, with a gas mixture flowing through the tube. Tests were run at temperatures of 900, 800 and 700°C for times of 300 and 600 hours. The CO/CO_2 gas mixture was selected to achieve the appropriate activity for each of the three temperatures. The effects of exposure to nitrogen at high temperature were more simply studied using only industrial grade nitrogen gas. Thus, in total, twelve different laboratory tests were run on three different alloys, which resulted in thirty-six samples.

After testing, the samples were prepared for metallographic examination and analysed with optical microscopy, scanning electron microscopy and X-ray mapping. Electron back scatter diffraction (EBSD) was used for phase identification. In addition, the weight of each sample was measured before and after testing to allow a weight-change comparison.

The analysis of laboratory test samples led to a clear comparison between the spalling performances of the three alloys. The results showed that Incoloy 800H is the alloy least likely to spall, followed by AISI 310, with Sandvik 253MA by far the most inferior alloy in terms of spalling resistance.

An additional test was conducted in a WhisperGen^{TM} with heater heads made out of each of the three alloys. After 600 hours of service the heater heads were sectioned and observed in the same manner as the laboratory test samples, which allowed a direct comparison of the heater head results with the laboratory test results.

An analysis of the heater head microstructures provided particularly useful information that may offer an indication of service performance. Note that heater heads saw service for only 600 hours, and that actual service life should be at least 20,000 hours. Interestingly, the only form of high-temperature corrosion observed was oxidation. The 253MA heater head exhibited severe internal oxidation, while the other two alloys underwent minimal internal oxidation. It was, in fact, the development of precipitates within the alloys that showed the greatest contrast. The 253MA heater head developed a large amount of $Cr_{23}C_6$, and underwent decarburisation near the surface, which means that the carbon activity of the heater head environment must have been lower than that in the alloy. A great amount of sigma phase formation occurred in the 310 heater head, and studies have shown that the presence of this phase on grain boundaries causes severe embrittlement. The superiority of alloy 800H shown in laboratory tests was confirmed in the heater head results, as the alloy did not exhibit any evidence of internal oxidation or development of sigma/carbide phases.

However, spalling was not observed on the heater head tests. This may be due to the difference in oxygen partial pressure at which the tests were conducted, and does not necessarily mean that spalling did not occur on the heater heads. This introduces an important issue: if spalling is not

observed, then it is not possible to say it definitely does not occur, as the oxide layer may have healed after spalling, especially in high oxygen partial pressures.

The success of the heater head simulation was assessed by comparing the heater head microstructures with the laboratory test microstructures. Laboratory test results similar to the heater head results were found for both 800H and 310, but none of the 253MA heater head results were similar to the laboratory test results. The amount of $Cr_{23}C_6$ precipitation seen in the 253MA heater head was far greater, and of different morphology, than that observed in the 253MA laboratory tests at any temperature, and this result cannot be explained at this time. A similar extent and morphology of sigma phase to that in the 310 heater head was observed in the laboratory test run at 900°C for 600 hours in CO/CO_2. The best match for the 800H heater head was with the laboratory test run at 800°C for 600 hours in CO/CO_2. Although the 800H laboratory test coupon run for 600 hours at 900°C exhibited a similar lack of precipitate phases to the 800H heater head, the extent of internal oxidation was inexplicably greater.

Although the laboratory simulation of the heater head environment produced some discrepancies, the testing results revealed information that will allow the selection of the most suitable material for the heater head component. The selection process for a suitable alloy will need to consider several factors, including the resistance of the alloy to: spalling, high-temperature internal oxidation, decarburisation and the formation of potentially detrimental phases.

The present work showed that Incoloy 800H outperforms AISI 310 and Sandvik 253MA both in terms of resistance to spalling and resistance to the formation of precipitate phases. AISI 310 is recommended over Sandvik 253MA from a spalling perspective, but AISI 310 has inferior mechanical properties to Sandvik 253MA prior to service. Interestingly, AISI 310 was the only

alloy out of the three that did not contain potentially detrimental stringers. AISI 310 was shown to be undesirable due to the formation of embritting sigma phase, while the microstructure of the Sandvik 253MA heater head was undesirable due to the presence of internal oxidation, decarburisation and large amounts of $Cr_{23}C_6$. Therefore, Incoloy 800H is recommended as the most suitable alloy for the heater head application.

7 Recommendations for Future Work

A more accurate simulation of service conditions, i.e. composition and pressure, should be done. The discrepancies in the simulation of the heater head environment were most likely caused by an over-simplification in the method of modeling, which was necessary in order to avoid the use of a pressure vessel. Further experimental work in this topic may involve the use of a pressurised environment. A pressure vessel test would result in ever-diminishing gas concentration. However, the actual engine working gas is continually changing with an ever-increasing trace gas composition, and this simulation is best accomplished with flowing gases of controlled composition.

The use of cyclic testing would ascertain the extent of spalling observed after multiple thermal cycles. Weight-change measurements of heater heads before and after service in a WhisperGen™ could be useful in determining the extent of spalling and oxide rehealing that occurs. Mechanical testing would be useful in assessing the extent of embrittlement and loss of strength caused by the internal oxidation, decarburisation and precipitate phase development observed in the 310 and 253MA heater heads. Finally, a continuous weight-measurement method would be useful when assessing spalling performance, and would take away the doubt behind whether rehealing of the oxide layer occurs.

Appendix A: End cap drawings

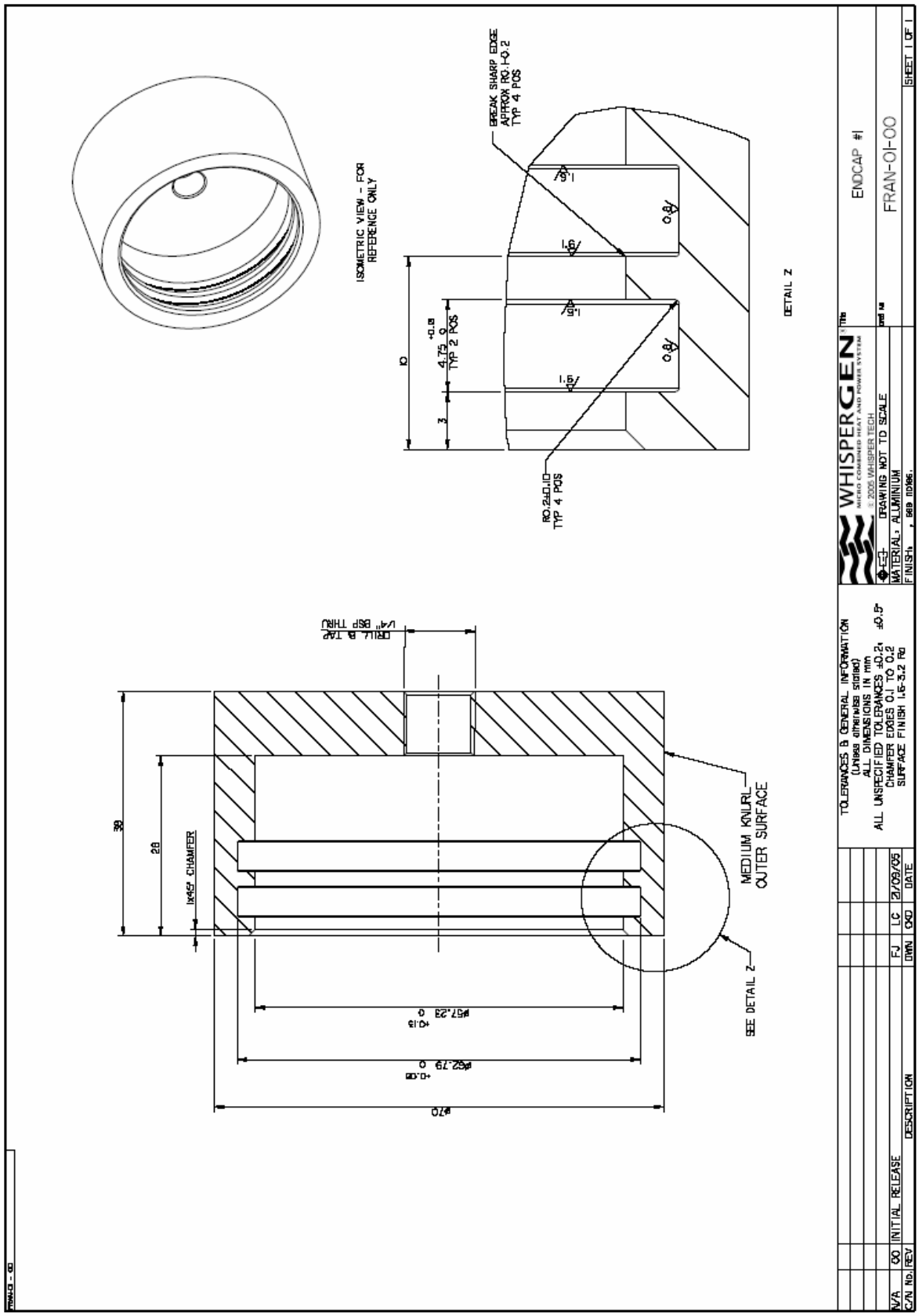

Figure A1: CAD drawing of outlet end cap for experimental set up

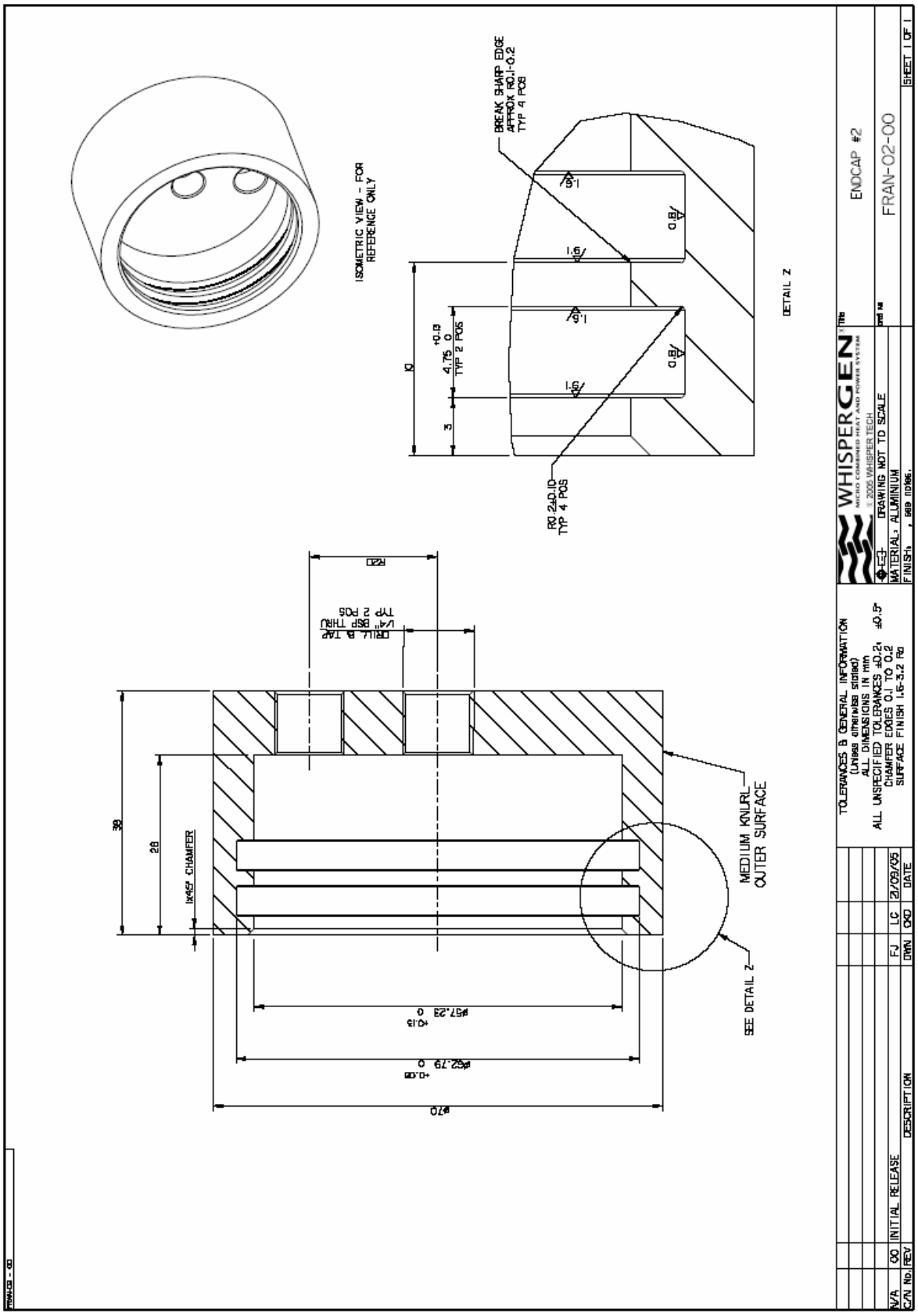

Figure A2: CAD drawing of inlet end cap for experimental set up

Appendix B: Check for laminar flow through tube

Calculation to check laminar flow (for nitrogen)

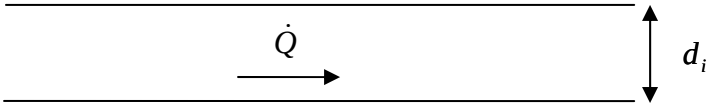

Volume flow rate $\dot{Q} = 0.05LPM = 8.3\times10^{-7}\,m^3s^{-1}$
Inner diameter $d_i = 53mm = 0.053m$

1). Calculation to find velocity of nitrogen through tube:

$\dot{Q} = A\tilde{v}$ where A is inside area of tube cross section, and $\tilde{v}$ is the velocity of fluid through the tube.

$$A = \frac{\pi d_i^{\,2}}{4} = \frac{\pi(0.053)^2}{4} = 0.0022m^2$$

$$\tilde{v} = \frac{\dot{Q}}{A} = \frac{8.3\times10^{-7}}{2.206\times10^{-3}} = 3.76\times10^{-4}\,ms^{-1}$$

2). Calculation to find density ρ at 900°C

$pV = nRT$ for an ideal gas.

$$\text{Density, } \rho = \frac{m}{V} = \frac{PM}{RT} = \frac{(1.101\times10^3)(28)}{(8.314)(1173)} = 3.16kgm^{-3}$$

Where the pressure (P) is 1 atm, the molar mass of nitrogen (M) is 28 $gmol^{-1}$, the gas constant (R) is 8.314 $JK^{-1}mol^{-1}$ and the temperature is 1173 K.

Kinematic viscosity, υ, of nitrogen at 1 atm

3). Calculation to find Reynold's number, Re

$$\text{Re} = \frac{ud_i}{\nu}$$

Kinematic viscosity υ of nitrogen at 1 atm and 1173 K is approximately $1\times10^{-5}\,m^2s^{-1}$

Hence $\text{Re} = \frac{ud_i}{\upsilon} = \frac{(3.76\times10^{-4})(0.053)}{1\times10^{-5}} = 2$

The laminar to turbulent transition occurs at approximately Re > 2100.

$\Rightarrow$ **Flow through tube is laminar.**

Appendix C: Safety assessment for laboratory testing

Number	Hazard	Significant effects	Consequence	Probability	Risk (Consequence x Probability)	Control
1	Gas cylinder falling over	Crushing someone, potential missile	4	4	16	Secure gas cylinder to wall
2	Furnace electrical connection	Risk of electric shock	4	2	8	Confirm electrical conformance
3	Glass tube breaking due to excessive heat	Gas leak; broken glass	3	2	6	Confirm furnace set point temperature and check regularly
4	Glass tube breaking due to mechanical damage	Gas leak; broken glass	3	2	6	Ensure adequate warnings are in place
5	Furnace moving due to earthquake	Gas leak; broken glass; fire risk	4	2	8	Chock furnace wheels
6	Gas leak due to faulty regulator	Minor asphyxiation risk; minor explosion hazard	4	2	8	Confirm operation of regulator suits application. 2 CO monitors in place to register dangerous concentrations
7	Gas leak due to faulty hose/tube/tube connections. Mixing with atmospheric air to form a combustible mixture.	Gas composition 60% CO and 40% CO_2. Minor asphyxiation risk, minor explosion hazard.	4	3	6	Check tube connections etc on commissioning and regular intervals during testing. 2 CO monitors in place to register dangerous concentrations, jubilee clips on connections. Extraction fan running at all times.

8	Gas leak from experimental apparatus mixing with air to form asphyxiation mixture.	Minor asphyxiation risk.	4	3	12	Route outlet tube to outside building, 2 CO monitors in place to register dangerous concentrations, door to room closed at all times with notice on door to call 111 if CO alarm is heard. Extraction fan running at all times.
9	Burn on hot apparatus.	Burns.	4	3	12	Adequate signage and IPE.
10	Overpressurisation of apparatus.	Explosion hazard, flying debris, cuts.	4	4	16	End caps will pop off.

Classification of numbers:

4 = High
3 = Med
2 = Low
1 = Very low

Appendix D: Example from the Atlas of Microstructures (253MA Heater Head)

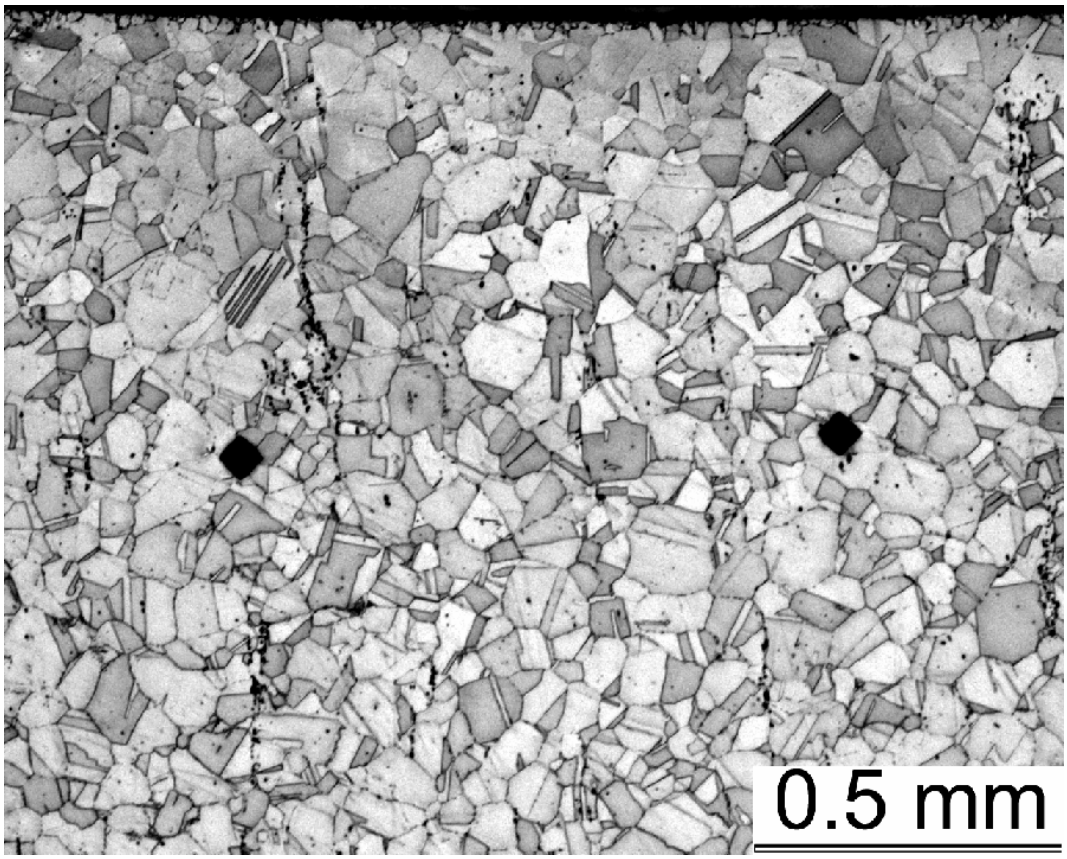

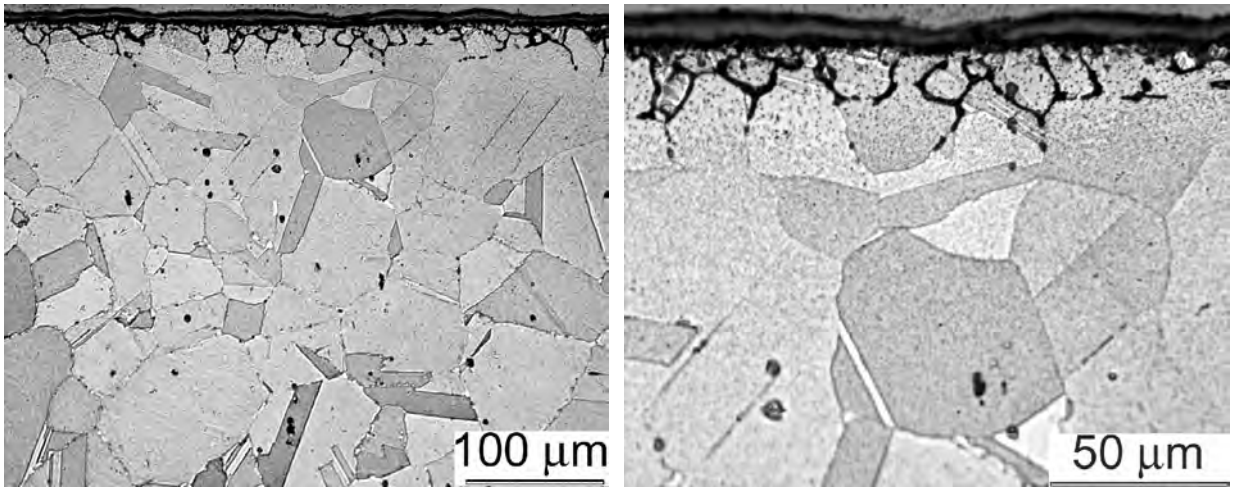

Figure D1: Optical microscopy images of the 253MA heater head at several magnifications, etched in glyceregia.

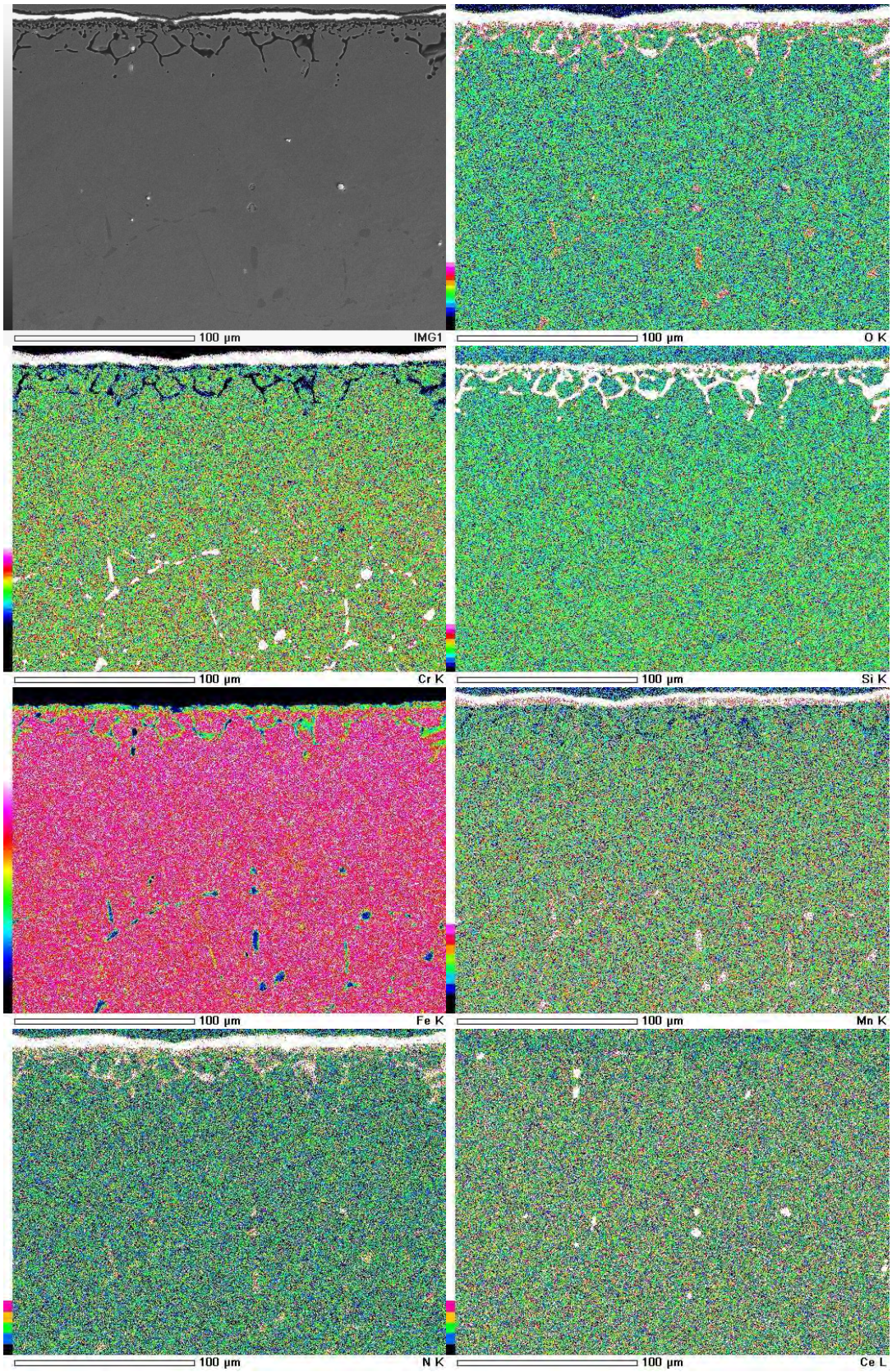

Figure D2: X-ray maps of the 253MA heater head, showing relevant elements at a lower magnification.

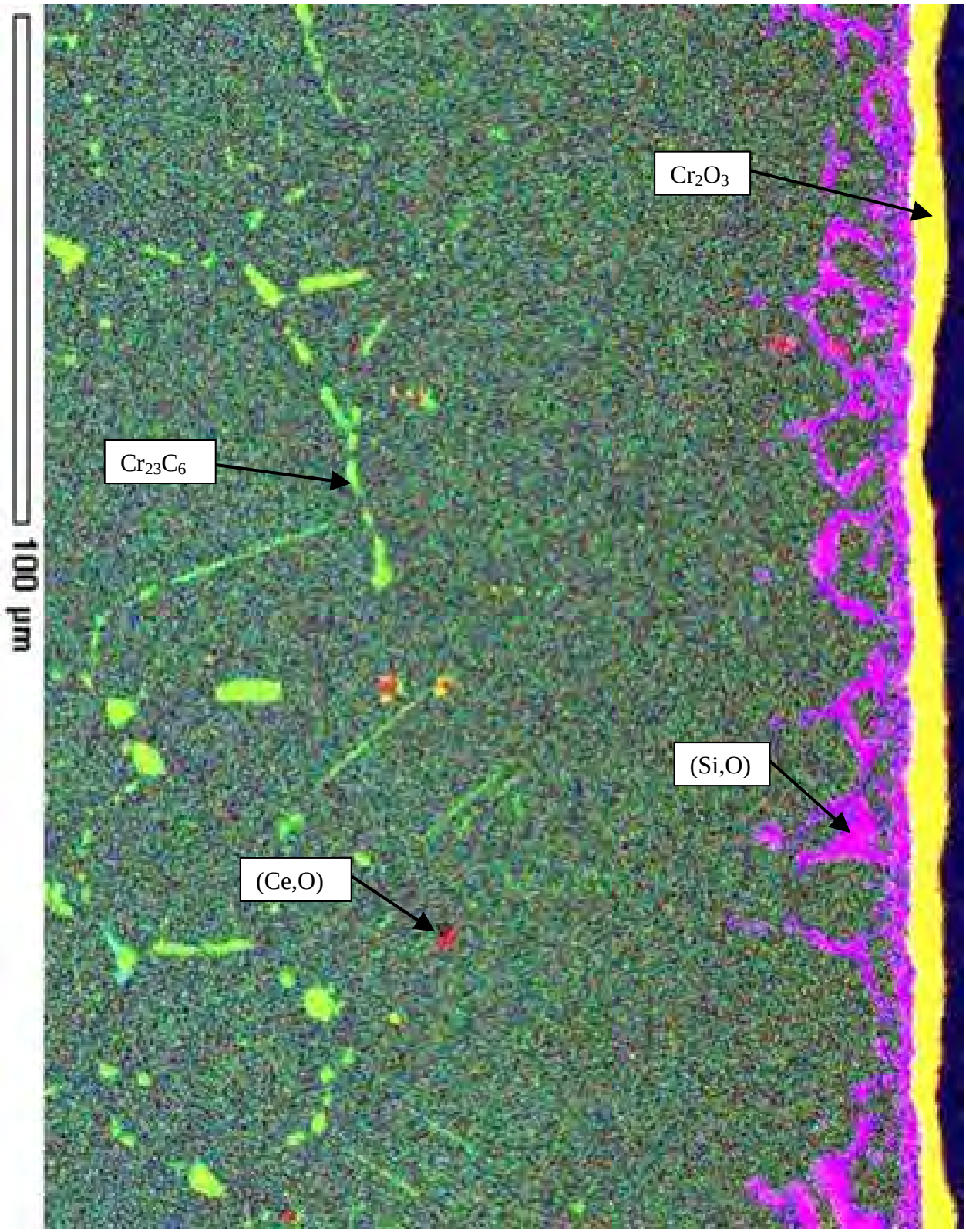

Figure D3: Composite X-ray map of the 253MA heater head, showing an overlap of the elements O, Cr and Si at a lower magnification.

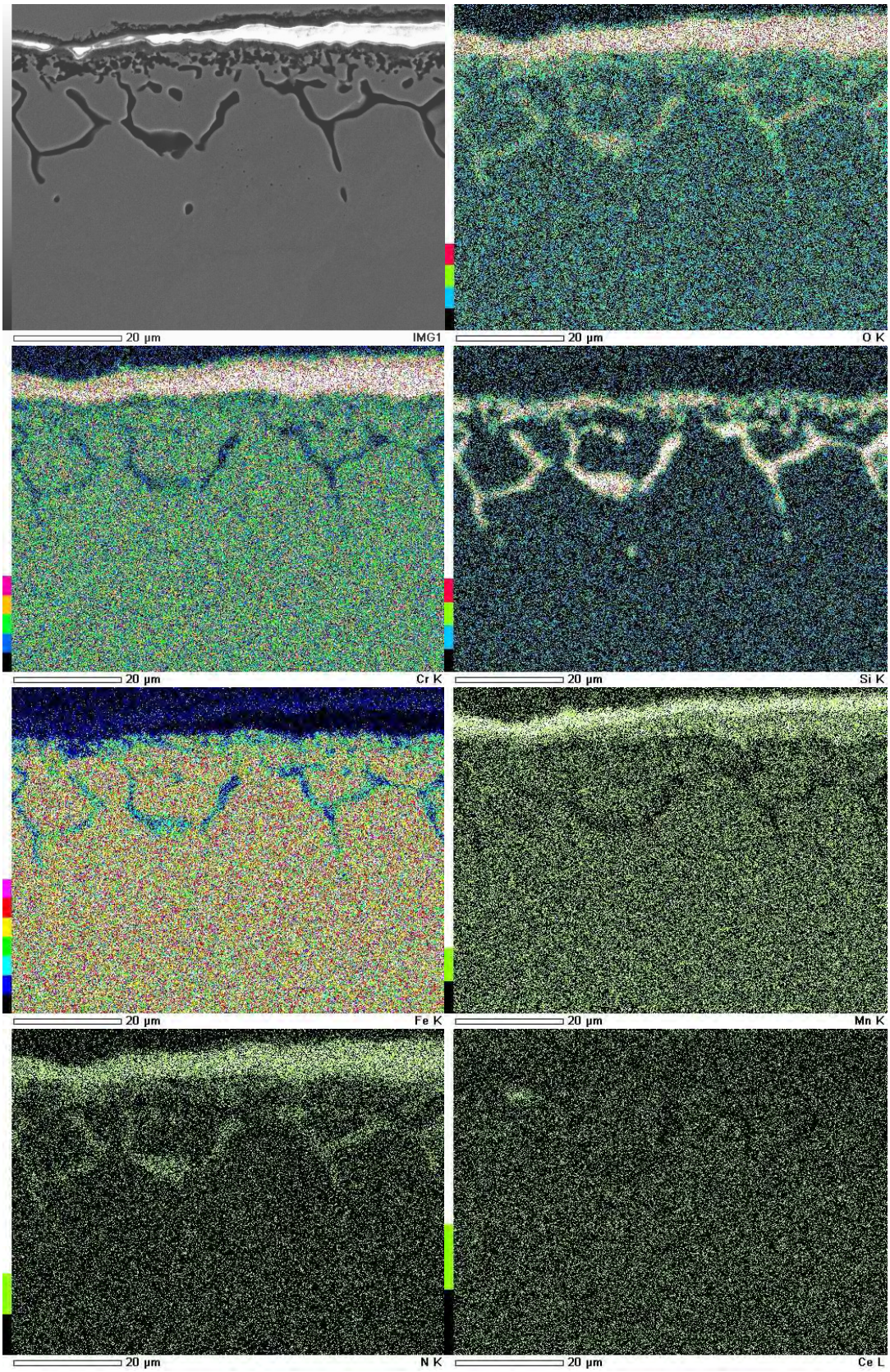

Figure D4: X-ray maps of the 253MA heater head, showing relevant elements at a higher magnification

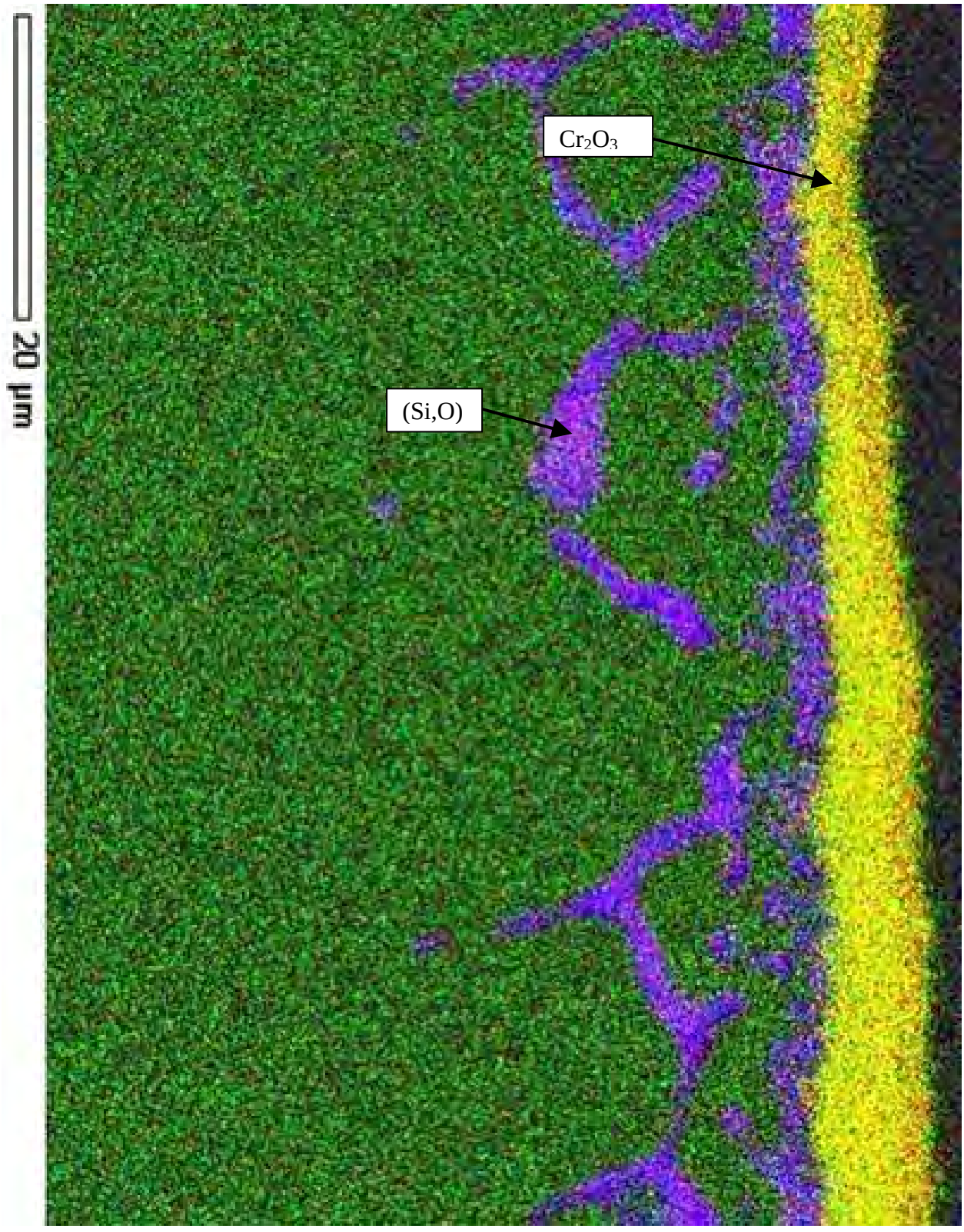

Figure D5: Composite X-ray map of the 253MA heater head, showing an overlap of the elements O, Cr and Si at a higher magnification

Appendix E: Summary of microstructures for test results

TableE1: Summary of microstructure development for heater head testing

Sample	**Phases Present**	
	Scale	**In alloy**
253MA Heater Head	Cr_2O_3	(Si,O) on austenite grains beneath scale to a depth of ~35μm
		$Cr_{23}C_6$ on grain boundaries throughout, starting ~100μm beneath scale
		(Ce,O) and/or (Ce,S) inclusions form stringers
310 Heater Head	Cr_2O_3	(Si,O) on austenite grains beneath scale to a depth of ~7μm
		Sigma phase formation on grain boundaries throughout, starting ~30μm beneath scale
800H Heater Head	Cr_2O_3	Al_2O_3 on austenite grains beneath scale to a depth of ~10μm
		(Nb,Ti)C, N or S precipitates sporadic
		(Si,O) layer beneath scale <1μm
		TiC or TiN stringers throughout

TableE2: Summary of microstructural development for laboratory tests undertaken in CO/CO_2 gas mixtures at 900°C

Sample	**Phases Present**	
	Scale	**In alloy**
900°C (CO/CO_2)		
253MA (300 hours)	Cr_2O_3	Fine (~1μm) $Cr_{23}C_6$ on grain boundaries throughout, starting ~20μm beneath scale
		Sporadic (Si,O) layer beneath scale, ~1.5μm thick
		Ce_2O_3 and (Ce,S) inclusions form stringers
253MA (600 hours)	Cr_2O_3	Fine $Cr_{23}C_6$ on grain boundaries throughout, starting ~20μm beneath scale
		(Si,O) layer beneath scale, 2-4μm thick
		(Ce,O) and (Ce,S) inclusions form stringers
310 (300 hours)	Cr_2O_3	Extensive grain boundary precipitation of sigma phase throughout, starting ~30μm beneath scale
		(Si,O) on austenite grains beneath scale to a depth of ~8μm
		$Cr_{23}C_6$ on grain boundaries throughout
		Mn-rich inclusions sporadic
310 (600 hours)	Fe_3O_4 Spinel	Extensive grain boundary precipitation of sigma phase throughout, starting ~30μm beneath scale
	(Cr-rich)	(Si,O) on austenite grains beneath scale to a depth of ~10μm
		$Cr_{23}C_6$ on grain boundaries throughout
		(Ti,O) inclusion with a Fe_3O_4 structure
800H (300 hours)	Cr_2O_3	(Al,O) on austenite grains beneath scale to a depth of ~18μm
	Mn-rich	(Si,O) layer beneath scale ~2μm
	outer	TiC or TiN precipitates form stringers throughout
800H (600 hours)	Cr_2O_3	Al_2O_3 on austenite grains beneath scale to a depth of ~25μm
	Mn-rich	(Si,O) layer beneath scale ~2μm
	outer	TiC and/or TiN precipitates
		Ti-rich precipitates in and near scale
		TiC or TiN precipitates form stringers throughout

TableE3: Summary of microstructural development for laboratory tests undertaken in CO/CO_2 gas mixtures at 800°C

Sample	Phases Present	
	Scale	**In alloy**
800°C (CO/CO_2)		
253MA (300 hours)	Cr_2O_3	Fine $Cr_{23}C_6$ on grain boundaries throughout, starting ~15μm beneath scale
		(Cr,Si)-rich precipitates beneath scale, unable to identify EBSD pattern
253MA (600 hours)	Cr_2O_3	Fine $Cr_{23}C_6$ on grain boundaries throughout, starting ~20μm beneath scale
		Tiny Si-rich precipitates (too small to obtain EBSD pattern)
		(Ce,O) and/or (Ce,S) inclusions present but not in stringers
310 (300 hours)	Cr_2O_3	Extensive sigma phase formation starting ~15μm beneath scale and continue for ~15μm then stop, beneath which sigma is on grain boundaries throughout
		(Si,O) layer beneath scale, ~2.5μm
		(Mn,O) inclusion
310 (600 hours)	Cr_2O_3	Extensive sigma phase formation starting ~ 10μm beneath scale and continue for ~25μm then stop, ~20μm beneath which grain boundary sigma precipitates are throughout
		(Si,O) layer beneath scale, ~3μm
800H (300 hours)	Cr_2O_3	(Al,O) on austenite grains beneath scale to a depth of ~6μm
	Mn-rich	(Si,O) layer beneath scale <1μm thick
	outer	TiC and/or TiN precipitates
		Small TiN and/or TiC precipitates form stringers throughout
800H (600 hours)	Cr_2O_3	(Al,O) on austenite grains beneath scale to a depth of ~10μm
	Mn-rich	(Si,O) layer beneath scale <1μm thick
	outer	TiC and/or TiN precipitates
		Small TiN and/or TiC precipitates form stringers throughout
		Ti-rich precipitates beneath scale (no EBSD pattern)
		Fine $Cr_{23}C_6$ on grain boundaries throughout, starting ~20μm beneath scale

TableE4: Summary of microstructural development for laboratory tests undertaken in CO/CO_2 gas mixtures at 700°C

Sample	**Phases Present**	
	Scale	**In alloy**
700°C (CO/CO_2)		
253MA (300 hours)	(Cr,O)	(Ce,O) and/or (Ce,S) inclusions form stringers throughout
253MA (600 hours)	Cr_2O_3	Fine $Cr_{23}C_6$ on grain boundaries throughout, starting ~5μm beneath scale
		(Ce,O) and/or (Ce,S) inclusions form stringers throughout
310 (300 hours)	Cr_2O_3	Region of sigma phase starts ~3.5μm beneath scale, and is ~15μm thick
		Fine Cr-rich precipitates on grain boundaries throughout (too fine to get pattern with EBSD)
		(Al,O) inclusion (sporadic)
310 (600 hours)	Cr_2O_3	Region of sigma phase starts ~6μm beneath scale, and is 9-16μm thick
		Fine Cr-rich precipitates on grain boundaries throughout (too fine to get pattern with EBSD)
		(Al,O) inclusion (sporadic)
800H (300 hours)	Cr_2O_3	(Al,O) on austenite grains beneath scale to a depth of ~2μm
		(Si,O) layer beneath scale <1μm thick
		TiC and/or TiN precipitates
		Small TiN and/or TiC precipitates form stringers throughout
		Fine Cr-rich precipitates on grain boundaries throughout, (too fine to get an EBSD pattern)
800H (600 hours)	(Cr,O)	(Al,O) on austenite grains beneath scale to a depth of ~2μm
		TiC and/or TiN precipitates
		Small TiN and/or TiC precipitates form stringers throughout
		Fine $Cr_{23}C_6$ precipitates on grain boundaries throughout

TableE5: Summary of microstructural development for laboratory tests undertaken in nitrogen at 900°C

Sample	**Phases Present**	
	Scale	**In alloy**
900°C (Nitrogen)		
253MA (300 hours)		Very non-uniform corrosion
Case 1	Cr_2O_3 and Cr_2N	Dense Cr_2N precipitates start ~4μm beneath scale to a depth of ~130μm, then become less dense with distance
		$Cr_{23}C_6$ (~3μm) precipitates on grain boundaries throughout
		Non-continuous (Si,O) layer beneath scale ~1μm thick
		(Ce,O) inclusions sporadic
Case 2	(Cr,O)	Region of Cr_2N precipitates starts ~20μm beneath scale to a depth of ~60μm
		Fine Cr-rich precipitates on grain boundaries throughout (difficult to differentiate between $Cr_{23}C_6$ and CrN pattern with EBSD)
		Non-continuous (Si,O) layer beneath scale ~1μm thick
		(Ce,O) inclusions sporadic
253MA (600 hours)	Cr_2O_3	$Cr_{23}C_6$ (~3μm) precipitates on grain boundaries throughout
		(Ce,O) and/or (Ce,S) inclusions form stringers throughout
310 (300 hours)	Cr_2O_3	Sigma phase on grain boundaries throughout, starting ~20μm beneath scale
		(Si,O) on austenite grains beneath scale to a depth of ~10μm
310 (600 hours)	Fe_3O_4 and Cr_2O_3	Sigma phase on grain boundaries throughout, starting ~40μm beneath scale
		(Si,O) on austenite grains beneath scale to a depth of ~15μm
800H (300 hours)	Cr_2O_3	(Al,O) on austenite grains beneath scale to a depth of ~35μm
	Mn-rich	(Si,O) layer beneath scale ~3μm thick
	outer	Ti-rich layer beneath scale ~5μm thick (no EBSD pattern)
		TiN and/or TiC precipitates form stringers throughout
800H (600 hours)	Cr_2O_3	Al_2O_3 on austenite grains beneath scale to a depth of ~30μm
	Mn-rich outer	Needle-like AlN starts ~45μm beneath scale and continues to a depth of up to ~330μm beneath scale
		TiC and/TiC precipitates sporadic
		TiN and/or TiC precipitates form stringers throughout

TableE6: Summary of microstructural development for laboratory tests undertaken in nitrogen at 800°C

Sample	**Phases Present**	
	Scale	**In alloy**
800°C (Nitrogen)		
253MA (300 hours)	(Cr,O)	Precipitates beneath scale from depths of ~5-20μm – unable to identify pattern using EBSD but EDS shows Cr,Si,Mn,Fe and Ni
		$Cr_{23}C_6$ on grain boundaries throughout, starting beneath unknown precipitates
		(Ce,O) inclusions sporadic
253MA (600 hours)	(Cr,O)	Precipitates beneath scale – unable to identify pattern using EBSD but EDS shows Cr,Si,Mn,Fe and Ni
		$Cr_{23}C_6$ on grain boundaries throughout, starting beneath unknown precipitates
		(Ce,O) inclusions sporadic
		Tiny Si-rich precipitates formed in lines (too small to identify)
310 (300 hours)	Fe_3O_4 Spinel	Sigma phase throughout, starting ~10μm beneath scale, with greater density near the scale
		(Si,O) layer beneath scale ~1μm thick
310 (600 hours)	(Cr,O)	Sigma phase throughout, starting ~10μm beneath scale, with greater density near the scale
		Non-continuous (Si,O) layer beneath scale ~1μm thick
800H (300 hours)	(Cr,O)	(Al,O) on austenite grains beneath scale to a depth of ~10μm
		(Si,O) layer beneath scale <1μm thick
		Sporadic TiC and/or TiN precipitates
		Small TiN and/or TiC precipitates form stringers throughout
		Ti-rich precipitates around beneath scale (no EBSD pattern)
		CrN precipitates beneath scale
800H (600 hours)	Cr_2O_3	(Al,O) on austenite grains beneath scale to a depth of ~10μm
		(Si,O) layer beneath scale <1μm thick
		Sporadic TiC and/or TiN precipitates
		Small TiN and/or TiC precipitates form stringers throughout
		(Si,O) inclusion (no EBSD pattern)

Table E7: Summary of microstructural development for laboratory tests undertaken in nitrogen at 700°C

Sample	Phases Present	
	Scale	**In alloy**
700°C (Nitrogen)		
253MA (300 hours)	No scale	(Ce,O) and/or (Ce,S) inclusions form stringers
253MA (600 hours)	No scale	(Ce,O) and/or (Ce,S) inclusions form stringers
310 (300 hours)	(Mn,O)	Scale is Mn-rich (but not Cr-rich)
		Region of sigma phase starts ~2μm beneath scale, and is ~8μm thick
		$Cr_{23}C_6$ precipitation on grain boundaries throughout
310 (600 hours)	(Mn,O)	Scale is Mn-rich (but not Cr-rich)
		Region of sigma phase starts ~2μm beneath scale, and is ~18μm thick
		$Cr_{23}C_6$ precipitation on grain boundaries throughout
800H (300 hours)	Cr_2O_3	(Al,O) on austenite grains beneath scale to a depth of ~1μm
	and CrN	Small TiN and/or TiC precipitates form stringers throughout
800H (600 hours)	(Cr,O)	(Al,O) on austenite grains beneath scale to a depth of ~1μm
		(Si,O) layer beneath scale <1μm thick
		Sporadic TiC and/or TiN precipitates
		Small TiN and/or TiC precipitates form stringers throughout
		Fine Cr-rich precipitates on grain boundaries throughout, (too fine to get an EBSD pattern)